University of Alberta

Microstructure and Properties of Ni-Alloy and Ni-WC Composite Overlays

by

Thilan Liyanage

A thesis submitted to the Faculty of Graduate Studies and Research
in partial fulfillment of the requirements for the degree of

Master of Science

in

Materials Engineering

Chemical and Materials Engineering

©Thilan Liyanage
Fall 2010
Edmonton, Alberta

I would like to dedicate this work to my parents who have supported me through good and difficult times. Without their love and patience I would not have been able to take advantage of the opportunity I was given to further my education.

Acknowledgements

Abstract

The microstructures and performance of Ni-based alloys and Ni-WC (nickel-tungsten carbide) composite overlays deposited by plasma transferred arc welding have been studied. The Ni-alloy overlays had similar microstructures consisting of γ-Ni dendrites, with interdendritic Ni-based eutectics, borides and carbides. Low hardness alloy overlays contained a smaller fraction of interdendritic phases relative to the high hardness alloys. The interdendritic regions make a significant contribution to the hardness since they are more than twice as hard as primary dendrites.

The Ni-WC composites contained similar phases, however WC dissolution was observed leading to the formation of other carbides. Ni-alloys with low carbon and Cr content exhibited the lowest WC dissolution. The Ni-WC overlays produced using these dilute alloys generally performed better in ASTM G65 wear tests. This was likely due to the reduced dissolution which avoided formation of brittle secondary phases, maintaining a short mean free path between WC particles and allowing increased impact energy absorption.

Table of Contents

List of Tables

List of Figures

List of Acronyms

AES…………Auger Electron Spectroscopy

ASTM………American Society for Testing and Materials

DTA………...Differential Thermal Analysis

EDS/EDX…...Energy Dispersive X-ray Spectroscopy

EPMA………Electron Probe Microanalysis

GTAW...........Gas Tungsten Arc Welding

HVOF……….High Velocity Oxy Fuel

ICP………….Inductively Coupled Plasma

LC…………...Laser Clad

MMC……..….Metal Matrix Composite

PTA…………Plasma Transferred Arc

PTAW………Plasma Transferred Arc Welding

SEM………....Scanning Electron Microscope

TEM………....Transmission Electron Microscope

WC…………Tungsten Carbide

WDS…………Wavelength Dispersive Spectroscopy

XRD………....X-ray Diffraction

1. Overview of Plasma Transferred Arc Welding Overlay Deposition

Overlay welding is used to improve the wear resistance of surfaces on industrial parts by depositing a protective layer of abrasion and/or corrosion resistant weld metal onto a base material surface. This technique is especially useful in high wear environments such as those experienced in a wide range of mining industries, in particular those encountered in the oil sands of Alberta [1]. The extreme wear decreases productivity and the useful life of equipment, as such overlay welding is used to apply a thick coating onto components in order to reduce the overall maintenance costs [1-3]. Plasma Transferred Arc Welding (PTAW) is a high energy-intensity process which can be made portable [4] and can be used to deposit a thick (>3mm) layer of a wear resistant alloy. It offers the following advantages with respect to other deposition methods: (1) low dilution (usually <10%) in the deposit, (2) excellent metallurgical bonding with the substrate, and (3) dense, defect-free deposits [2-3, 5-7]. Overlays may however have inherent defects throughout the layer resulting from extrinsic (shrinkage and gas porosity) and intrinsic (brittle phase precipitation) microstructural defects [8].

PTAW is used to deposit Ni-WC overlays especially when wear rates are high and the performance required exceeds that of Cr-carbide based ferrous overlays. Plasma transferred arc welding (PTAW) is similar to gas-tungsten arc welding (GTAW) where an electric arc is established between a tungsten electrode and the base material (see Figure 1.1). Inert argon gas is generally used for the arc plasma supply, for powder transport, and for shielding of the weld pool [9]. Factors that have a strong effect on the weld deposit are the weld speed, carrier gas/powder speed, and arc current, while other variables such as powder and gas composition are typically kept constant.
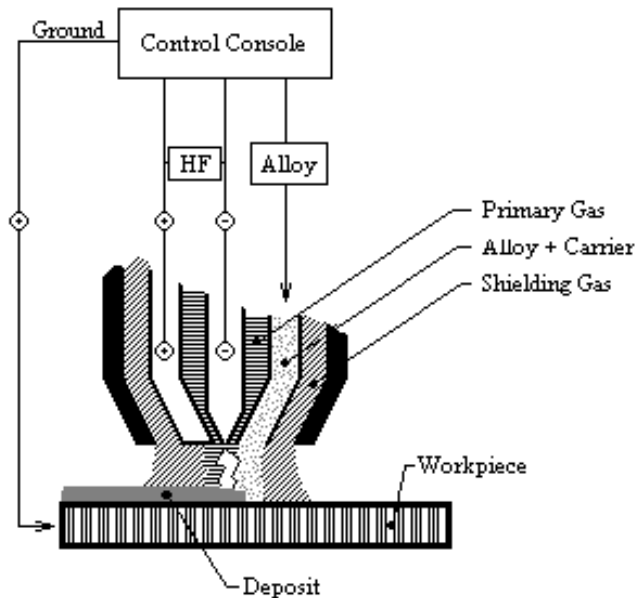
Figure 1.1. Schematic of plasma transferred arc welding torch (using high frequency (HF) pilot arc). [10]

There are two key issues relevant to the deposition of Ni-WC based metal matrix composite (MMC) overlays using PTAW: dilution of the substrate material and dissolution of the reinforcing WC particles. Dilution is defined as the percentage of the melted substrate relative to the total melted area (which includes the substrate and the deposit, shown in Figure 1.2). As shown by D'Oliveira et al.[9], the dilution level is directly dependent on the heat input (arc current and travel speed) into the weld area as melting and diffusion are a function of temperature. Dilution is detrimental to a hard coating as it may lower the integrity of the substrate as well as promote undesired reactions between the substrate and the deposit.

$$\delta = \frac{Substrate\ melted\ area}{Total\ melted\ area} \times 100 = \frac{B}{A + B}$$
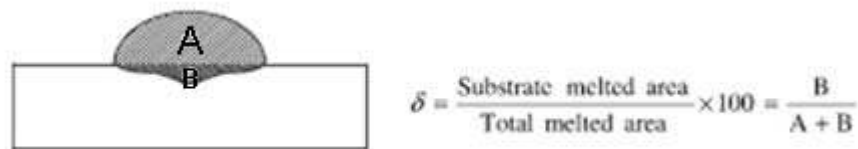
Figure 1.2. Dilution Measurement. [9]

The other issue, dissolution of the WC particles, results in lowered wear resistance as there is less reinforcing material remaining to offer protection from

abrasive wear. Particle dissolution occurs when excessive arc current provides sufficient heat to cause WC material to go into solution above a critical temperature (Figure 1.3 shows the loss of the large carbides due to dissolution).
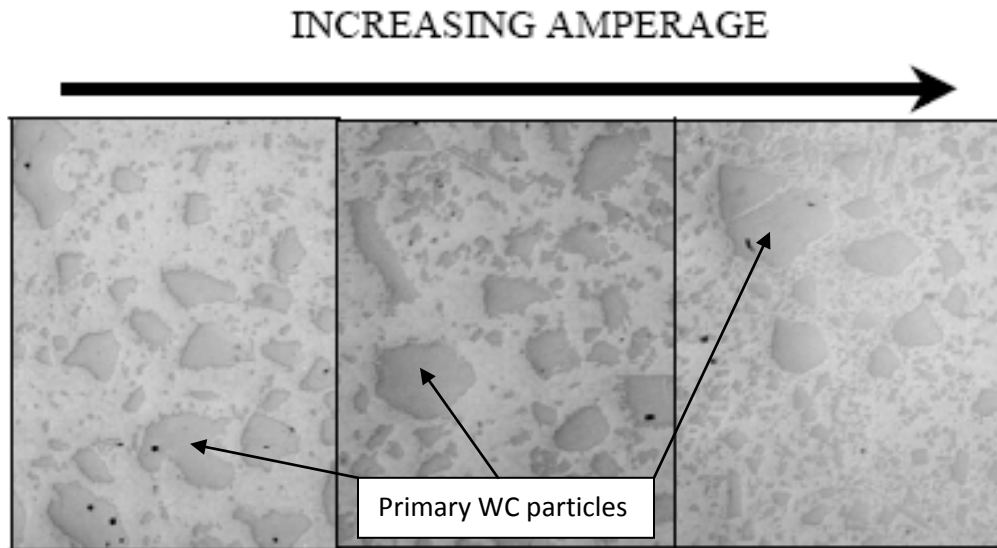
Figure 1.3. Effect of increasing current on WC particle dissolution during PTAW deposition. [10]

There are some other challenges associated with the PTAW overlay process as well. For example, the heat input from multipass welds can also have an effect on the microstructure as found by Cockeram where a higher density of precipitates in the first deposited weld layers resulted from heat input from the top weld layers in several Ni-based alloys [11]. In addition, differences in coefficients of thermal expansion between the base metal and the hardfacing can produce large thermal stresses under thermal shock conditions resulting in cracking of the hardfacing [11].

Since the ductility of γ-Ni is fairly high, this should reduce the tendency of microcrack formation, although they may still occur in the overlay. The microcracks could be avoided even without preheating specimens by continuous welding which will increase the temperature of the substrate and so decrease cracking due to differences in thermal expansion. Porosity may also occur during

PTAW as the plasma and shielding gases impact the surface with a high velocity and enter the molten pool, however the gas can escape from the molten pool if the solidification rate is low enough, which can be achieved with a higher current [12].

1.1.   Ni-Alloy Powder Characteristics

Nickel-based self-fluxing alloys (NiCrBSi and NiBSi) are attractive for use in the mining industries due to their excellent wear and corrosion resistance and relatively low cost. The alloys are typically divided into two groups: chromium-containing and chromium-free. The chromium containing powders are typically characterized as low Cr (~8wt%Cr), medium Cr (~11wt% Cr), and high Cr (~20wt% Cr). For a relatively hard (high-Cr) NiCrBSi alloy a typical composition   is   Ni-13wt%Cr-2wt%B-4wt%Si-5wt%Fe-0.5wt%C   (all compositions in this thesis will be indicated in wt% unless otherwise noted). The addition of boron and silicon to these alloys improves their wetting to the steel substrate during welding and provides them with "self-fluxing" characteristics (ie. self-deoxidization and self-slag formation when melted) [13-15].

The melting point of the NiCrBSi alloys is reduced by the addition of boron in concentrations up to 2.5 wt% and welding is also favourable due to the wide solidification temperature range which characterizes the alloys containing Ni and B [3, 15-17]. Silicon increases the self-fluxing properties, the castability, and the wetting characteristics but does not have an important influence on the melting point or solidification behavior [16]. Both B and Si act as deoxidizers to form low melting point borosilicate which prevents further oxidation of active elements in the alloys [14, 18]. The oxides ascend toward the surface through the molten deposit and are removed as slag [16]. Simultaneously the eutectic Ni-Ni_3B forms together with the highly wettable borosilicate, allowing deposition to occur at lower temperatures [14]. In fact, wetting of borosilicate in nickel alloys is so good that a liquid phase sintering at around 1030°C homogenizes the

chemical composition (along with enhancing the precipitation of chromium carbides and borides) [14]. The thermal input to the substrate can thus be decreased using these alloy additions, however, the NiCrBSi powders were originally designed for welding methods such as high velocity oxy fuel (HVOF) welding that do not reach temperatures as high as plasma torches (>10,000°K [12]). Consequently, these alloying additions may not be fully optimized for PTAW of overlays, since there may not necessarily be a need for such strong melting point suppressants [13-14].

The boron and carbon present in the NiCrBSi alloys react with the chromium to produce the hard borides and carbides and hence raise the cavitation and wear resistance of the coatings [14, 19]. The hard phases formed in Cr-free alloys are borides (eg. Ni_3B) and silicides (eg. Ni_3Si). Further addition of hard reinforcing compounds such as WC, TiC and $B_{13}C_2$, can also significantly improve the tribological properties. [19]

The type of powder used as the feedstock gives the desired properties for the particular application and careful control of feedstock powder chemistry and particle size distribution is required during PTAW. Generally, particles with a spherical shape (Figure 1.4), narrow size distribution, and chemical homogeneity are preferred.
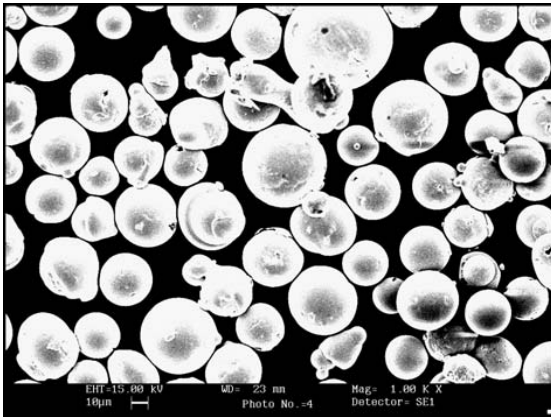
Figure 1.4. SEM micrograph of NiCrBSi powder. [20]

Tungsten carbide (WC) is widely used in high-wear environments as a reinforcing phase in metal matrix composites since it combines desirable properties such as high hardness (>2000HV), high melting point (>3000K) and a

low coefficient of thermal expansion (3.88-5.96 x 10^{-6} K^{-1} for the range 273-2000 K [21]) Tungsten carbide is also favourable due to a certain amount of plasticity and good wettability by molten metals. The main disadvantage of WC is its low heat of formation at about -40 kJ/mol, which makes it easily dissolved by molten metals [21]. In general, the more negative the heat of formation the more stable the carbide, although there are some exceptions to this rule.

In general the two methods of preparing tungsten carbide are carburization of elemental tungsten powder and eutectic melting of tungsten and carbon to form melt carbide. The melt carbide has a higher hardness as well as higher density and so is preferred for manufacturing cemented carbide and for use in high-wear scenarios. In the W-C system, tungsten carbide exists in three intermediate phases (with 3 eutectic reactions), namely W_2C, WC_{1-x}, and WC. WC is formed peritectically at 2776°C and 6.13wt% C (50at%) [21]. When producing fused tungsten carbide ($WC+W_2C$), a eutectic melt of about 4.5wt% C is rapidly cooled. In the above mentioned reaction, graphite would precipitate at carbon contents above 4.5 wt% C which reduces hardness and wear resistance and so is undesirable [21]. Carbon contents below 3.8wt% yield high quantities of W_2C which is not suitable for wear applications since it is extremely brittle, more prone to dissolution, and tribologically less resistant than WC [21].

1.2.   *Wear Characterization*

During abrasive wear, the surface of a soft material is gouged out by the abrasive particles/phases of the harder material and produces wear chips when the abraded material is elastoplastic or viscoelastic-plastic. It has been found that the wear rate increases rapidly up to an abrading particle size of about 1µm then increases slowly or levels off [22]. Below 1µm, wear is not caused by abrasive wear but approaches delamination wear. Abrasive wear involves subsurface

plastic deformation (increases as wear particles themselves develop flat surfaces) in addition to cutting of the surface and generation of wear chips [22].

During abrasive wear of MMCs, material is removed by three major mechanisms: (1) micro-cutting (gouging), (2) plastic deformation, and (3) fracture or pull-out of the reinforcing particles in the matrix material. Micro-cutting is usually considered to have the most important contribution to abrasive wear [23]. The first two factors can be addressed by a suitably hard matrix, and the third factor can be addressed by reinforcing particles that have good mechanical properties (a combination of hardness and toughness), do not dissolve easily, and which are not overly brittle.

There are two major wear modes in abrasive wear: 2-body and 3-body wear. Two-body wear occurs when two materials slide against each other and material is removed from one or both surfaces. The wear volume for two-body wear is almost linearly proportional to the sliding distance and the normal loads, but inversely proportional to the hardness of the material. Three body abrasive wear occurs when abrasive particles in the form of wear debris or particles of grit and dust from the surroundings remain trapped on the sliding surfaces and remove material largely by microcutting.

For some composite systems it was reported that a shift in fracture mode toward decohesion at the particle/matrix interfaces occurred when higher heat input allowed extensive precipitation of alloying elements along the matrix/particle interfaces. Conversely low heat input lead to particle cracking due to increased stress concentration at the reinforcement phases during straining of the composite. [24]

In a broad sense, the wear resistance of a material depends on many parameters of the tribological system (such as size, shape, roughness and hardness of the abrading surface/particles, loading conditions, sliding speed, and environment) [25-26]. In the case of NiCrBSi and MMC coatings, the wear resistance depends on the above mentioned factors as well as on their ability to withstand gouging of the matrix and particle pull-out. These two factors in turn

depend on the hardness and fracture toughness of the coating and the strength with which the reinforcing particles are bound to the matrix.

The fracture toughness (K_{IC}) of nickel-base hardfacing alloys is accurately described by a crack-bridging model. Crack bridging in Ni-based alloys is described as "the toughening of the brittle matrix of carbide, boride, and silicide interdendrite phases by the stretching, necking, and plastic elongation of the nickel-phase dendrites in the wake of a crack tip that is propagating through the continuous brittle matrix" [7]. For example, after compact tension specimen fracture toughness testing of several Ni-based alloys, plastic stretching and necking was observed for 55 to 80 pct of dendrites in the failure region, giving credence to the assertion that plastic deformation of the matrix plays a large role in the fracture toughness of the coatings [7].

Incorporating fine, well dispersed particles into a matrix can also increase fracture toughness and it was found that increasing the WC content from 0 to 35wt% during flame-spray of NiCrBSi + WC powders increased the coating hardness and there was a toughening of the coating with little increase in brittleness [27]. However, increasing WC content further decreased hardness and toughness as there was a sharp increase in porosity and pore size [27].

The properties of the abrading particles have been found to have an effect on the wear resistance of NiCrBSi-WC alloys. Pin-on-disc abrasive wear testing (2-body abrasion) of the matrix alloy (without WC) was stated to have higher wear resistance compared to the matrix with WC (>2000HV) when abraded with SiC (3000HV) [27]. However, the wear resistance of the matrix was lower when abraded with Al_2O_3 (2000HV) compared to the MMC. This may be due to the brittleness of the WC particles which would fracture when abraded by the harder SiC, increasing wear loss [27].

For steel substrates coated with various wear-resistant alloys (non Ni-based), the wear damage during dry sand rubber wheel testing (ASTM-G65) was more severe in high stress than in low stress abrasion wear, however, the wear rate did not linearly increase with load when high loads were applied [28]. It was suggested that the transition occurs because the asperities in the silica sand

responsible for the cutting action had been fractured and smoothed out (Figure 1.5) by the higher loading (which was greater than the compression strength of quartz) [25, 28].
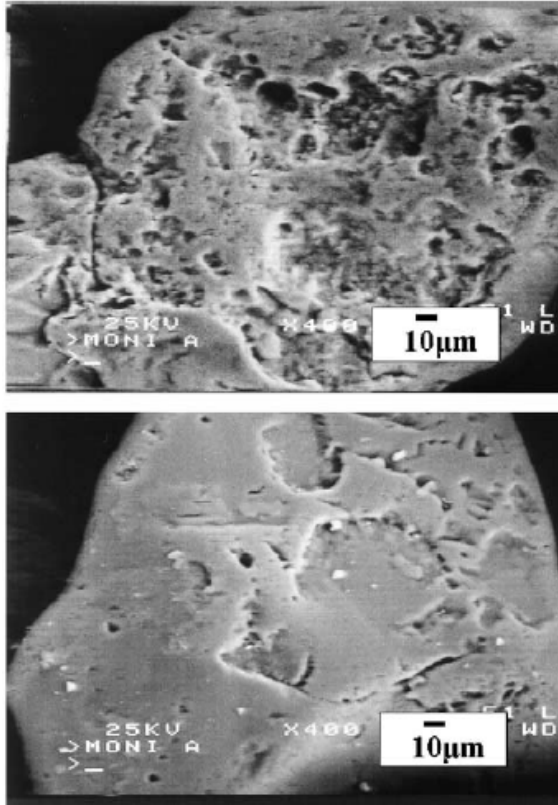
Figure 1.5. Unused (top) and used (bottom) silica sand from dry sand rubber wheel testing (ASTM-G65). [28]

To observe the effects of temperature on wear, two NiCrBSi coatings, one *without WC* (Ni–15.2%Cr–3.1%B–4%Si–3.6%Fe–0.6wt%C) and one *with WC* (44%Ni–11%Cr–2.5%B–2.5%Si–2.5%Fe–2.5%C–35%WC) were deposited on a steel substrate by plasma spraying in tests by Martin et al. [29]. Following deposition, sliding wear tests (rubbing a 99.5% purity alumina cylinder against the specimen surface in an oscillating friction) at 20°C, 250°C, and 500°C showed that wear rates were actually lower at higher temperatures for the deposit without WC. This was due to the transfer of soft material to the alumina cylinder at higher temperatures which covered the abrasive alumina causing it to lose its abrasive surface. The wear rate did not vary greatly for the deposit with WC and the WC did not have a significant impact on the wear rates [29].

It is generally understood that increasing the hard particle fraction will increase coating hardness and hence abrasive wear resistance. It was found that for laser deposited Ni-based alloys with WC particles, increasing the WC volume fraction from 0 to ~50% did indeed show a linear dependence of hardness on the concentration of carbides but there was no correlation with the size of the particles [30]. Compressive residual stresses in the matrix are desired for good cohesion of the particles with the surrounding matrix (while tensile stresses have shown to reduce abrasive wear resistance in thermally sprayed WC-Co coatings [31]) and it was found that the internal stress state of the Ni matrix was not affected by the concentration or size of the carbide [30]. Ball-on-disc wear testing showed that smaller carbides were more effective for dry sliding wear resistance since coatings with large carbides revealed evidence of cracks at the interface between carbides and matrix [30]. Subsequently during ball cratering tests (low load abrasive wear), wear was shown to be caused by three body abrasion of SiC particles between the ball and sample surfaces and the Ni matrix was preferentially worn away and WC/W_2C carbides were intact and rose well above the matrix. Further wear testing with abrasion on coarse SiC paper (high load two-body wear) showed grooves carved out of both the matrix and the WC particles [30].

To gauge the effect of morphology of the WC particles (spherical or angular) on wear rate, a WC-Ni-Al (69.5% WC–29.5% Ni–1%Al) powder was deposited by laser. It was found that the wear rate (tested on an ASTM-G65 dry sand rubber wheel apparatus) of clad layers formed by angular WC powder was up to 50% lower than those obtained with spherical powder (ie. the angular WC had higher wear resistance). The surfaces of the clad layer formed with spherical powder after abrasive wear testing is shown in Figure 1.6.
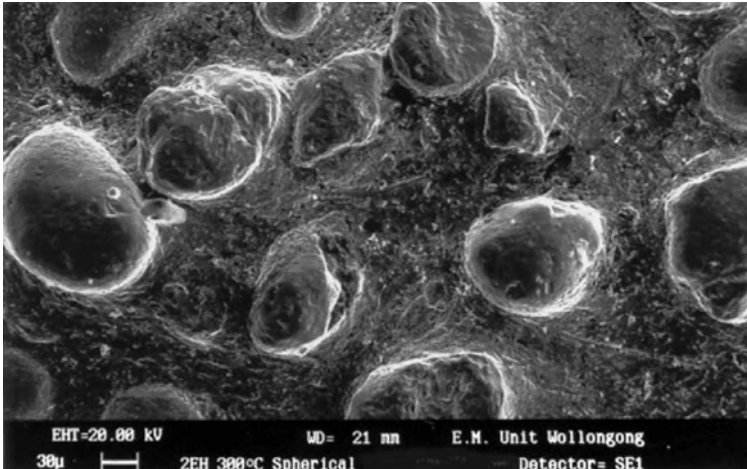
Figure 1.6. SEM micrograph of laser clad spherical WC-Ni formed with 300°C pre-heat. [8]

Analysis of Figure 1.6 indicated that the predominant wear mechanism is removal of the Ni alloy binder phase. The WC particles were essentially intact with no evidence of fracture or particle pull-out. The worn surface of the clad layers formed with crushed powder is shown in Figure 1.7 and was found to display an interlocking carbide structure with very little of the matrix phase exposed which led to better wear resistance than obtained with the spherical carbides. This effect however may change with the size of the WC particles (spherical or angular) as smaller carbides will be able to group together more closely and form a coating similar in structure to the one in Figure 1.7 regardless of WC shape. [8]
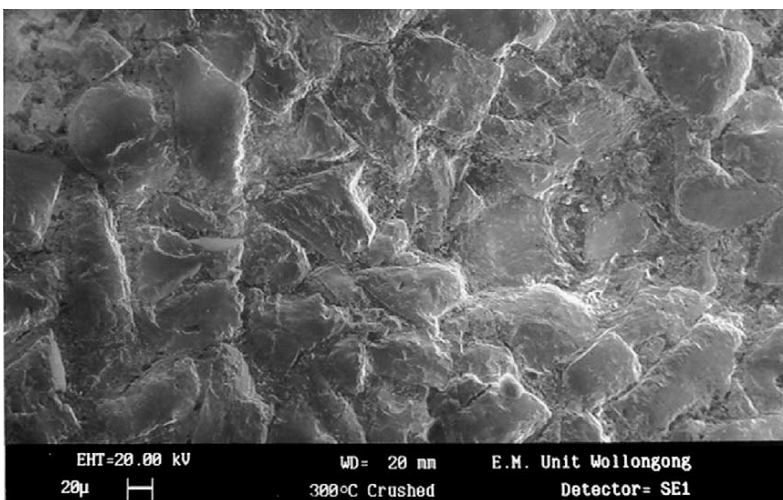
Figure 1.7. SEM micrograph of laser clad crushed WC-Ni formed with 300°C pre-heat. [8]

1.3. Microstructural Features of Nickel Matrix Alloy Overlays

The NiCrBSi and NiBSi alloy based overlays typically have a microstructure comprised of Ni dendrites along with silicides, carbides, and borides [7]. The volume fraction of the primary Ni-phase dendrites ranges from 40-80% and the interdendritic regions contain the particles rich in silicon, carbon, and boron which segregate to the interdendritic region during solidification and precipitate out.

Lebaili et al. tested the microstructural evolution of 11 different NiCrBSi and NiBSi alloys by button melting in an argon arc furnace followed by quenching [15]. Differential thermal analysis (DTA) and TEM analysis was used to find the transition temperatures and identify phases, respectively. The transition temperatures and phases observed are presented in Figure 1.8. The most common phases were found to be γ-Ni, M_7C_3 carbides, CrB and Ni_3B borides, and Ni_5Si_2 silicides [15]. These phases have also been observed in other literature using a variety of Ni-based alloys and welding methods.

Alloy	Cr (at. %)	B (at. %)	Si (at. %)	C (at. %)	Transition temperatures (°C)	Phases in order of appearance
1	–	10	–	–	1280 1095	Ni(α) Ni_3B
2	–	15	–	–	1185 1095	Ni(α) Ni_3B
3	–	–	19	~	1225 1160 1125 1008	Ni(α) Ni_5Si_2
4	–	6	4.5	–	1275 915 885	Ni(α) Ni_3B
5	–	10	10	–	1120 1030 985	Ni(α) Ni_3B Ni_5Si_2
6*	7.5	8	6.3	1	1175 975 985	Ni(α) Ni_3B Ni_5Si_2
7	–	15	10	–	1030 1010 1000 985	Ni_3B Ni_6Si_2B Ni
8*	14	14	6.3	1.5	1025 990 955	CrB Ni M_7C_3 Ni_3B Ni_5Si_2
9*	11	20	8	1.5	1040 960 940	CrB Ni M_7C_3 Ni_3B Ni_5Si_2
10*	10	10	7	2	1075 976 955	M_7C_3 Ni Ni_3B Ni_5Si_2
11*	15	17	7	3.6	1030 970 948 933	M_7C_3 Ni Ni_3B Ni_5Si_2

Figure 1.8. Transformation temperatures and phases formed for each alloy in the order of their appearance. [15]

According to XRD analysis of a NiCrBSi (Ni–15.7%Cr–3.35%B–4.27%Si–4.08%Fe–0.81%C) coating deposited by HVOF, the composition of the coating was a γ-Ni solid solution with small amounts of Ni_3B and Cr_7C_3 phases [20] (similar to what is reported in [32]). Some $NiCr_2O_4$ was also present [20] but

that was most likely a result of oxidation during the HVOF process and is not expected to be present for the PTAW process which uses Ar shielding gas.

The formation of various borides and carbides varies with alloy chemistry and deposition method. For example, XRD analysis of a NiCrBSi (Ni–13.1%Cr–3.6%Fe–0.1%Co–2.2% others) coating deposited by HVOF resulted in strong γ-Ni solid solution peaks with weaker peaks of Ni_3B and CrB [33]. Sidhu et al. reported similar findings in HVOF sprayed coatings but did not report CrB and instead found Cr_7C_3 [20]. Thermal spraying of a NiCrBSi alloy resulted in Cr-rich particles of Cr_7C_3, Cr_3C_2 and CrB as shown by XRD analysis [14]. There is also a potential to form amorphous phases due to the boron and very high cooling rates of individual splats encountered in HVOF [32, 34-35].

The formation of various phases may also occur at high temperatures in these alloys. For example, when a NiCrBSi (Ni–16.3%Cr–3.3%B–4.3%Si–4.2%Fe–0.9%C) alloy was flame sprayed onto a steel substrate, XRD analysis revealed the existence of γ-Ni, Ni_3B in the as-sprayed condition [27]. After fusing the as-sprayed coating at 1065°C, XRD and EPMA confirmed the presence of γ-Ni, Ni_3B, CrB, Cr_7C_3, and Ni/Ni_5Si_2 eutectic [27]. PTAW and laser cladding of similar NiCrBSi alloys resulted in similar phases detected [18, 36-37].

Since these various transformations may occur, some remelting techniques have been examined to determine their influence on the alloy microstructure. Flame spray followed by flame remelting of a NiCrBSi alloy (Ni–15.7%Cr–3.35%B–4.27%Si–4.08%Fe–0.81%C) promotes the formation of a uniform distribution of chromium borides and carbides, a γ-Ni solid solution, and a eutectic phase γ-Ni/Ni_3B [38]. Flame spray followed by laser remelting instead produced a microstructure similar to the flame remelted coating but the matrix phase exhibited a dendritic structure and a lamellar eutectic consisting mainly of Ni with small amounts of Si. Several scattered precipitates with a high concentration of Cr were also produced which were identified as chromium carbides and chromium borides. It was also noted that Cr_7C_3 mainly formed when the alloy contained approximately 0.6% C, and mainly Cr_3C_2 if the alloy had a

carbon content >0.8%. As a comparison, laser cladding of the same alloy resulted in large CrB particles, the γ-Ni phase, and the γ-Ni/Ni$_3$B lamellar eutectic [38].

During laser cladding of NiCrBSi the presence of Ni$_3$Fe, Ni$_3$Si, B$_4$C, CrB, Cr$_3$Si, Cr$_{23}$C$_6$ and (Fe,Ni)$_{23}$C$_6$ particles have been noted by XRD analysis, though the microstructure mainly consisted of γ-Ni dendrites with γ-Ni/Ni$_3$B eutectic containing small amounts Ni$_3$Fe and Ni$_3$S in the interdendritic lamellae [39]. However, the majority of particles in deposits formed by laser cladding are carbides or borides. For example, EDX analysis of a NiCrBSi (Ni–15.3%Cr–3.1%B–4.8%Si–4.2%Fe–0.6%C) coating formed by laser cladding, the microstructure consisted of a dendritic Ni solid solution phase ("A" in Figure 1.9) with a metastable Ni$_3$B eutectic. The interdendritic phase ("B" in Figure 1.9) is a Ni-Si laminar eutectic and there are also precipitates of Cr: most likely CrB (darker precipitates, "C" in Figure 1.9) and Cr$_7$C$_3$ or Cr$_3$C$_2$ (grey precipitates, "D" in Figure 1.9) [40]. These results are in good agreement with the results from HVOF and other laser clad coatings and so a similar microstructure is expected in the PTAW process, however the morphology and distribution of these phases may differ due to the different thermal cycles attained in PTAW.
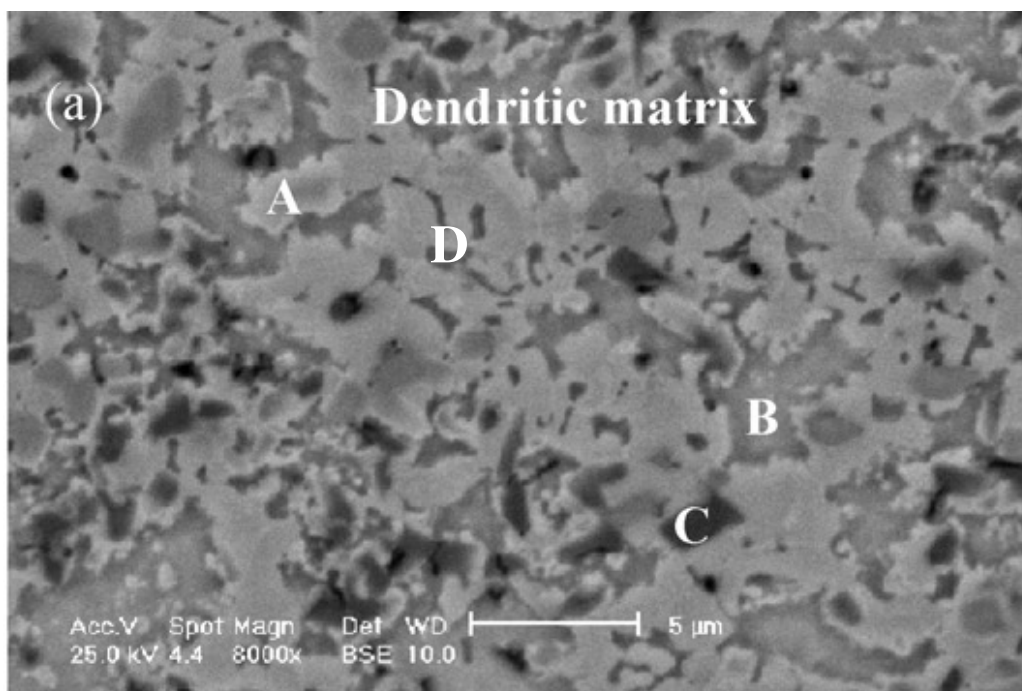
Figure 1.9. SEM microstructure of a NiCrBSi coating made with laser cladding. [40]

It should be noted that these phases may also occur in the initial powder base material, however they may dissolve and reprecipitate at high temperature in different quantities during deposition. For example, a NiCrBSi (Ni–14%Cr–3.2%B–4.5%Si–4.5%Fe–0.55%C) alloy powder consisted of the following before welding: γ-Ni, Cr_7C_3, Cr_3C_2, and Cr_2B. After PTA welding, XRD scans contained peaks corresponding to the γ-Ni phase along with other phases like Cr_2B, Cr_3C_2 and Cr_7C_3 which was similar to the original powder except for a significant increase in the Cr_3C_2 peak intensity [5]. This is actually the preferred chromium carbide form for wear resistance as it is the one with the highest hardness [41-42]). The dissolution of these phases in the powder base material is also important in solution strengthening, since Yan et al. reported that chromium, boron and silicon dissolved in the γ-Ni matrix and provided added strengthening and hardening after surface remelting of a high-Cr NiCrBSi alloy (Ni–25.66%Cr–2.82%B–3.41%Si–<5%Fe–0.6%C) [12].

During welding, segregation of elements plays a major role in the development of the solidified microstructure. For example, EDX analysis

indicated that the γ-Ni primary dendrites are rich in Si and Fe, while it is depleted in Cr which is likely concentrated in the Cr-rich particles in the interdendritic regions [25]. XRD analysis showed the deposit consisted mainly of γ-Ni, $(Cr,Fe)_7C_3$, CrB and Ni_3B [25]. In addition PTA welding of a high-Cr alloy (12.44% Cr) resulted in the γ-Ni dendritic phase having around 10% of Cr in solid solution [1].

1.4. *Hardness and Wear Properties of Nickel Overlay Alloys*

The hardness and wear resistance of alloys without reinforcing particles is expected to be governed by the presence of hard phases since abrasive wear resistance correlates well with hardness [34]. Consequently, Cr-rich carbides and borides, as well as eutectic phases such as Ni_3B and Ni_3Si are important to the overall properties. Some of those phases can be very hard (eg. Cr_3C_2 has a hardness of 1400HV [43] or Ni_3B at about 1000HV [44]), and even approach values comparable to the hardness of reinforcing particles used in MMCs. In addition, for very hard matrix alloys, ductility may decrease and so fracture can play an important role by diminishing the ability of the alloy to undergo plastic deformation and absorb impact energy.

The ductile γ-Ni-phase primary dendrites are prone to adhesive wear and so reducing their volume fraction is expected to improve the wear resistance. However, increasing the fraction of the brittle interdendritic regions can have a detrimental impact on the toughness of the deposits since the ductile primary dendrites promote crack-bridging and toughening. A higher Si:B ratio results in a greater tendency to form Ni/Ni_3Si eutectic which is tougher than the Ni/Ni_3B eutectic [7]. It was found that in fracture testing of several NiCrBSi alloys, the lowest toughness values were observed for an alloy with a Si:B ratio < 3.3 and low iron content produced the highest toughness values [7]. Cleavage fracture

was found in the interdendritic regions while necking and plastic deformation (dimpling) were observed in the dendrites after fracture. The addition of iron resulted in an increase in the dendrite volume fraction but also resulted in the formation of large precipitates (assumed to be brittle carbides, borides, or silicides) in the interdendritic regions [7]. The presence of these precipitates hampered the positive effect the higher dendrite volume fraction would have on the fracture toughness [7, 11].

In a PTA welded NiCrBSi alloy (Ni–16.64%Cr–4.02%B–4.28%Si–3.48%Fe–0.67%C), it was found that coarser Cr- carbides and borides survived dry sand rubber wheel wear tests (ASTM-G65) whereas the finer precipitates were detached from the matrix. In this instance, the size of the hard particles was a more critical factor in abrasive wear resistance than hardness because the test sand was coarser and softer than the borides and carbides. [18]

Wear tests conducted according to the ASTM G77 standard (block on ring sliding wear) on flame sprayed (and laser remelted) versus laser clad coatings of NiCrBSi indicated that there were no significant differences in the wear rates between the different coatings [38, 45]. The presence of iron oxides on almost all of the surfaces of the coatings that were tested decreased along with the friction coefficient when the load was increased. This suggests a regime of oxidative wear, in which the increased interface temperature induced during sliding produces an oxide film, which protects the underlying surface by reducing the wear rate and the oxide itself determines the coefficient of friction. Wear was observed to be predominantly adhesive (material transfer between abrading surfaces) in the test carried out at the highest loads since the rate of oxide film formation would be lower than its rate of removal [38, 45-46].

In general, laser and HVOF deposition methods provide higher hardness than PTA overlays since the higher cooling rates result in a finer microstructure. In fact, it has been argued that some nanocrystalline or amorphous phases account for this increased hardness [34]. From the various tests shown for high-Cr alloys in Table 1.1, the average hardness value for laser cladding was 740HV, while for HVOF it was 790HV, and for PTAW it was 550HV. As a result, in abrasive wear

testing the laser and HVOF sprayed deposits are expected to perform better than PTAW deposits.

Table 1.1. Reported hardness values for NiCrBSi alloys formed by various deposition methods.

Alloy Composition	Deposition method	Hardness	Ref.
Ni–15.7%Cr–3.35%B–4.27%Si–4.08%Fe–0.81%C	Laser remelting	$900HV_{100\,g}$	[45]
Ni–13.5%Cr–3%B–4.2%Si–4.7%Fe–0.75%C	HVOF	$700HV_{500g}$	[47]
Ni–21%Cr–4%B–5.3%Si–5%Fe–0.6%C	HVOF	$905HV_{200g}$	[34]
Ni–14%Cr–3.2%B–4.5%Si–4.5%Fe–0.55%C	PTAW	$700HV_{25g}$	[5]
Ni–14.56%Cr–3.37%B–4.28%Si–3.8%Fe–0.73%C	Laser	730HV	[36]
Ni–14.56%Cr–3.37%B–4.28%Si–3.8%Fe–0.73%C	PTAW	500HV	[36]
Ni–15.3%Cr–3.1%B–4.8%Si–4.2%Fe–0.6%C	HVOF	$750HV_{15g}$-$930HV_{15g}$ (different substrates)	[20]
Ni–15.7%Cr–3.35%B–4.27%Si–4.08%Fe–0.81%C	Laser	$800HV_{100g}$	[25]
Ni–15.7%Cr–3.35%B–4.27%Si–4.08%Fe–0.81%C	Flame spray	$800HV_{100g}$	[25]
Ni–7.5%Cr–1.6%B–3.5%Si–2.5%Fe–0.25%C	Laser	$500HV_{1kg}$	[6]
Ni–15%Cr–3.1%B–4.3%Si–3.5%Fe–0.75%C	Laser	$700HV_{1kg}$	[6]
Ni–16%Cr–4%B–4%Si–2.5%Fe–0.5%C	Laser	550HV	[17]
Ni–2.5%B–3.3%Si–1.2%Fe–0.1%C	PTAW	$525HV_{200g}$ (avg. for 2 welding currents)	[48]
Ni–16.64%Cr–4.02%B–4.28%Si–3.48%Fe–0.67%C	PTAW	$600HV_{1kg}$	[18]

1.5.   Ni-WC MMC Overlays

The abrasive wear resistance increases strongly with the addition of tungsten carbides WC in the metallic matrix [3, 30]. As a result, WC particles with either a spherical or angular morphology (shown in Figure 1.10) are an ideal candidate for addition into Ni-based alloys as the reinforcing phase. The low melting point of the NiCrBSi alloys (about 1025°C) allows tungsten carbide to endure the deposition process more readily than Fe-based matrix alloys [41], In fact, it is a major challenge to incorporate a high fraction of WC particles to a metal matrix, since these may undergo complete dissolution, or only partially decompose and decarburize when heated to form W_2C. This type of tungsten carbide is more brittle than WC, and so its presence will degrade the coating wear properties [27].
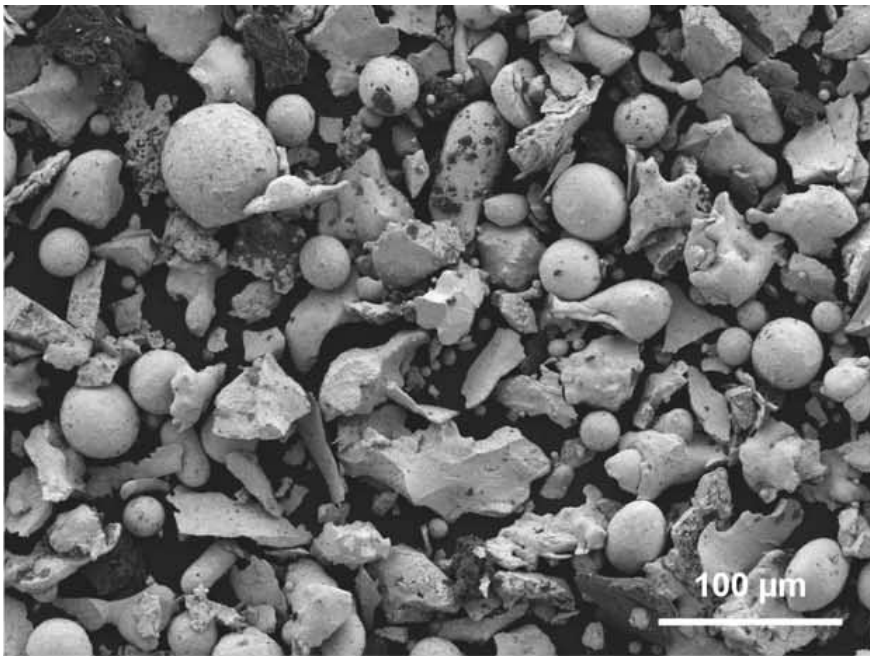

Figure 1.10. Spherical and angular WC particles. [30]

Laser cladding of a NiCrBSi alloy (Ni–16%Cr–3.5%B–4.5%Si–1.2%Fe–0.8%C) with WC particles results in a matrix microstructure similar to that processed with no WC particles present, since the dissolution of WC particles is very low (~5%) using the laser cladding process [49]. The matrix was composed

of γ-Ni dendrites and γ-Ni + Ni_3B lamellar eutectic in the interdendritic region. Blocky precipitates formed both near and away from the WC-matrix interface were found to be β-W_2C and contained some Cr. Quadrilateral precipitates were found to be η_1-M_6C with some Cr and Ni (possibly $(Cr,Ni)_3W_3C$) and thin-plate carbides were found to be α-W_2C [49]. Other intermetallics bearing W and C are formed at high temperature when the WC particles dissolve. For example, after fusing a NiCrBSi (46%Ni–11%Cr–2.5%B–2.5%Si–2.5%Fe–0.5%C–35%WC-Co) alloy at 1090°C, XRD and EPMA confirmed the presence of γ-Ni, Ni_3B, CrB, Cr_7C_3, WC, W_2B, and Co_6W_6C, whereas only γ-Ni, Ni_3B, and WC were detected in the as-sprayed coating. [27]

In order to prevent precipitation of brittle hard phases during laser welding, it was found that alloys with low contents of carbon, boron, and chromium should be used [21]. The low matrix hardness (higher ductility) of these low alloyed materials did not increase the wear rate significantly as a ductile matrix is superior in preventing particle pull-out during abrasive wear. To prevent cracking a matrix with fewer precipitated hard phases is desired and in general the hardness of the matrix should ideally be less than 600 HV [21].

Complex carbides such as the metastable and extremely brittle η phase M_3W_3C form in MMCs due to the low carbon concentration in matrix alloys and the rapid cooling of the melt when WC is used as reinforcing particles [21]. It is believed that if these complex carbides embrittle the matrix at a critical matrix hardness level, it prevents the matrix alloy from accommodating shrinkage strains during solidification, and cracks occur during cooling [21].

Deposit cracking is a problem inherent to many welding processes and is exacerbated by use of hard matrix alloys with WC particles which can act as initiation sites [50]. This has also been observed in WC-Ni-Al powders deposited by laser using spherical and crushed WC particles, where clad layers produced without preheating of the substrate contained cracks while preheating the substrate to 300°C completely eliminated all the cracks [8]. The elimination of cracks was attributed to the reduction in thermal mismatch between the clad layer and substrate which leads to lower thermal stress and in turn reduces cracking [8].

Similarly, for several high- and low-Cr NiCrBSi alloys reinforced with WC by laser deposition, all claddings contained some cracks perpendicular to the laser travel direction [41]. The cracks were caused by a hard matrix (embrittled by dissolution of carbides resulting in brittle W and C-containing secondary phases) combined with the WC carbides which can act as crack initiation sites. A softer matrix material, better parameter control to avoid carbide dissolution or preheating of the component was advised to decrease the cracking behaviour [41].

1.6. *WC Carbide Dissolution during Deposition of Ni-WC MMCs*

Dissolution of primary WC carbides can be a major problem in Ni-WC MMCs because the high temperatures attained and chemical driving force promote dissolution of the WC particles. In addition, the subsequent reprecipitation of secondary carbide phases containing W and C which may be detrimental to the mechanical properties of the coating. Carbide shape also plays a role in dissolution as it was found that that angular WC showed slightly less dissolution than spherical [41]. However, there is a tradeoff, in that using spherical rather than angular particles may help in preventing cracks as the cracks can initiate at sharp edges [30]. Further, using coarse rather than fine WC particles minimizes the decarburization of WC which would form W_2C [51].

Interface reactions take place between carbides and the matrix during MMC deposition and bind the carbides to the matrix which can influence the mechanical behaviour of the hardfacing overlay. It has been shown previously that greater heat input into the weld leads to higher dissolution of carbides. The interface forms by either melting with subsequent diffusion or pure diffusion without melting of the carbide [48]. The diffusion coefficient of carbon in the matrix material is usually higher than the diffusion coefficient of the carbide-forming metal [48]. Thus carbon diffuses much faster out of the carbide, allowing it to form mixed carbides at the interface.

The influence of the chemical composition of the matrix on WC/matrix interface reactions was shown for a Fe-based matrix with WC particles. During tungsten inert gas welding of those alloys, alloying elements which led to greater dissolution were Fe, W, Cr and Mo, while C content had a minor effect on the dissolution [48, 52]. X-ray analysis of HVOF sprayed WC-Cr and WC-Ni coatings showed that chromium did not significantly change the amount of WC dissolution [53]. XRD and TEM analysis showed that the addition of chromium to WC-Co coatings prevents the formation of metallic tungsten and favours the formation of other mixed compounds [54].

In terms of the phases that form after carbide dissolution, it was reported that the heterogeneous nucleation of Ni_3B is enhanced on the surface of WC particles [55]. In addition, in the interface between WC particles and the matrix, M_6C tends to form as well as low amounts of Fe_3W_3C [16]. Away from the WC/matrix interface, more complex carbides have also been found in NiCrBSi alloys containing W; their chemistry was found to follow the formula $(NiSi)_A(CrW)_B$, with A and B taking values in the ranges (2.5-2.9) and (2.5-3.6), respectively [16].

An alloy deposited by thermal spraying and laser remelting containing 50 vol.% WC particles in addition to the NiCrBSi matrix (Ni–10%Cr–2.1%B–2.8%Si–14%Fe–0.1%C) was found to consist of WC particles, Ni_2W_4C, and Ni-Cr-Fe [56]. It was possible for the coating not to contain any evidence of WC particles depending on the laser power used for remelting [56].

When several Ni-base alloys with WC particles were deposited by laser on steel substrates so that the weld pool surface exceeded 3273K and alloy/substrate temperature was about 1788K, very little dissolution of the WC particles are observed, however they would dissolve completely if the W and C concentrations in the bulk alloy are reduced [57]. Thermodynamic calculations suggested that the terminal solidification temperature would be about 1617K and could contain austenite, WC particles, and graphite once solidified. It was also suggested that at slower laser traveling speeds, enrichment of the interparticle region with carbon

from dissolved WC results in the eutectic formation of austenite and carbide from liquid [57].

Thermal spray deposition of a NiCrBSi (Ni–7.6%Cr–1.6%B–3.6%Si–2.4%Fe–0.25%C) alloy with WC particles (10% and 40%) alloy resulted in XRD peaks for Cr_7C_3, secondary tungsten carbide W_2C and metallic tungsten (W), Cr_3Ni_2, and $Cr_{23}C_6$ [58]. Heat treating for 1 h at 1200°C resulted in a number of complex tungsten carbide phases: Ni_2W_4C, FeW_3C, Fe_6W_6C were produced by the consumption of primary tungsten carbide (WC), secondary tungsten carbide (W_2C), and metallic tungsten (W). There was also evidence of nickel boride (Ni_4B_3), chromium borides (CrB_6, Cr_2B_3), and chromium carbides (Cr_3C_2, Cr_7C_3) [58]. Laser cladding of spherical WC-Ni (29.5%Ni–1%Al–69.5%WC) alloy showed XRD peaks corresponding to γ-Ni, WC, W_2C and WC_{1-X}, Ni_2W_4C and CrFeNi. The latter two phases were a result of dissolution of WC particles and substrate dilution (some Cr in substrate) [8]. When PTAW was used to deposit two NiCrBSi alloys with WC hard particles, dissolution of WC was evidenced by the presence of elongated precipitates rich in W next to the WC particles and a small concentration of W in solid solution [1]. Dissolution of WC carbides also was noticed for a laser clad MMC (75%Ni-25%WC) alloy [59].

1.7. Hardness and Wear of Ni-WC MMCs

It was found that even a 5 vol% addition of WC is sufficient to lower wear by a factor of 10 for several Ni/WC MMCs [30]. For flame-sprayed and fused Ni-based coatings, adding 35% WC-Co to NiCrBSiC powder gave the best coating quality in terms of hardness and porosity [27] and it was found that 40% WC addition showed the best wear resistance for dry sand rubber wheel (DSRW) abrasive wear testing [27]. It was determined that weight loss of the base metal decreased by 59% during wear testing compared to a NiCrBSi coating (without WC) while it decreased a further 61% with the addition of 35% WC but did not

noticeably decrease the wear with >60% WC [13]. The volume fraction of carbides was found to have only a minor effect on the wear rate in the WC fraction from 40% to 60%, since this increase only yielded a minor ~5% decrease in wear loss which was within experimental error [23, 60]. It was also shown that the inter-particle distance had a large effect on wear as large inter-particle distances lead to more gouging of the matrix and particle pull-out [61].

Fine carbides have been found to undergo more WC dissolution likely due to the higher degree of overheating related to the greater surface-to-volume ratio [53]. As a result, it is expected that higher dissolution would result in more deterioration of mechanical strength and that they would be physically too small to resist and deflect the abrasive particles. Thus, smaller carbides would be limited to dispersion strengthening of the matrix (increasing hardness) to reduce scratch depth and material loss [53].

NiBSi coatings with single-crystal Ni coated WC particles resulted in contiguous particles compared to agglomerated and sintered WC particles which resulted in an inhomogeneous and clustered distribution of the WC particles [60]. The abrasion resistance was higher for the deposit containing single crystal WC as finer and contiguous particles resulted in a lower abrasion rate [60].

For NiCrBSi + WC alloys deposited by metal active gas welding, the predominant wear mechanism under combined impact and abrasion was mainly erosion of the matrix and WC particles with neither the hard particles nor the matrix/particle interfaces showing signs of failure [3]. A higher coating microhardness was found to be beneficial for erosive material loss and a finer distribution of hard phases was found to be beneficial for toughness during low energy impacts. Increasing the impact loading energy caused a large increase in wear as there was much more plastic deformation of the matrix and fracture of the carbides occurs. In subsequent 3-body abrasion tests (ASTM-G65 tumbler), the primary wear mechanism was removal of carbides, which then resulted in removal of matrix material [3].

Laser welding of a NiCrBSi alloy (Ni–16%Cr–4%B–4%Si–2.5%Fe–0.5%C) with 25% and 50% WC particles resulted in hardness values of

approximately 800HV and 1100HV, respectively [17]. The hardness of a thermal-spray deposited NiCrBSi (Ni–7.6%Cr–1.6%B–3.6%Si–2.4%Fe–0.25%C) alloy with 90% WC was found to be about $1400HV_{300g}$ [58].

When PTA overlay welding of a NiCrBSi alloy composites is conducted with 4 different sizes of WC particles, almost identical microhardness values are obtained (about $1000HV_{1kg}$) [62].

Table 1.2. Reported hardness values for NiCrBSi +WC alloys formed by various deposition methods.

Alloy Composition	Deposition method	Hardness	Ref.
Ni–16%Cr–4%B–4%Si–2.5%Fe–0.5%C + 25% WC	Laser	800HV	[17]
Ni–16%Cr–4%B–4%Si–2.5%Fe–0.5%C + 50% WC	Laser	1100HV	[17]
Ni–11.3%Cr–3%B–3.8%Si–2.36%Fe–0.58%C + 65% WC	PTAW	$1000HV_{1kg}$	[62]

1.8.   Purpose of this Thesis

A wide range of NiCrBSi alloy chemistries are available which yield various degrees of hardness and wear resistance, however there is a limited understanding of the correlation between the composition, microstructure and properties of these materials. These alloys have been largely developed for oxyfuel and other thermal spraying processes where the peak temperatures are limited, and so the formation of low melting point phases (such as eutectics involving Ni_3B and Ni_3Si) are desired. However, this is not necessarily a requirement for the PTAW process since much higher temperatures of >20,000 K are readily produced within the constricted arc [63]. As such, there is a need to

reassess the role of melting point suppressing elements, such as B and Si [3] during PTAW of these alloys. In addition, although the chemistry of a NiCrBSi may be optimized for peak hardness or wear resistance as a Ni-alloy overlay, the influence of alloy elements (including carbon and Cr) may be very different when the alloy is used in a Ni-WC composite. In the present work, the microstructures and properties in two commercial NiCrBSi alloys are examined with similar Cr content in order to determine the influence of alloying constituents. The performance of a wide range of Ni-alloys is also compared in terms of wear resistance, WC dissolution, and hardness versus chemistry in order to determine the influence of alloying elements in the composite coatings. Quantitative microscopy is used to compare the volume fractions of various phases, and this is correlated to the coating properties.

2. Experimental Work

2.1. Alloy and PTAW Information

The NiCrBSi and NiBSi matrix alloys studied are listed in Table 2.1, and the chemical compositions given in Table 2.2. Each of these were deposited using PTAW as both a Ni-alloy overlay, as well as part of the metal matrix phase in a MMC overlay. The nominal compositions for the powders materials before welding were available for only a few of the alloys, as shown in Table 2.3. However, these powder chemistries are only shown for comparison purposes, and it should be noted that the alloy chemistry may change during PTAW due to loss of some elements as a result of fume generation in the arc. The PTAW system used was a Stellite Starweld System 300M with an Excalibur torch with a tungsten electrode of 3/16 inch diameter.

Table 2.1. List of Ni-alloys examined.

Supplier	Alloy	Powder type	Hardness
Colmonoy	Colmonoy 4	NiCrBSi	40 HRC
Colmonoy	Colmonoy 5	NiCrBSi	50 HRC
Colmonoy	Colmonoy 6	NiCrBSi	60 HRC
Deloro Stellite	Deloro 30	NiCrBSi	30 HRC
Deloro Stellite	Deloro 40	NiCrBSi	40 HRC
Deloro Stellite	Deloro 50	NiCrBSi	50 HRC
Carpenter	B40	NiCrBSi	40 HRC
Carpenter	B50	NiCrBSi	50 HRC
Carpenter	B60	NiCrBSi	60 HRC
Hoganas	1535	NiCrBSi	30 HRC
Hoganas	1536-40	NiCrBSi	40 HRC
Hoganas	1550	NiCrBSi	50 HRC
Hoganas	1560-00	NiCrBSi	60 HRC
Hoganas	1559-SP329 (Cr-free)	NiBSi	50 HRC

Table 2.2. Chemical composition of Ni-alloy overlays studied (in wt%).

Alloy	B	C	Cr	Fe	Ni	Si
Deloro 30	1.25	0.11	8.63	2.7	84.17	3.14
Deloro 40	1.57	0.21	7.03	3.23	84.17	3.79
Deloro 50	1.98	0.42	9.28	4.49	79.89	3.94
Colmonoy 4	1.93	0.67	8.39	5.2	79.79	4.02
Colmonoy 5	1.65	0.52	12.23	5.16	75.93	4.51
Colmonoy 6	2.73	0.92	13.8	5.5	71.25	5.8
Carpenter B40	1.89	0.18	8.38	4.88	81.68	2.99
Carpenter B50	2.9	0.42	8.62	8.25	76.15	3.66
Hoganas H1535	1.26	0.22	5.25	2.48	87.87	2.92
Hoganas H1536-40	1.57	0.09	4.47	0.87	90.22	2.78
Hoganas 1550	2.71	0.44	8.17	4.45	80.33	3.9
Hoganas 1560-00	3.55	0.75	12.2	4.49	74.68	4.33
Hoganas 1559-SP329 (Cr-free)	3.45	0.027	0.16	0.64	92.643	3.08

Table 2.3. Nominal composition of some of the powders (in wt%).

Alloy	B	C	Cr	Fe	Ni	Si
Deloro 30	1.4	0.3	8.0	2.2	84.9	3.2
Deloro 50	2.0	0.45	10.5	4.0	79.05	4.0
Carpenter B40	1.6	0.3	7.0	2.9	84.8	3.4
Carpenter B50	2.4	0.5	11.6	4.4	77.4	3.7

The matrix alloy powders were spherical in shape with a size distribution of 50 to 180 μm and an average of 100 μm. The matrix coatings were applied with PTAW parameters as follows: arc voltage of 25 V, current of 140 to 150 A (in DC electrode negative polarity), powder feed rate of 25 g/min, Ar gas shielding at a flow rate of 12 l/min, 14 mm working distance, and a travel speed of 0.6 mm/s (shown in Table 2.4). The samples were deposited onto hot rolled low carbon steel (prepared by washing in alcohol and then grit blasted to remove mill scale) and the weld overlay dimensions were approximately 25 mm wide by 75 to 100 mm in length.

Table 2.4. PTAW parameters used during deposition of Ni-alloy overlays.

Arc voltage, V	Current, A	Powder feed rate, g/min	Shielding gas flow rate, l/min	Travel speed, mm/s
25	140-150	25	12	0.6

The WC powder used consisted of angular and monocrystalline particles (without any W_2C) with a size distribution of 50 to 180 µm with an average of 100 µm. The MMC powders were mixed as 500g batches (for each alloy) to a ratio of 60wt% monocrystalline WC with 40wt% Ni-alloy (which is approximately 50 vol.%). Powders were mixed on a tumbler for a minimum of 2 hours and the mixed powders were poured directly from the tumbler into the PTAW system hopper to be welded (i.e. without storing between mixing and welding) to minimize any settling effects. The MMC coatings were applied with PTAW parameters as follows: arc voltage of 25 V, current of 150 to 160 A (in DC electrode negative polarity), powder feed rate of 25- to 30 g/min, Ar gas shielding at a flow rate of 12 l/min, 14 mm working distance, and a travel speed of 0.3-0.5 mm/s (shown in Table 2.5). The settings for the MMC deposition used slightly higher current and slower travels speeds (resulting in higher heat input), in order to achieve comparable coating deposition rates and wetting with the substrate since the addition of tungsten carbide to the powder introduces a heat-sink effect whereby some of the heat is retained in the WC particles.

Table 2.5. PTAW parameters used during deposition of Ni-WC composites.

Arc voltage, V	Current (DCEN), A	Powder feed rate, g/min	Shielding gas flow rate, l/min	Travel speed, mm/s
25	150-160	25-30	12	0.3-0.5

2.2. Microscopy

For the matrix alloys the samples were cut (using a diamond reinforced cutting wheel) from the middle of the deposit and ground flat using up to 1200grit wet SiC abrasive, polished with a 1μm diamond suspension and etched for 20-30s with Marble's reagent (with a composition of 1g/l $CuSO_4$, 50vol% HCl, 50vol% water). This etchant leaves hard phases in Ni-based alloys intact while preferentially attacking the nickel. Optical microscopy was conducted following the etching. Scanning electron microscopy (SEM) with energy-dispersive X-ray (EDX) analysis and electron probe microanalysis (EPMA) with wavelength dispersive spectroscopy (WDS) were conducted using a 20keV accelerating voltage to characterize the microstructure of the deposits. Auger Electron Spectroscopy (AES) was also conducted on some samples at an accelerating voltage of 15keV to quantify certain phases contained in the deposits with Ar ion sputtering being done for 30 s prior to analysis (to remove surface contamination). AES provides elemental quantification for small phases since it is a very surface sensitive technique (Auger electrons are emitted only from the first few nanometers of the surface), and consequently does not suffer from undesirable interaction volume effects observed with other SEM methods for analysis of bulk samples.

MMC overlay deposits were cut (using a diamond reinforced cutting wheel) from the middle of the deposit and were then polished using an autopolisher with a diamond impregnated polishing pad (up to 1 μm). This is the preferred method for such MMCs, as the very hard WC particles make it impractical to prepare by conventional methods with SiC abrasive pads. Optical microscopy was performed following the polishing and was used to quantify the WC fractions and examine some of the other phases. EPMA and AES were also used in the same settings as the Ni-alloy analysis to quantify the chemistry of various phases, and SEM microscopy was used to analyze the surface scars produced following wear testing of the MMC deposits.

2.3. Hardness Testing

Vickers microhardness testing was conducted using a Mitutoyo MVK-H1 indentation system, with a 25g to 1 kg load and 15 s load time to determine the average hardness through the coating thickness. When analysis of specific phases was required a 25 or 50g load was used. Unless otherwise noted, hardness values reported for a specific phase represent an average of at least 3 indentations.

2.4. Wear Testing

Wear testing was performed as per the ASTM-G65-04 (Procedure A) standard (dry sand rubber wheel apparatus) and the mass loss results were taken for two consecutive wear scars (following 6000 and then 12000 revolutions of the abrasive wheel) using a 20 N load on the wheel. The abrasive used was Ottawa silica sand in a 50/70 mesh size (200 to 300 μm diameter particle size) with an angular morphology.

Most deposits had a layer devoid of WC at the top of the deposit, and in order to take into account the reduced WC fraction observed in this region, the samples were ground down by 1 to 2 mm before wear testing was performed. Since some settling of the WC towards the substrate is often observed, the 2nd wear scar is the more representative value of the wear performance of the deposit.

3. Ni-Alloy Results

3.1. Optical and SEM Microscopy

PTAW overlays were 5 to 6 mm in thickness and approximately 30 mm wide with no observed porosity in optical micrographs. In general, the microstructural features observed can be grouped into similar hardness values. The typical appearance of each group is shown in Figure 3.1, with the trend of decreasing fractions of primary dendrite γ-Ni phase (or increasing interdendritic phase) with increasing hardness. The 30HRc grade of alloys has a large dendritic volume fraction with very few carbides and borides while the 40HRc grade of alloys has a higher interdendritic volume fraction with some carbides and borides. The alloys with hardness ranging from 50-60HRc were found to have a much higher interdendritic volume fraction than 40HRc alloys with a far greater fraction of carbides and borides
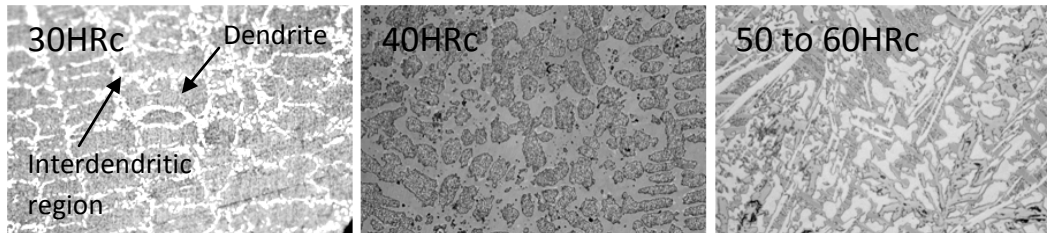
Figure 3.1. Typical microstructural appearance of 30HRc, 40HRc, and 50 to 60HRc matrix alloys deposited by PTAW.

For the purpose of this chapter, the characterization will be mainly focused on two alloys in order to simplify the analysis, with a low-Cr (Deloro 30) and a high-Cr (Deloro 50) alloy being selected for the purpose of comparison, with exact compositions given in Table 2.3. In terms of microstructure, Deloro 30 contained large dendrites of γ-Ni phase, along with fine particles in the inter-dendritic regions, see Figure 3.2(a). In Deloro 50, the γ-Ni phase dendrites were much finer and more difficult to discern (see Figure 3.2(b)), and a significantly larger fraction of blocky, globular, and rhombus shaped particles could be observed in the interdendritic regions (see Figure 3.3(b)). The microstructure of

Deloro 30 is shown using SEM in Figure 3.3(a), and EDX analysis was used to quantify the composition of hardness indents (Table 3.1). For example, the chemistry at the cores of the γ-Ni dendrites in Deloro 30 (e.g. point 1 in Figure 3.3) as well as the interdendritic regions (e.g. points "2" and "3" in Figure 3.3) were determined. Several Cr-based particles could also be detected in the interdendritic regions of Deloro 50 as indicated in Figure 3.3(b), however EDX could not be used to conclusively identify particles containing carbon or boron due to the limitations of the detector, and hence these phases were subsequently identified by a combination of EPMA and AES.
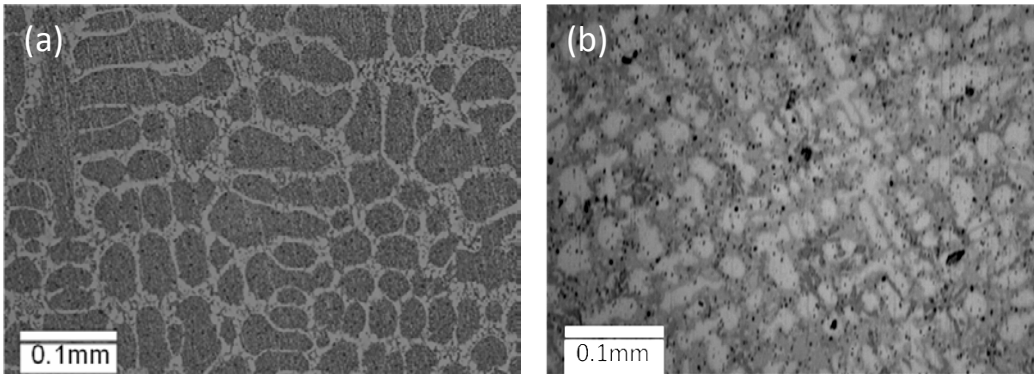
Figure 3.2. Optical micrographs of (a) Deloro 30, and (b) Deloro 50.
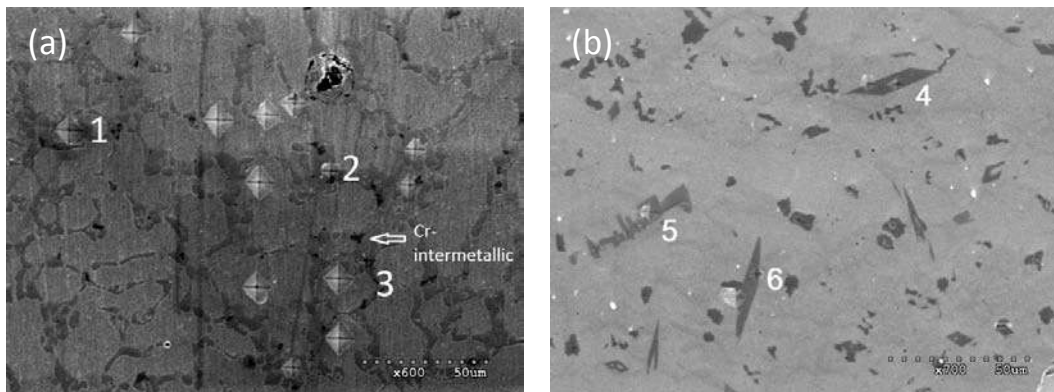
Figure 3.3. (a) SEM image of selected area of Deloro 30. (b) SEM image of selected area of Deloro 50.

Table 3.1. EDX point quantification of locations in Figure 3.3, all in wt%.

Location	Ni	Cr	C	Fe	Si
1	85.5	9.6	0.0	3.1	1.8
2	88.6	7.3	0.0	1.6	2.5
3	83.6	9.6	0.0	1.5	5.3
4	17.5	57.5	22.7	1.0	1.3
5	38.1	42.7	13.0	3.7	2.4
6	10.0	65.3	23.3	0.9	0.6

EDX analysis of Deloro 50 in the interdendritic region is shown in Figure 3.4. The fraction of γ-Ni phase is much lower in Deloro 50, and a number of Cr-carbides could be distinguished within the inter-dendritic regions. EDX analysis of Deloro 50 showed that the precipitates ("4", "5", and "6" in Figure 3.3) were chromium carbides with varying Cr to C ratios, suggesting these may correspond with different phases. The interdendritic regions of both alloys appeared to contain a globular eutectic structure, see Figure 3.4. EDX analysis indicates that the component with lower atomic contrast is enriched in Si. A low Cr content was measured in the interdendritic regions where no particles are present. As mentioned earlier, EDX cannot detect boron, and hence these regions can only be investigated using EPMA and AES.
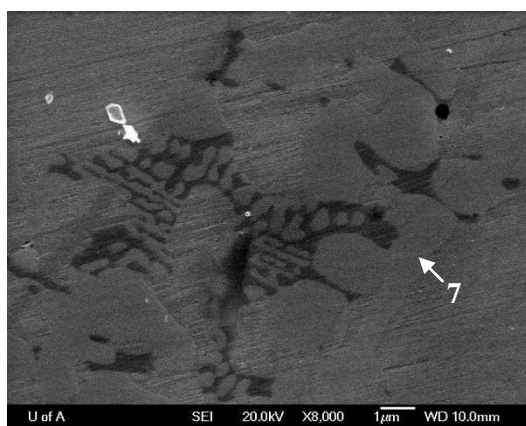
Figure 3.4. SEM image of interdendritic region in Deloro 50, with EDX quantification at location 7 corresponding with 86.2% Ni, 8.4% Si, 3.5% Cr, and 1.9% Fe.

3.2. EPMA and AES Analysis

EPMA element mapping was performed on both alloys in order to identify the phases as well as to quantify their volume fractions. The EPMA maps were collected from the entire coating thickness in a 100 µm wide section near the centerline of the deposit, and image analysis of individual segments 0.5 mm in height was performed in order to quantify the volume of interdendritic areas and Cr-bearing borides and carbides. Element maps collected by EPMA in Figure 3.5 show that there is a much higher volume fraction of Cr-rich particles in the Deloro 50 deposit. The variation in volume fractions of these regions through the thickness of each coating are shown in Figure 3.7 and Figure 3.8, which indicate the microstructures were nearly uniform through the thickness of the coating. The volume fraction of interdendritic phases (including the Cr borides and carbides) corresponds to about 35% in Deloro 30, versus about 55% in Deloro 50. The volume fraction of the Cr-rich particles increased from about 1.5 to 15vol% in Deloro 30 versus 50.

Figure 3.5 and Figure 3.8 show that a significantly higher volume fraction of Cr-bearing phases were produced in Deloro 50, and these were all situated within the interdendritic regions. From Figure 3.3(b) and Figure 3.5(b), three morphologies of Cr particles could be distinguished in the coating produced from Deloro 50, one consisting of a blocky equiaxed phase, another forming globular islands, and others taking on an acicular form with a rhombus shaped cross-section. Similar rhombus shaped Cr_7C_3 carbides were found in a NiCrBSi coating by Lebaili et al. as shown in Figure 3.6 [15].
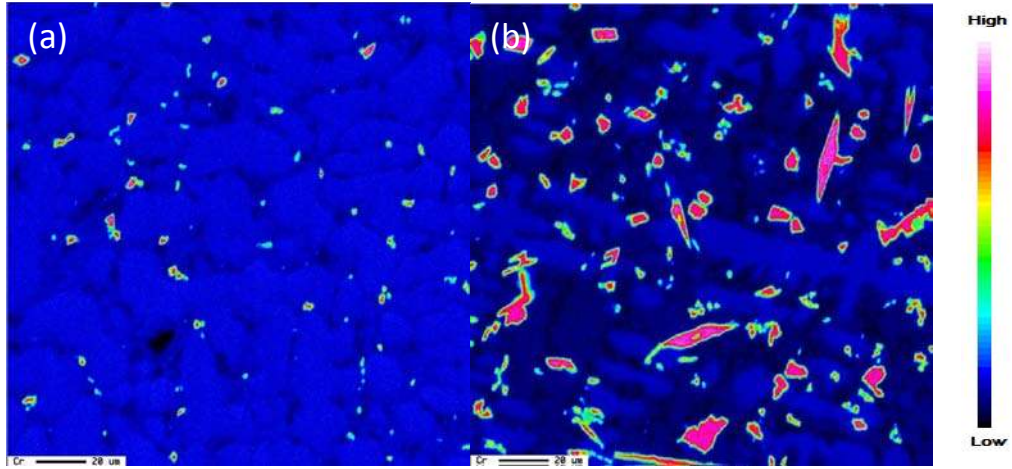
Figure 3.5. EPMA Cr element map for (a) Deloro 30, and (b) Deloro 50, both obtained from the mid-thickness region.
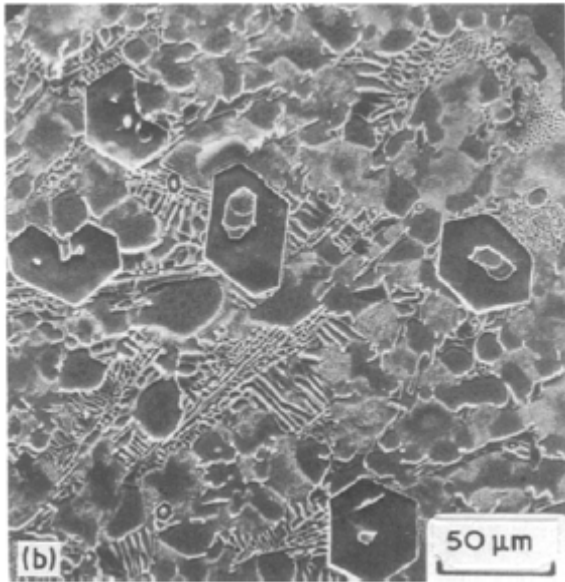
Figure 3.6. M_7C_3 carbide in an NiCrBSi alloy. [15]
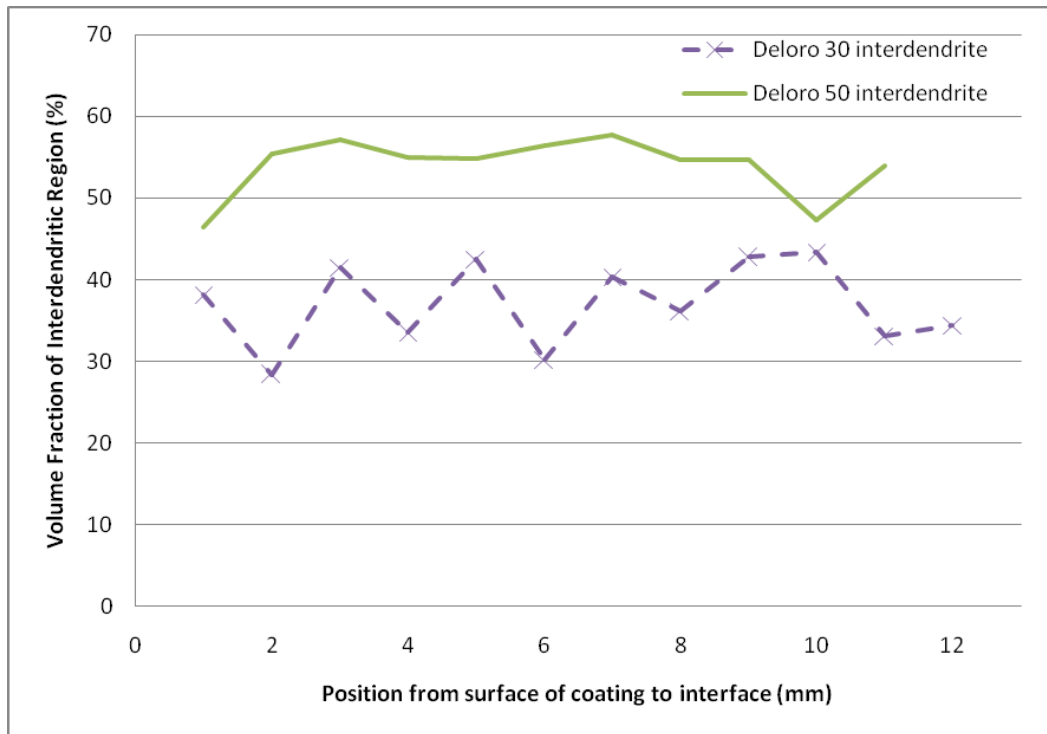
Figure 3.7. Volume fraction of interdendritic regions for Deloro 30 and 50.
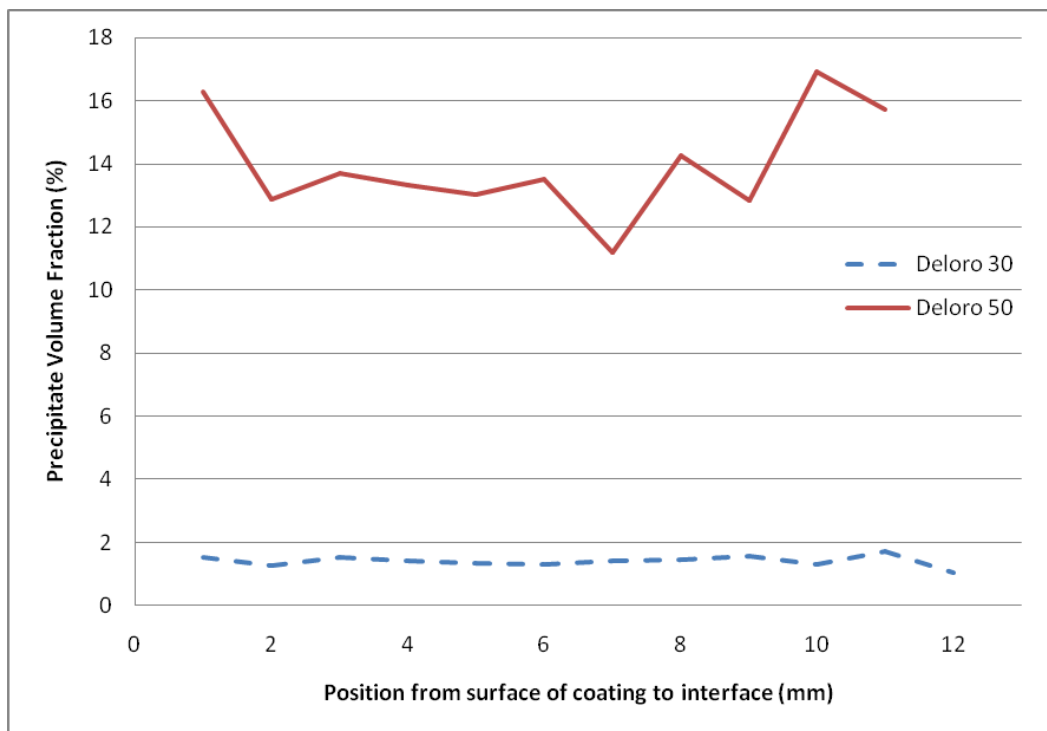
Figure 3.8. Overall volume fraction of Cr particles in Deloro 30 and 50.

EPMA maps of B, C, Cr, Fe, Ni, and Si were compared between the coatings. The maps of Si are shown in Figure 3.9 and indicate that Si segregated preferentially to interdendritic regions forming a globular structure in both alloys, shown in detail in Figure 3.4. The EPMA maps for other elements are shown in Figure 3.10 for Deloro 50. Boron also segregated preferentially to the interdendritic regions where it leads to the formation of chromium borides. Although the segregation of boron to interdendritic regions also occurred in Deloro 30, few chromium borides could be detected. Finally, carbon segregated to interdendritic regions in both alloys, which accommodated the formation of Cr-carbides. The element maps for boron and carbon in Figure 3.10 suggest that the globular regions are Cr-carbides (with a lower carbon ratio than the acicular rhombus-shaped carbides), and the equiaxed globular regions are Cr-borides. It is interesting to note that in both alloys, the iron was concentrated in the primary dendrites. EPMA of Colmonoy 4 and Colmonoy 6 revealed similar features to Deloro 50 (See Appendix C).
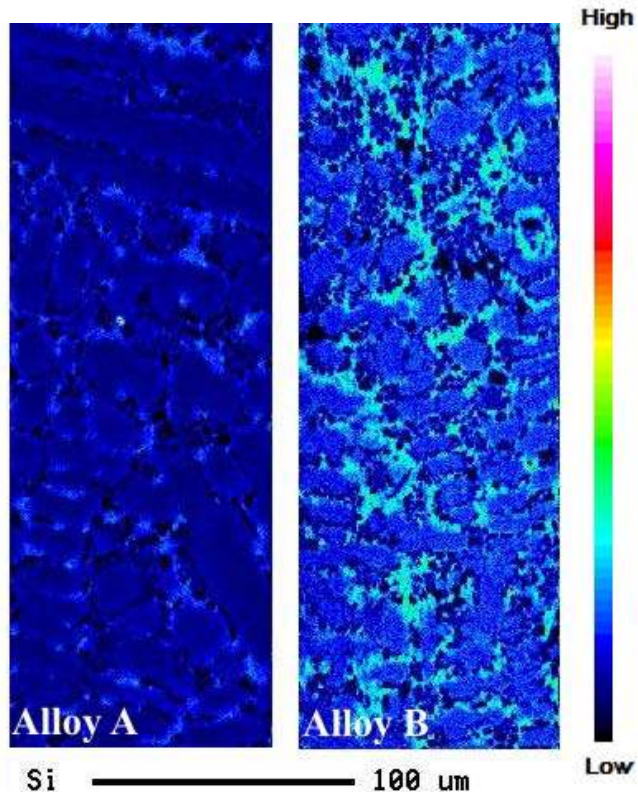
Figure 3.9. EPMA maps of Si in Deloro 30 and 50.
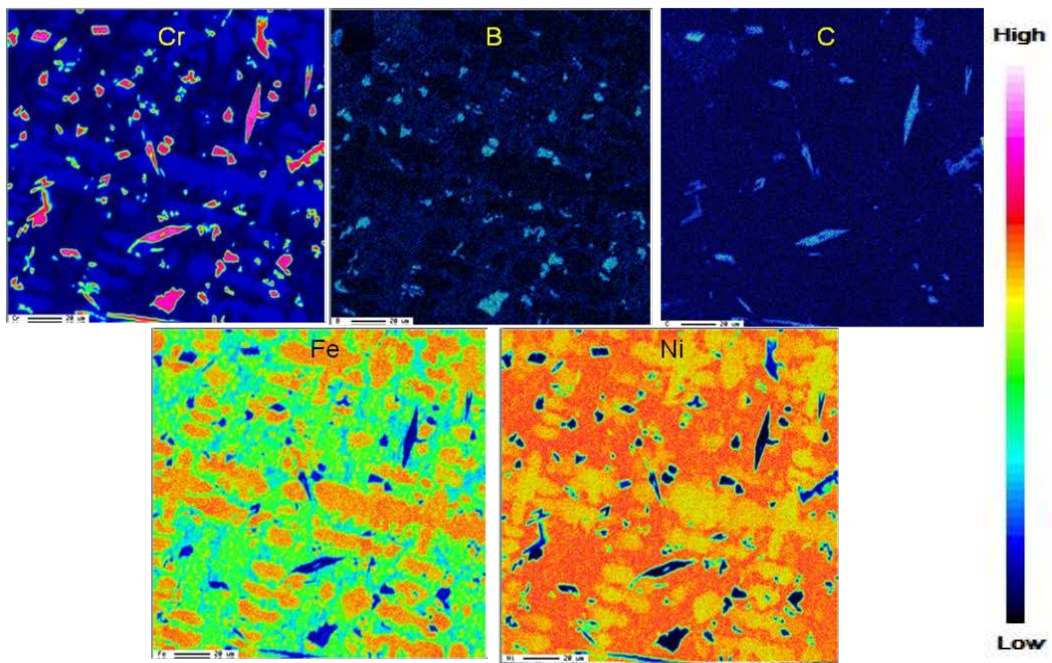
Figure 3.10. EPMA map of Cr, B, C, Fe and Ni regions in Deloro 50.

An EPMA line scan across three Cr bearing precipitates (located along the arrow in Figure 3.11) indicated that the rhombus-shaped precipitate was a chromium carbide and the two globular precipitates were chromium borides. This is consistent with the boron and carbon element maps showing globular or acicular Cr-carbides and nearly equiaxed Cr-borides in Figure 3.10.
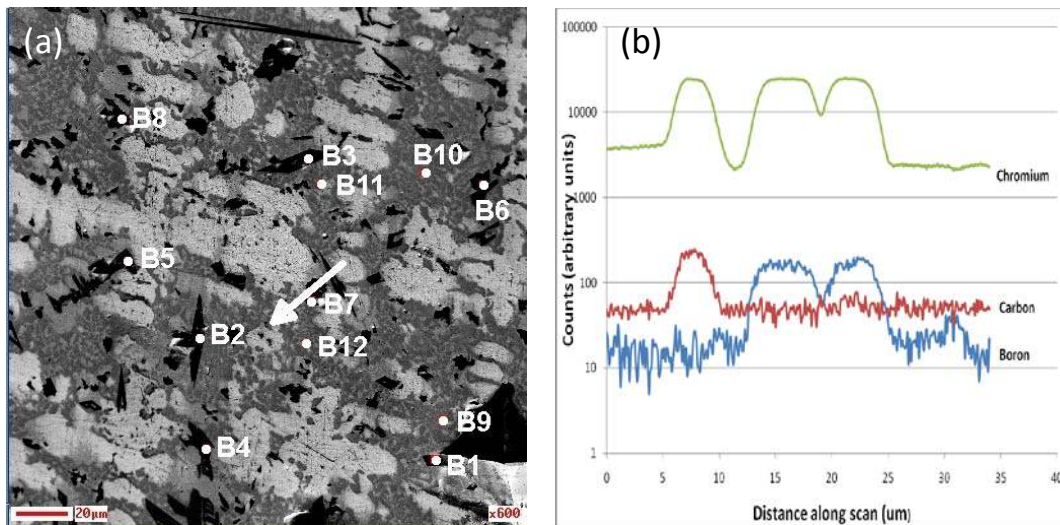
Figure 3.11. (a) Line scan across selected area highlighted by red arrow in Deloro 50. (b) WDX intensity measurements along the arrow indicated in (a).

AES was used to quantify the compositions of various phases present in the deposit. This technique is highly surface sensitive, and only probes the first 10 nm of the sample which avoids interaction volume effects of the electron beam. The AES results for various point analyses (points B1-B12 in Figure 3.11a) taken from Deloro 50 are shown in Table 3.2. The likely phases indicated by the AES results correlate well with previous data reported in the literature.

Table 3.2. AES results for Deloro 50.

	Atomic Percent						Probable
Point	C	Cr	B	Ni	Fe	Si	Phase
B1	44.8	54.9	0	0.3	0	0	Cr_3C_2
B2	44.6	54.7	0	0.2	0.6	0	Cr_3C_2
B3	45.2	54.8	0	0	0	0	Cr_3C_2
B4	33.9	54.9	2.7	5.7	2.8	0	Cr_7C_3
B5	38.2	54	1.9	4.6	1.3	0	Cr_7C_3
B6	0.5	54.3	45.2	0	0	0	CrB
B7	7.5	50	41.2	0.4	0.9	0	CrB
B8	0.2	52.5	47	0.3	0	0	CrB
B9	0	7.2	29.1	62.7	0	0.9	Ni_3B
B10	2.3	4.5	29.4	63.8	0	0	Ni_3B
B11	7.6	3.9	21.4	63.4	0	3.8	Ni_3B/Ni_3Si
B12	4.7	5.1	14.1	68	0	8	Ni_3B/Ni_3Si

EPMA and AES analysis was also performed on a 50HRc Cr-free alloy (Hoganas 1559-SP329) and revealed the microstructure shown in Figure 3.12. The large lighter phases are the Ni-rich primary dendrites which contain some carbon, and are separated by a fine $Ni-Ni_3B$ eutectic. Although this alloy does not contain any Cr-rich particles, it is still relatively hard due to the presence of many Ni_3B phases (confirmed with AES), which has a hardness of around 1000 HV [44].
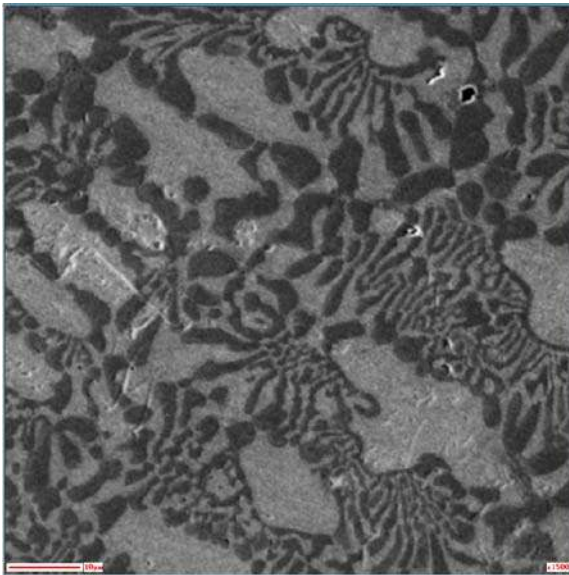
Figure 3.12. SEM image of the Cr-free alloy Hoganas 1559-SP329.

3.3. Microhardness and Wear Performance

The average hardness of the Deloro 50 deposit is about 600HV (approximately 55HRc) versus an average of 350HV (approximately 36HRc) for the Deloro 30 alloy (see Figure 3.13). Both of these values are slightly higher than the nominal hardness values based on the manufacturer datasheets (Table 2.1).
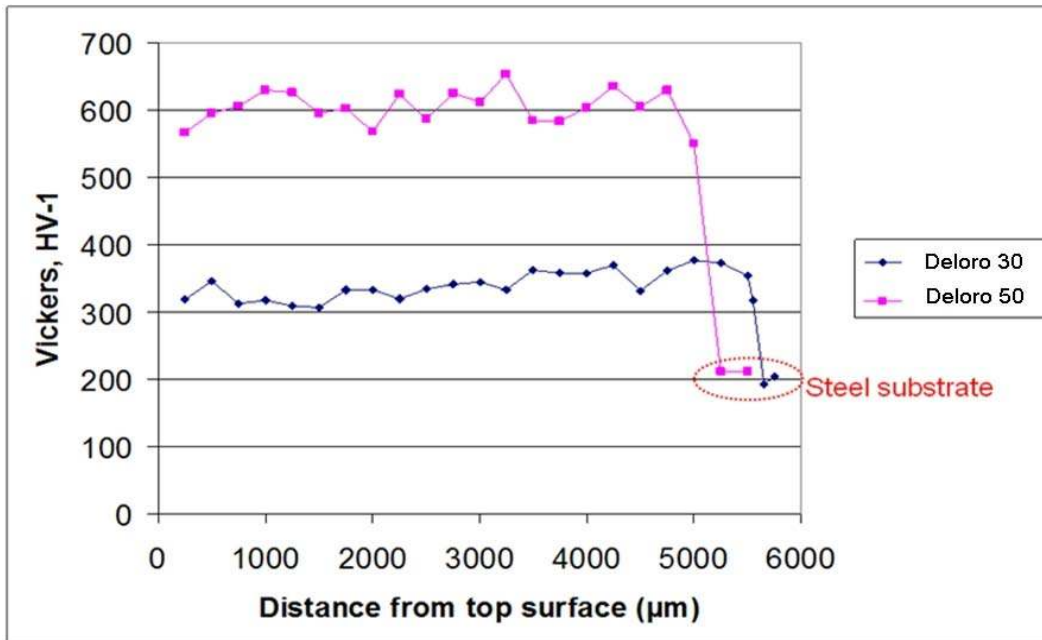
Figure 3.13. Hardness profiles in Deloro 30 and 50 through the coating thickness.

Microhardness measurements of individual phases were also obtained using a 25g indenter load, and these are visible in Figure 3.14. Several indents were made on the primary dendrite Ni-phases of Deloro 30, which had an average hardness of 264 HV. The interdendritic phase of Deloro 30 had an average hardness of 500 HV, however individual Cr-based particles in this coating were too small for reliable hardness measurements to be obtained. Measurements of individual phases in Deloro 50 (see Figure 3.14) reveal that the primary dendrite average hardness is about 405HV with an average hardness for interdendritic region of 860 HV. In the case of Cr-based precipitates the hardness values ranged from 973 to 1400 HV, with an average of about 1200 HV.

Applying a composite model to the analysis of the hardness results, the average Vickers hardness of the coating can be expressed as:

$$HV = \left(V_d \times HV_d\right) + \left(V_{id} \times HV_{id}\right) + \left(V_p \times HV_p\right) \qquad \text{Eq.1}$$

where V is the volume fraction, HV is the phase hardness (with subscripts "d", "id", and "p" representing dendritic, interdendritic, and Cr-particles, respectively) in the deposit. Based on the average measured values of the individual phases, the expected average hardness calculated from Eq. 1 is 348 HV for Deloro 30, and 748 HV for Deloro 50. These values are higher than the hardness values shown in Figure 3.13 when testing with a 1 kg load. It is possible that this calculated average based on microhardness measurements may produce errors since particles with dimensions < 25 µm were measured with microhardness testing, and this may result in hardness overestimations due to possible strengthening effects at the surrounding particle/matrix interfaces. In addition, the thickness of softer phases may be less than the plastically deformed region produced during indentation and thus lead to overestimated predictions using Eq. 1. However, this composite model appears to give a reasonable prediction of the average hardness based on the volume fractions of the various phases. In terms of wear resistance, there was a good correlation between interdendritic phase fraction and wear rate as shown in Figure 3.15 with higher interdendritic fraction leading to a lower wear rate.
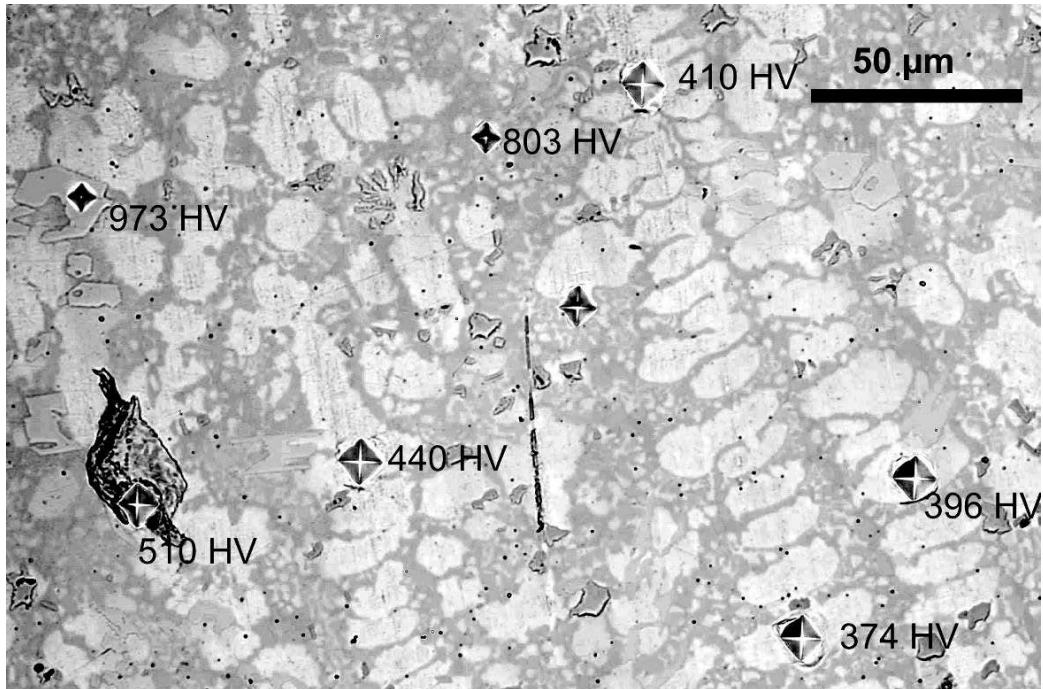
Figure 3.14. Microhardness measurements of selected area in Deloro 50.
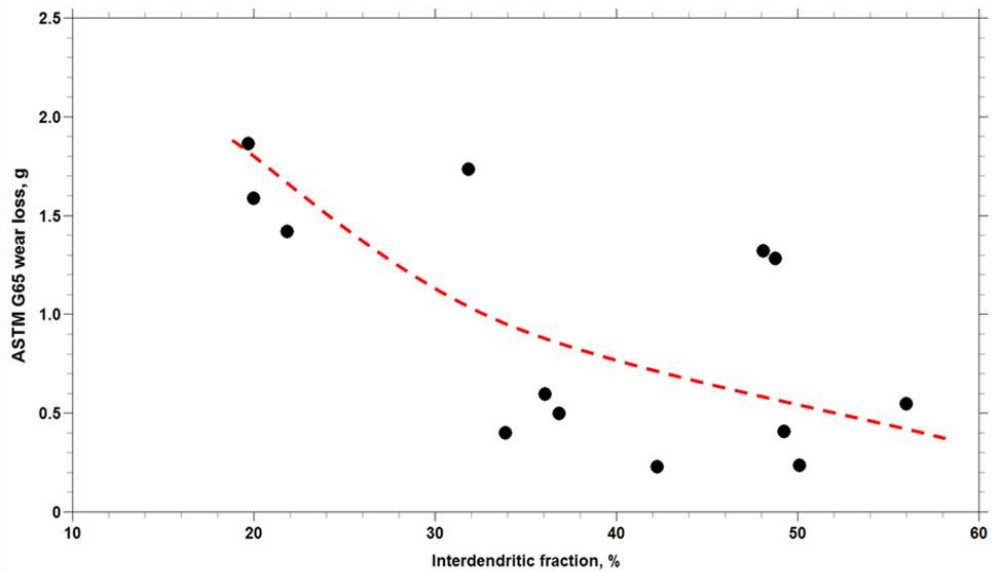
Figure 3.15. Interdendritic fraction vs. wear rate.

4. Discussion of Ni-alloy results

4.1. Microstructural Constituents

The microstructures of the deposits for both alloys were nearly uniform through their thickness. This is in contrast to earlier findings regarding NiCrBSi PTAW deposits on stainless steel [5] which indicated 3 distinct regions with different microstructures and hardness values. The present EPMA results indicate nearly uniform microstructures and macrohardness values throughout the deposit, and it is likely that lower base material dilution accounts for the through-thickness uniformity. Deloro 50 showed the higher interdendritic and particle volume fractions because there is more carbon and boron, which segregate to the interdendritic areas (since their solubility in Ni is negligible) and lead to the formation of hard phases such as carbides and borides. Optical and SEM imaging indicated that during PTAW of a NiCrBSi alloy, Cr borides formed first, followed by Ni solid solution simultaneously with the growth of Cr carbides, and the remaining liquid forming a $Ni-Ni_3B$ eutectic [18].

EPMA element maps and line scans of both alloys showed that silicon and boron segregated to the interdendritic regions and may be forming $\gamma Ni-Ni_3Si$ eutectic, along with Ni_3B, however previous work using a high power laser diode also indicated the presence of Ni_3Fe [39]. In that case during laser cladding operations a much thinner coating is produced which drastically reduces the diffusion distance required for iron from the substrate into the coating. One may expect that iron diffusion and Ni_3Fe formation should be limited to within the first 0.5 mm of the coating interface based on the previous results.

AES results in Table 3.2 indicate the presence of Cr_3C_2 (points B1-B3), Cr_7C_3 (points B4 and B5), CrB (points B6-B8), and Ni_3B phases (points B9-B12) in the interdendritic regions, see Figure 3.11(a). These results are consistent with previous work, however Cr_2B has also been reported in other studies [5]. The AES quantifications also indicated that in terms of carbide particle shape, the rhombus-shaped carbides were most likely Cr_3C_2 and the irregular shaped carbides are Cr_7C_3 particles.

The wear resistance of NiCrBSi coatings is largely attributed to the formation of hard boride and carbide particles [5]. For example, the hardness of Cr_2B particles is about 1250 HV [50] and 1400 HV and 1700 HV for Cr_3C_2 and Cr_7C_3, respectively [64]. However, in the present work, AES analysis suggests that approximately half of the Cr-based particles are CrB. The formation of CrB may actually be preferred in terms of optimizing coating performance since it has a hardness of 2300 HV[65].

From the EPMA carbon element map of Deloro 50 (see Figure 3.5(b)), it can be seen that there are carbides with differing carbon counts which is likely due to different chromium carbide phases.

4.2. Element Segregation

Since the solubility of C, B and Si is very low in the γ-Ni phase, the addition of these elements leads to their segregation towards the interdendritic regions as shown in Figure 3.4 and Figure 3.9. The segregation of Cr has seldom been considered in the NiCrBSi system, yet this is an important element since the formation of Cr-borides and carbides is controlled by the Cr concentration at the interdendritic regions where the C and B are concentrated. Although there is only a slight increase in the Cr content from Deloro 30 to Deloro 50, there is a substantial increase in the amount of Cr-bearing phases produced. The influence of alloy composition on elemental segregation can be understood from the viewpoint of solidification theory and the Scheil equation which states that the composition of the solid at the solid/liquid interface is [66]:

$$C_s^* = kC_o[1 - f_s]^{k-1} \qquad \text{Eq.2}$$

where C_o is the nominal composition of the alloy, f_s is the fraction of solid, and k is referred to as the segregation coefficient which corresponds with the ratio C_s/C_l between the composition of the solid and the composition of the liquid. In the case of the partitioning of elements, values of k<1 indicate low solubility for the

element and rejection of it away from the dentrite core, and values of $k>1$ indicate high solubility within the dendrite. It has been shown that the application of the Scheil equation is valid during arc welding processes, since there is negligible diffusion in the solid, perfect mixing in the liquid, and undercooling is not significant [67].

Since the start of solidification occurs when f_s is zero, Dupont et. al showed that composition data obtained by EDX point analysis for the cores of dendrites can be used to quantify segregation via the Scheil equation [67]. In this case, the EDX quantification was averaged from at least 5 dendrites to yield values for C_s, and this is compared to the average composition of the deposits C_o, obtained by inductively coupled plasma (ICP) analysis shown in Table 2. The table shows the segregation coefficient value k (where lower values suggest more segregation away from the dendrite core) for the elements in both alloys. Comparing the segregation coefficient values in both Deloro 30 and 50, it can be seen that there is a tendency for the Cr to segregate slightly towards the dendrite in both alloys. This situation is not desirable from the perspective of optimizing wear performance, since hardness and wear resistance improves with the formation of Cr-borides and Cr-carbides. Considering that EPMA maps for Deloro 50 indicate that a considerable amount of boron is concentrated in the interdendritic regions (see Figure 3.10), any alloy additions which could promote the segregation of Cr away from the γ-Ni (rather than toward the dendrite) are desirable. The values for carbon and boron have been neglected in the analysis in Table 4 since quantification of each of these elements at values of <1% by SEM methods are not feasible. However this does not have a significant effect on the other k values presented in Table 4, as the combined fraction of C, and B is < 2.4wt% in both alloys.

An examination of the ternary phase diagrams for both the Ni-Cr-Fe and Ni-Cr-Si systems reveals that addition of both Fe and Si will reduce the solubility of Cr in the γNi phase, and hence promote Cr segregation to the interdendritic area. However, since the increase of Fe was from 2.70 to 4.49 wt% in Deloro 30 versus Deloro 50, the relative change in the Cr solubility was not significant

enough to promote Cr segregation to interdendritic regions. The fraction of Si did not significantly change in the two alloys, and the Si itself had a strong tendency to segregate away from the dendrites. This would suggest a much greater increase in Si would be required to promote Cr segregation compared to additions of iron. Since the iron itself preferentially segregates to the γ-Ni dendrites, it has a greater potential to change the Cr solubility in the solidifying dendrite [43]. This could promote segregation of Cr to the boron-rich interdendritic regions, and enhance the rate of Cr-boride formation. In the case of the two alloys studied, the contribution of additional Fe to segregation of Cr only had a minor influence within the composition range examined.

Table 4.1. Segregation coefficient "k" for elements in overlay deposits.

Deloro 30				Deloro 50			
Element (wt%)	Deposit chemistry, C_o	Dendrite core	k	Element (wt%)	Deposit chemistry, C_o	Dendrite core	k
Ni:	Bal	Bal	-	Ni:	Bal.	81.21	-
Fe:	2.70	3.09	**1.14**	Fe:	4.49	5.59	**1.24**
B:	1.25	-	**-**	B:	1.98	-	**-**
C:	0.11	-	**-**	C:	0.42	-	**-**
Cr:	8.63	9.62	**1.11**	Cr:	9.28	10.71	**1.15**
Si:	3.14	1.8	**0.57**	Si:	3.94	2.48	**0.63**

4.3. Factors Influencing Hardness

The average hardness calculated from Eq. 1 is higher than the average hardness shown in Figure 3.13. This is likely to be higher due the small size of the regions which are probed during indentation. For example, since the size of the plastic zone may approach or exceed the dimensions of the soft dendritic regions, the apparent hardness of dendrites may be higher than the actual value since these phases are surrounded by a significantly harder interdendritic region.

Also, the plastic zone may encounter interphase boundaries which would provide a hardening effect. Although these considerations regarding the plastic interaction volume should be taken into account, it is clear that the Si-rich interdendritic regions provide a major contribution to the hardness, particularly in Deloro 50 the since formation of Ni_3Si is likely and has a relatively high hardness of 600+ HV [68].

The role of B and Si in the alloy chemistry has traditionally been recognized as a melting point suppressant [3]. In the case of Si, this is accomplished by the formation of a $\gamma Ni-Ni_3Si$ eutectic with a melting point expected at 1143ºC based on the binary phase diagram [43]. Since Figure 3.4 indicates that these phases are primarily formed in the interdendritic regions during terminal solidification, the addition of Si will increase their volume fraction and the overall hardness of the alloy. This effect is enhanced by the fact that Si also segregates away from the γ-Ni dendrites during the initial stages of solidification.

The present work has shown that B and Si both segregate to interdendritic regions, see Figure 3.9 and Figure 3.10. Due to the very limited solubility of boron in Ni, it is likely to have a dominant role in determining the volume fraction of the interdendritic region. For example, the boron content increases from 1.25 to 1.98wt% in Deloro 30 vs. Deloro 50. One may expect Deloro 50 to contain both a higher interdendritic and Cr-particle volume fraction since there is more boron and carbon which segregate to the interdendritic areas and form the hard phases such as Cr-carbides, and borides. Although the formation of hard CrB phases primarily occurs in the interdendritic regions, this may have been inhibited by the formation of $\gamma Ni-Ni_3B$ eutectic during terminal solidification. Following the solidification, the nucleation and growth of CrB is much slower due to the low diffusion rate in the solid state.

4.4. Matrix Conclusions

All of the NiCrBSi alloys examined had similar microstructures consisting of γ-Ni dendrites, with interdendritic material comprised of varying fractions of Ni-Ni$_3$B and Ni-Ni$_3$Si eutectics along with Cr-based borides and carbides. In the case of the two alloys studied in detail, Deloro 30 was found to consist of a 61.6vol% fraction of γ-Ni dendrites and a 1.4vol% fraction of Cr-rich particles, while Deloro 50 contained a 32.1vol% fraction of γ-Ni dendrites and interdendritic regions containing approximately 14vol% fraction of Cr-rich particles and Ni- borides and silicides. Other alloys examined by optical and electron microscopy yielded similar results.

The hardness of a typical NiCrBSi alloy deposit is controlled not only by the amount of Cr-rich particles present but also by the volume fraction of the interdendritic eutectics, since these are made up of hard Ni$_3$B and Ni$_3$Si phases. The interdendritic phase was shown to exhibit high hardness of about 860HV relative to the primary dendritic phase which had a hardness of about 405 HV. Since the volume fraction of the interdendritic phases is higher for Deloro 50, it significantly contributes to the overall properties of the deposit.

Although there was only a minor increase in Cr, C, and B content in Deloro 50, this lead to a large increase in the amount of Cr-particles from 1.5 to about 15vol% between the two alloys examined. Ternary phase diagrams suggest the addition of Fe or Si will decrease the solubility of Cr in Ni, however no significant change in Cr segregation was observed in the alloy compositions examined. It was also found that boron segregates to the interdendritic regions in both alloys and promotes formation of Ni$_3$B, though this may form at the expense of the harder CrB phase.

5. Ni-WC Composite Results

5.1. Microstructure of Ni-WC Composite Overlays

Two major issues in achieving optimal performance of the Ni-WC composite overlays, involve the non-uniform distribution and possible degradation or dissolution of the WC particles. Deposition of the Ni-WC MMC overlays produced microstructures as shown in the cross-section in Figure 5.1. The deposits were about 25 to 30mm wide and about 4 to 6mm in thickness. Almost all alloys showed a layer devoid of WC at the top of the deposit (shown in Figure 5.1 and higher magnification in Figure 5.2)) as well as a higher density of WC particles at the sides of the weave weld. The inhomogeneity of the WC particles has been accounted for mostly by settling during the brief time that the overlay is fully molten [69]. Some Ni-WC overlays also showed a similar barren layer at the bottom of the deposit, and the deposit produced using Deloro 50 alloy also contained round denuded zones in the middle of the deposit as indicated by the arrows in Figure 5.3. AES analysis of several MMC overlays showed that nearly all the phases present in the Ni-alloy overlays were also present in the metal matrix of the Ni-WC composite overlay. AES analysis detected γ-Ni, Ni_3B, and Cr-borides and Cr-carbides but Ni_3Si was not detected.
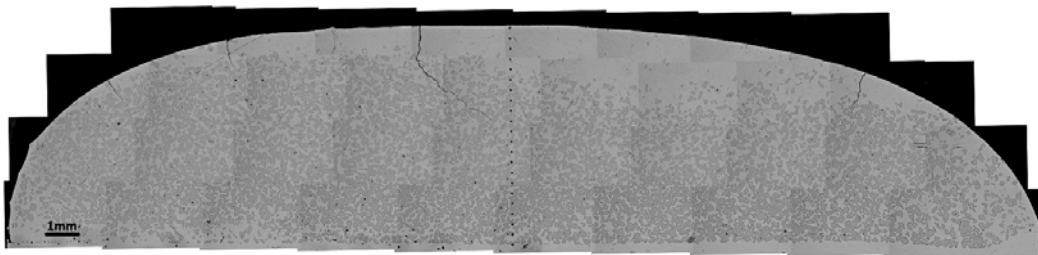
Figure 5.1. Ni-WC deposit optical micrograph of Colmonoy 5.
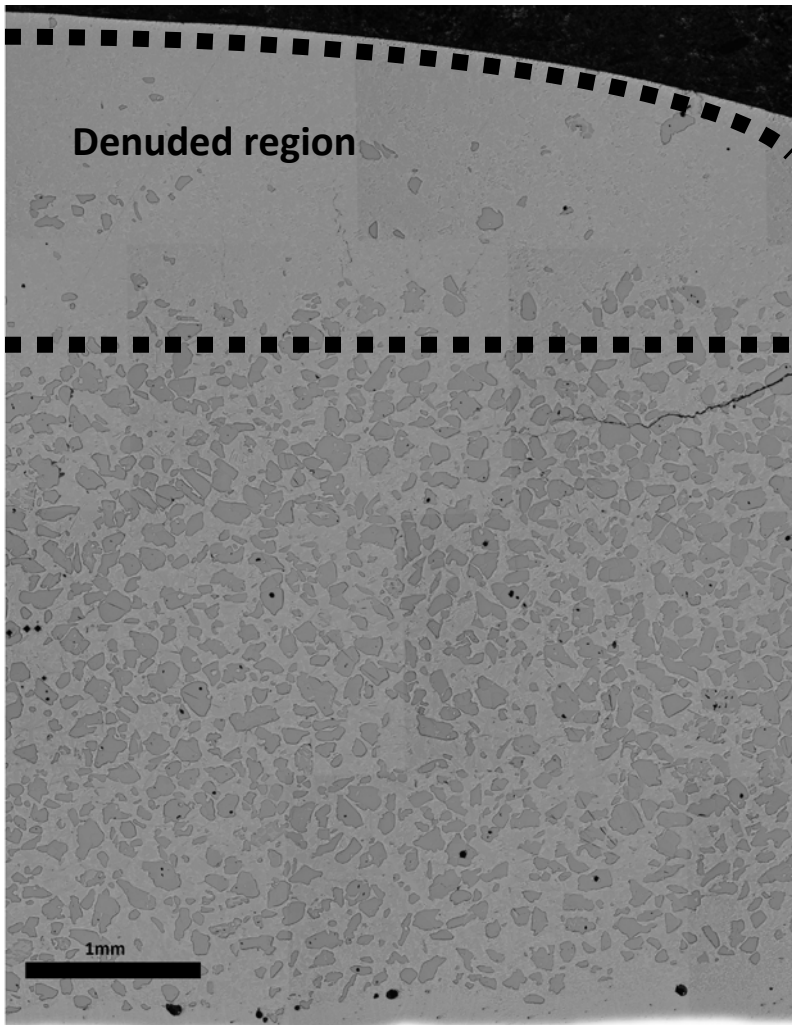
Figure 5.2. Optical image composition of section of Colmonoy 6 composite alloy.
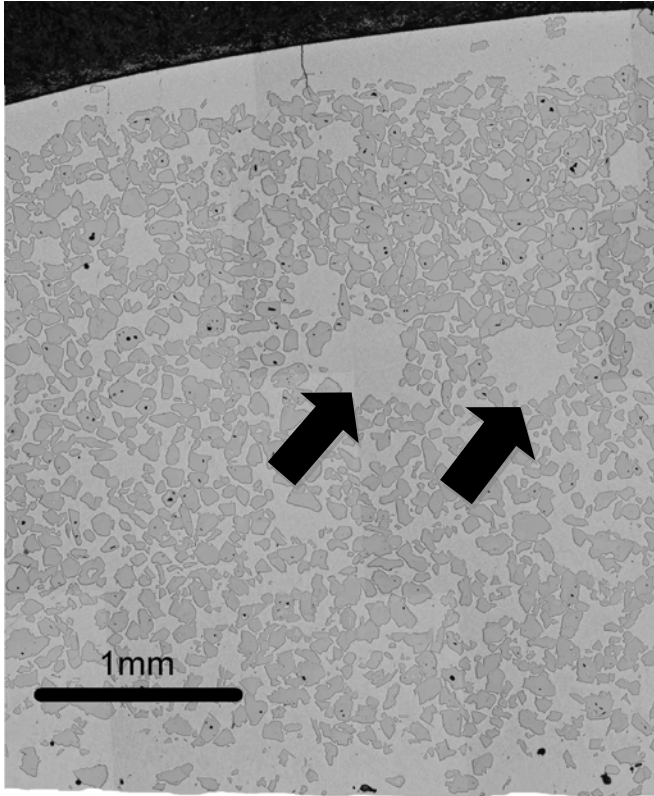
Figure 5.3. Circular denuded zones (indicated by arrows) in the Ni-WC overlay utilizing Deloro 50 matrix alloy.

Vickers microhardness testing was performed on the MMC overlays with a 1kg load at 250 μm intervals from the bottom (at the substrate/deposit interface) to the top of the deposit and compared to the hardness of the matrix alloy alone without WC particles. The average Vickers hardness through the thickness of the deposit centerline is compared in Figure 5.4. Although wide variation could be observed in the amount and distribution of the WC particles between all of the deposits examined, the hardness values increased roughly in proportion to the nominal hardness of the Ni-alloy for both the matrix and MMC overlays..
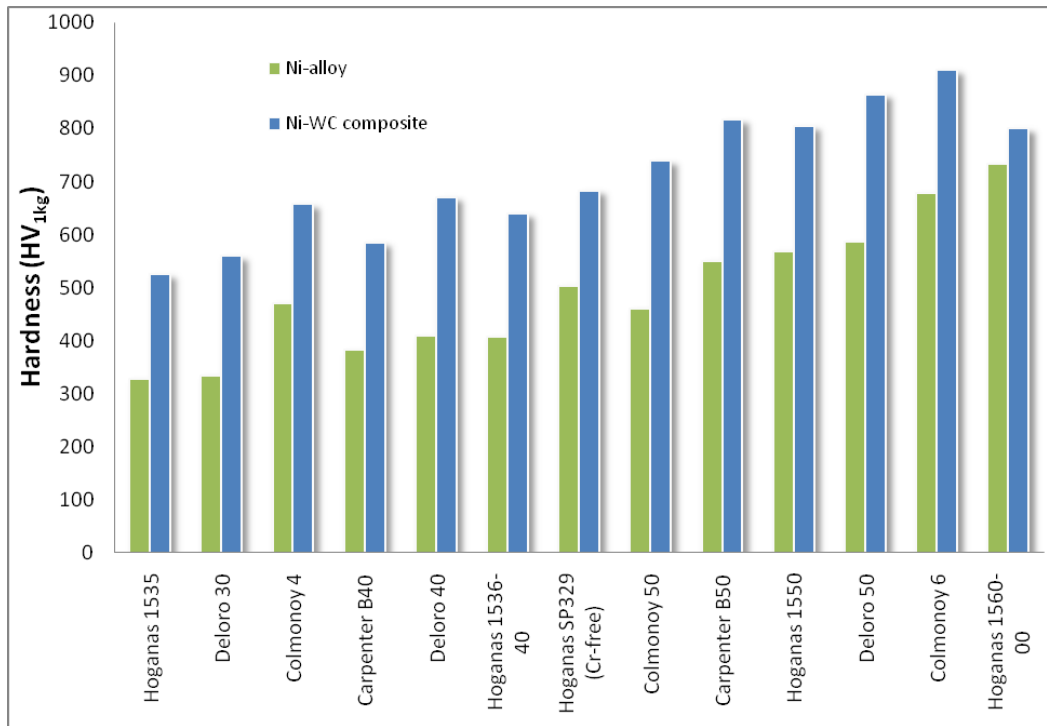
Figure 5.4. Average hardness values of the Ni-alloy matrix and Ni-WC composite overlays.

5.2. WC Dissolution

Optical image analysis of the composite alloys (example analysis sections of low and high WC dissolution alloys shown in Figure 5.5a and Figure 5.5b, Hoganas 1559-SP329 and Colmonoy 6, respectively) was used to estimate the dissolution of the WC particles. Based on a 60/40 wt% ratio between WC/Ni-alloy, the *volume* fraction of the deposit should theoretically be 45vol% WC-55vol% Ni (calculation shown in Appendix D) but 50vol% WC was used for the purpose of dissolution calculations as some error was expected since there is a minor difference in deposition efficiency in favor of WC. The highest dissolution was evident in alloys that had higher amounts (>8wt%) of Cr and alloying elements. Most notably, the Ni-WC overlays produced using Colmonoy 4 and Colmonoy 6 alloys exhibited the highest WC dissolution levels at about 40% (meaning that 40% of the initial WC material dissolved) and had high levels of Cr and C. Figure 5.6 also shows there is an increasing trend of dissolution relative to the carbon content (negative dissolution in Figure 5.6 due to variation in WC

quantified in Figure 5.8 coupled with 50vol% WC assumtion). However, no direct correlation could be determined between dissolution and specific alloying additions, since both the Cr and carbon content of each alloy increased in roughly equal proportion for all of the alloys examined.
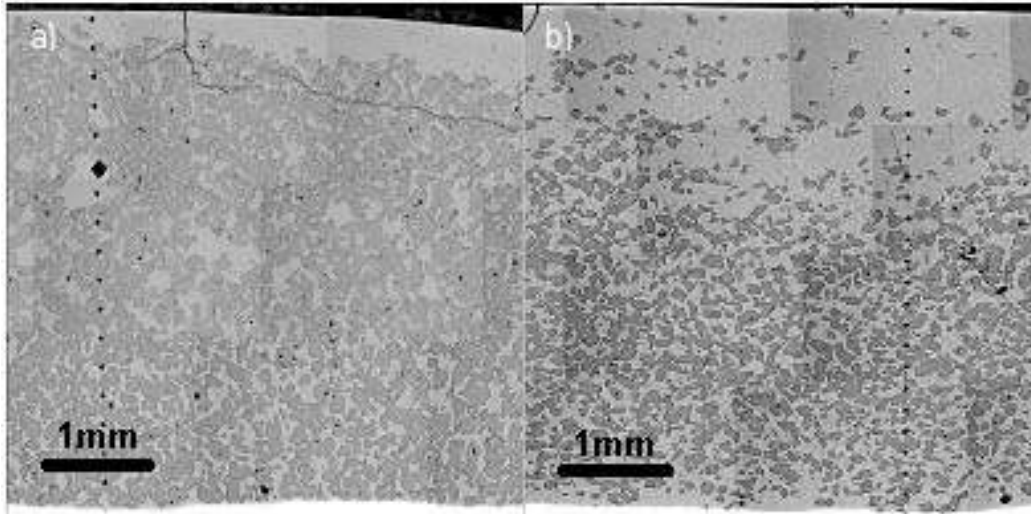
Figure 5.5. MMC cross-sections illustrating examples of (a) low dissolution of WC when using Hoganas 1559-SP329 Ni-alloy in the matrix, and (b) high WC dissolution when using Colmonoy 6 as the matrix.
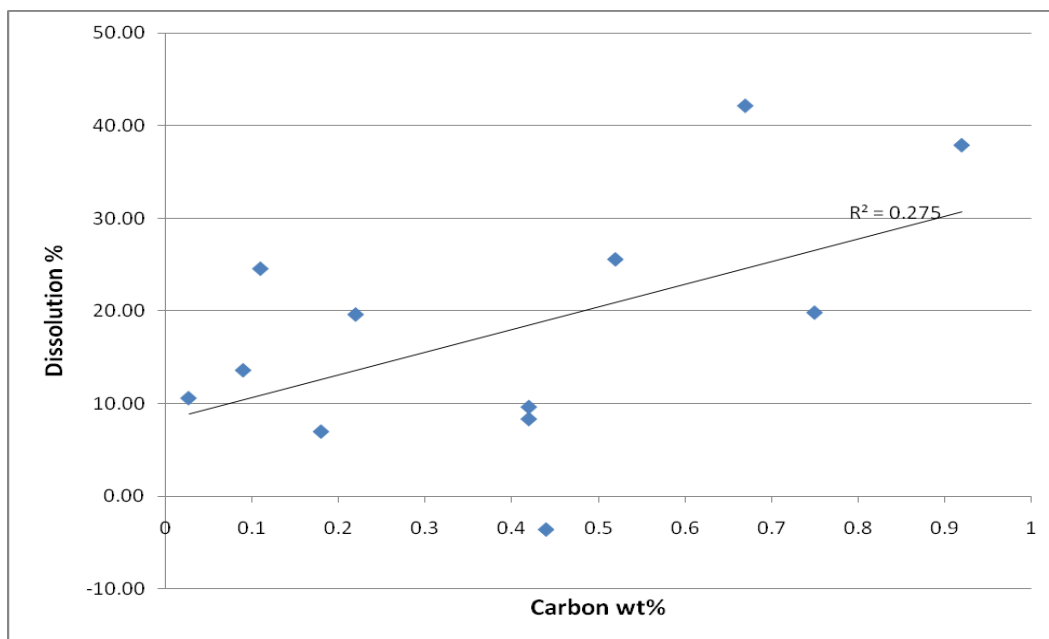
Figure 5.6. WC dissolution vs. carbon content of the matrix in the Ni-WC overlays.

Cross-sections were examined from the middle of the deposit to ensure consistency and to lessen any microstructural differences due to starting and ending the weave weld. The total WC fractions measured for each Ni-WC overlay are compared in Figure 5.7, calculated from cross-sections observed at the middle of each deposit. However, it should be noted that along the length, some heating of the substrate will occur during preparation of the sample due to the slow travel speeds used. To quantify any scatter in the dissolution rate along the deposit length, sections were made at the start, middle, and end of three different MMC deposits and the volume fractions were compared in each. The results of these quantification are shown in Figure 5.8. It was found that the difference in WC fraction calculation varied by 2 to 8% from the start to the end of the deposit. This suggests there was relatively little variation in the WC dissolution along the length of the deposit which could stem from the accumulation of heat in the substrate coupon during welding.
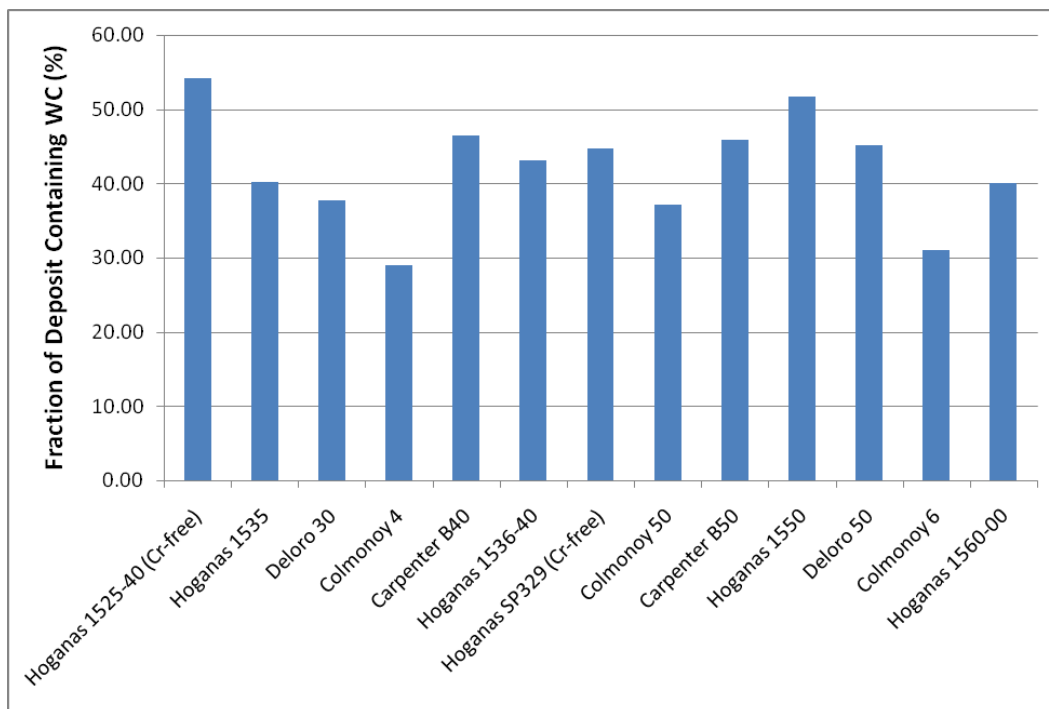
Figure 5.7. Total WC fraction in Ni-WC overlays.
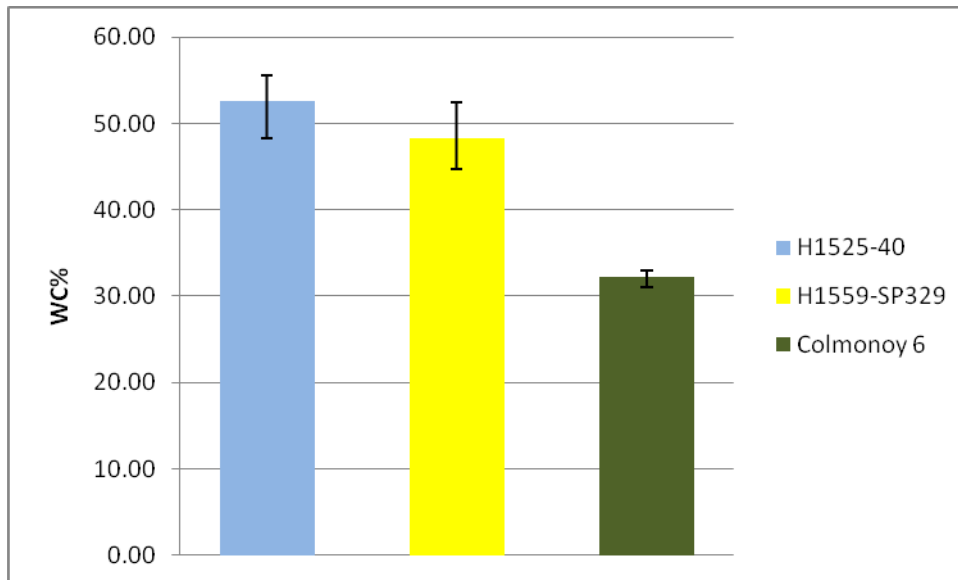
Figure 5.8. Average WC% with error bars indicating minimum and maximum of calculated values.

EPMA analysis revealed dissolution of primary WC carbides occurs and leads to the formation of secondary carbides surrounding the WC particles. The Hoganas 1559-SP329 Cr-free alloy tested showed little dissolution with only some secondary phases showing slightly higher tungsten concentration (Figure 5.9). The Cr-free alloy had very low carbon content as well, and as such this resulted in little dissolution. A feathery Cr-W-C phase formed at the periphery surrounding the WC-particles in a Ni-WC overlay utilizing Deloro 50 alloy (Figure 5.10) and AES element quantification of the composite involving Colmonoy 4 alloy suggested that the stoichiometry of that phase being about $Cr_7W_3C_6$ (quantifications shown in Appendix C).
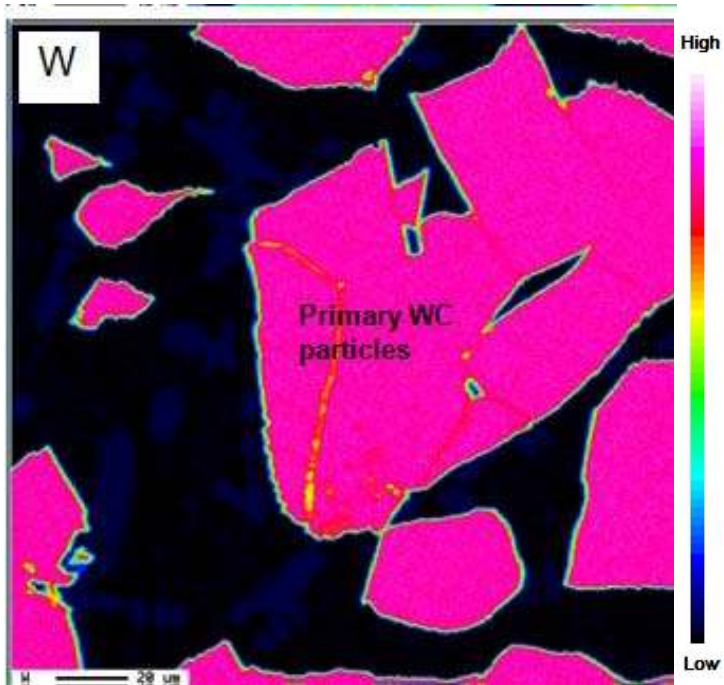
Figure 5.9. Tungsten EPMA element map of a Cr-free Ni-WC overlay (Hoganas 1559-SP329) with WC particles.
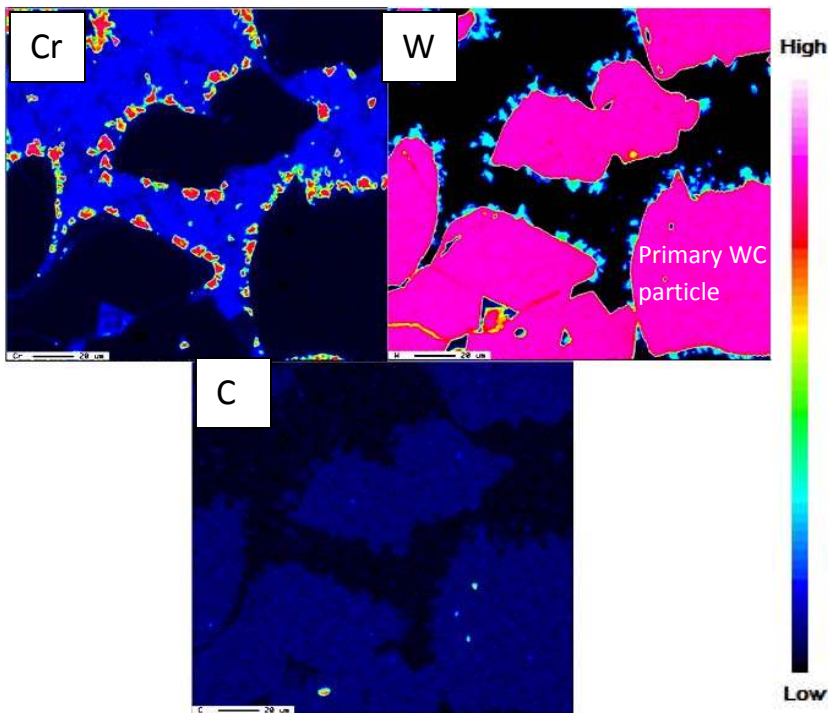
Figure 5.10. EPMA element maps for Cr, W, and C in a medium-Cr Ni-WC MMC overlay (Deloro 50) showing the Cr-W-C rich phases at the periphery of the WC particles.

The Ni-WC overlay produced using Colmonoy 6 alloy (which contained the highest fractions of Cr, C, and Si of all alloys tested) contained a blocky Cr-Ni-Si-W-C phases located between the WC particles (Figure 5.11). Repeated AES element quantification of points in Figure 5.12 revealed the stoichiometry of the blocky 5-component phase to be about $Ni_4Cr_5Si_2W_4C_{4.5}$ as indicated in Table 5.1, although there may be some error in the C quantification due to some preferential removal of lighter elements during ion sputtering of the surface prior to collecting the AES data.
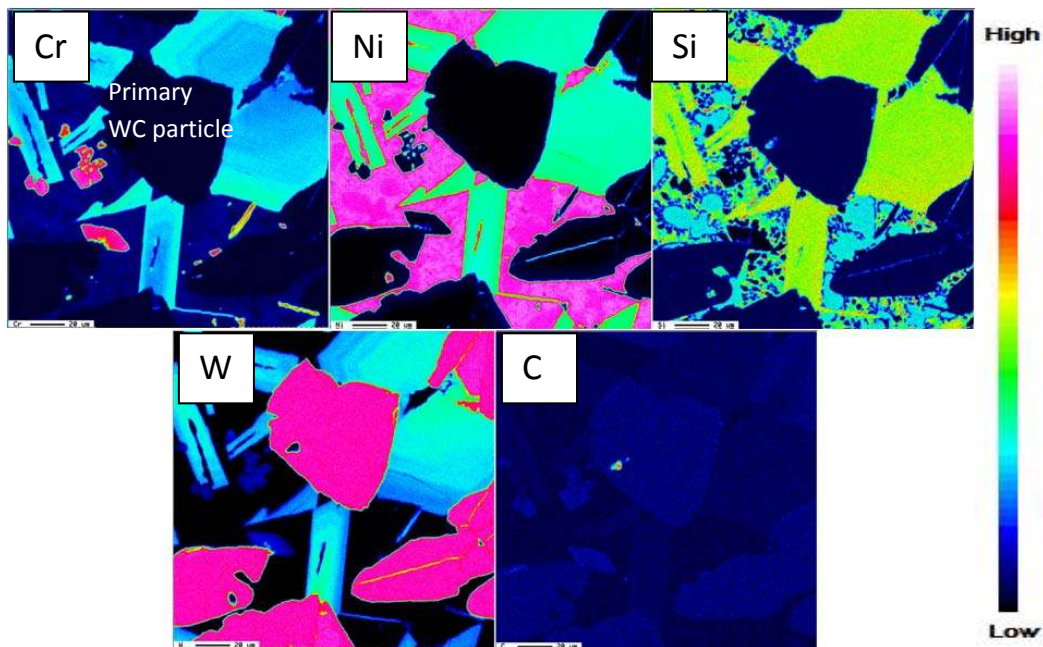
Figure 5.11 EPMA element map of the Ni-WC composite utilizing Colmonoy 6 alloy which contained the blocky Cr-Ni-Si-W-C phase.
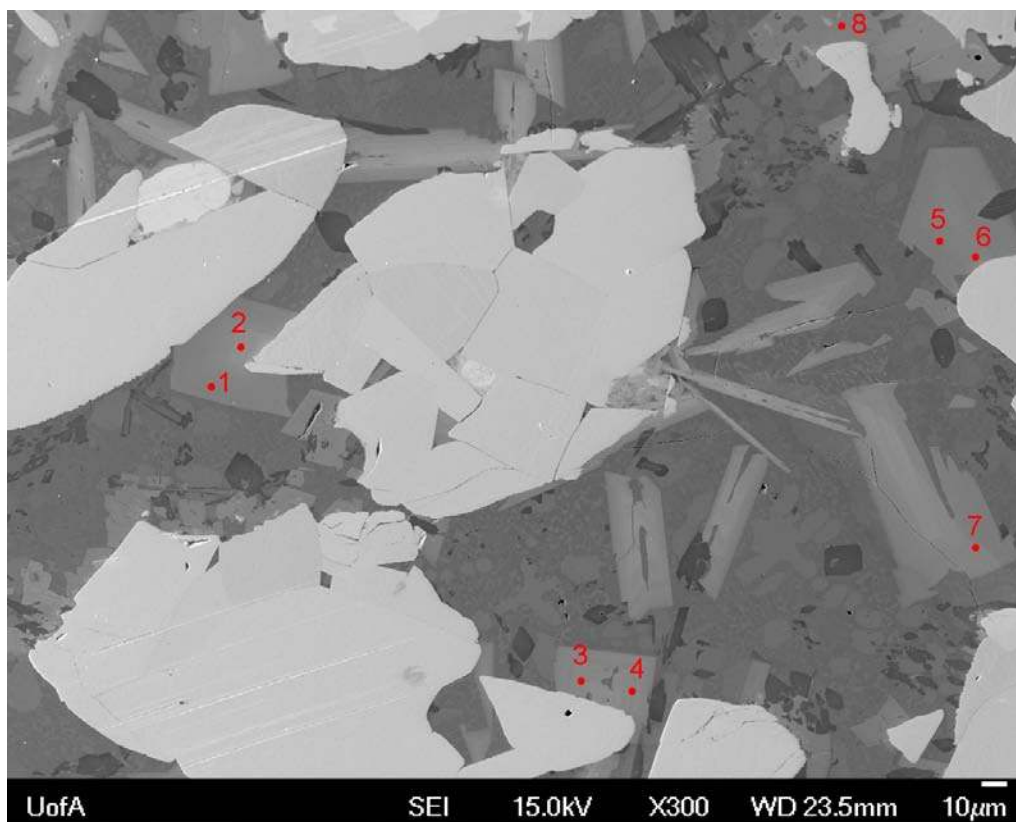
Figure 5.12. **SEM image of the Colmonoy 6 Ni-WC composite containing the secondary blocky phase involving Cr, Ni, SI, W, and C.**

Table 5.1. Repeated AES quantifications of the 5-component blocky phase between WC-particles in the Ni-WC composite produced using Colmonoy 6. (analysis points shown in Figure 5.12).

	Atomic Concentration (%)				
Point	**C**	**Cr**	**Ni**	**Si**	**W**
1	21.6	26.6	20.9	11	19.9
2	21.5	25.4	21.1	9.1	22.9
3	22.6	24.4	21	12	20
4	22.4	24.2	20.2	10.4	22.8
5	24.1	26.3	20.2	9.9	19.5
6	22.3	26.6	21.6	11	18.5
7	23.3	26.5	21.1	9.8	19.3
8	22	26.7	20.5	12.2	18.6
Average	**22.5**	**25.8**	**20.8**	**10.7**	**20.2**
Stoichiometry (est.)	**4.5**	**5**	**4**	**2**	**4**

Microhardness testing was performed on the MMC produced using Colmonoy 6 alloy to investigate the properties of the blocky 5-component phase and determine its contribution to the overall hardness of the composite. The hardness was found to vary between about 960 HV to about 1600 HV using either a 25 or 50g load, compared to about 2000 HV for the WC particles (see Figure 5.13). As a result, the blocky phase can make a significant contribution to the overall hardness when compared to the original matrix hardness of about 700 HV. However, microhardness testing on the blocky 5-component phase using loads higher than 50 g consistently resulted in cracking of the phase, suggesting these are particularly brittle. This will have drastic implications for the wear resistance of this Ni-WC overlay made using Colmonoy 6, as discussed in the following section.
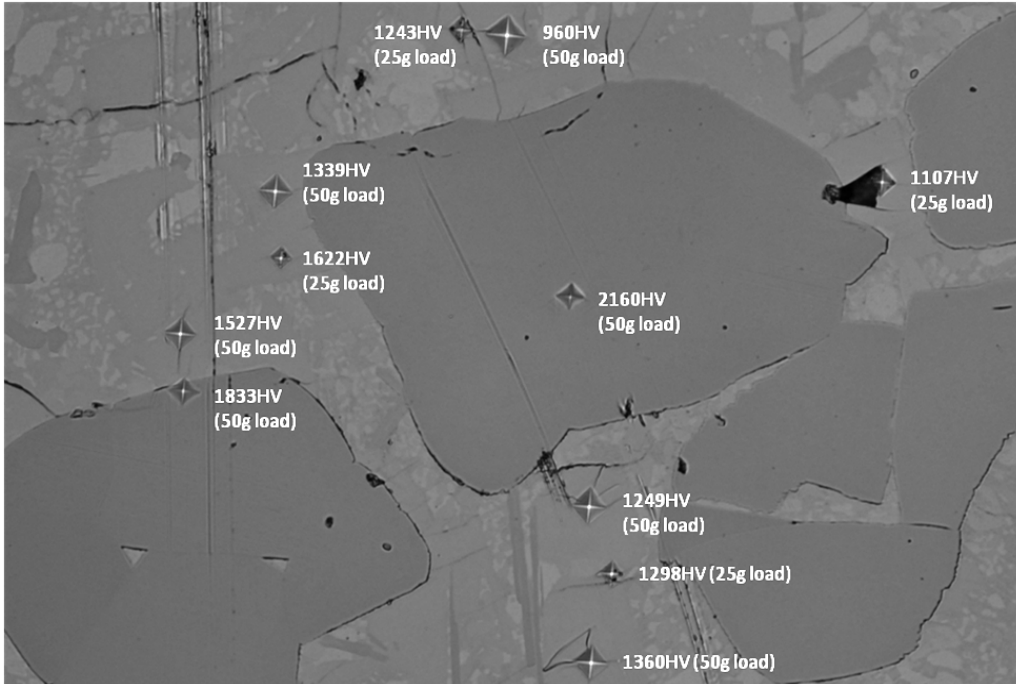
Figure 5.13. Microhardness indents on WC particles and Cr-Ni-Si-W-C blocky phase in the Ni-W composite utilizing Colmonoy 6.

5.3. Wear Testing Results

Wear testing as per the ASTM-G65 (dry sand rubber wheel test) on the matrix alloys (without reinforcing WC) indicated that wear resistance correlated almost directly with hardness for each of the Ni-alloys, and the values were roughly in proportion to the nominal hardness values indicated (Figure 5.14). The one anomaly was Colmonoy 4 alloy, and it was found that this alloy actually had a microstructure and measured hardness similar to the alloys with higher nominal hardness (ie. similar to the 50 HRc grades). In the case of the MMC wear performance, the matrix alloys that produced low hardness, such as those which were Cr-free actually yielded the best wear resistance (see Figure 5.15). The lowest wear rate was achieved by the Ni-WC coating utilizing Hoganas 1535 alloy, which achieved 0.041g mass loss (versus 1.585g for the matrix alone). It should be noted that the highest wear rate was for the Ni-WC coating utilizing Colmonoy 6 alloy which resulted in 0.098g mass loss, even though this alloy achieved the best performance of all the Ni-alloys with no WC particles.
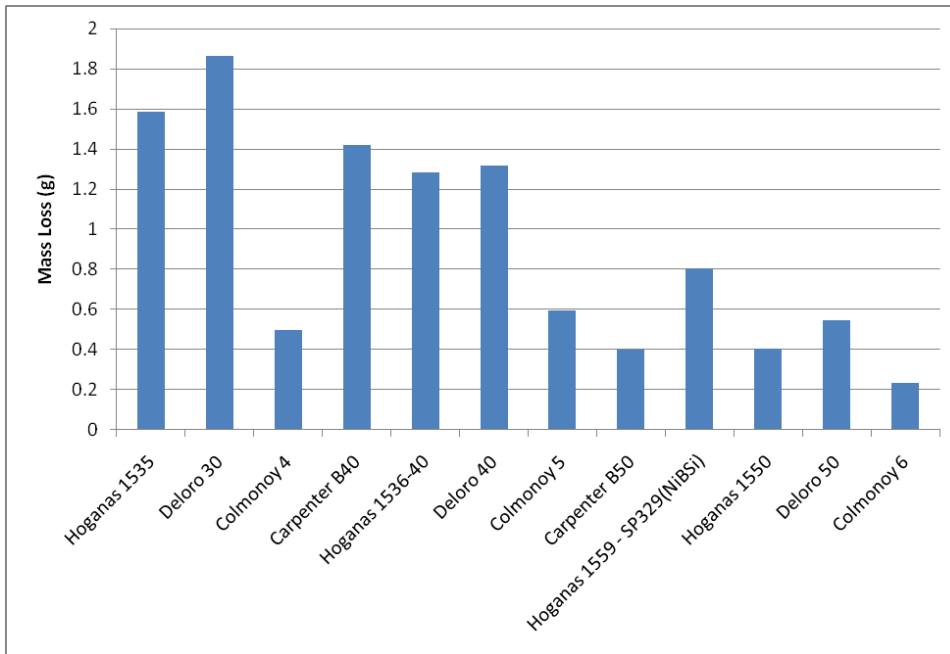
Figure 5.14. ASTM-G65 wear results for the Ni-alloys tested (wear results are for the 2nd wear scar).
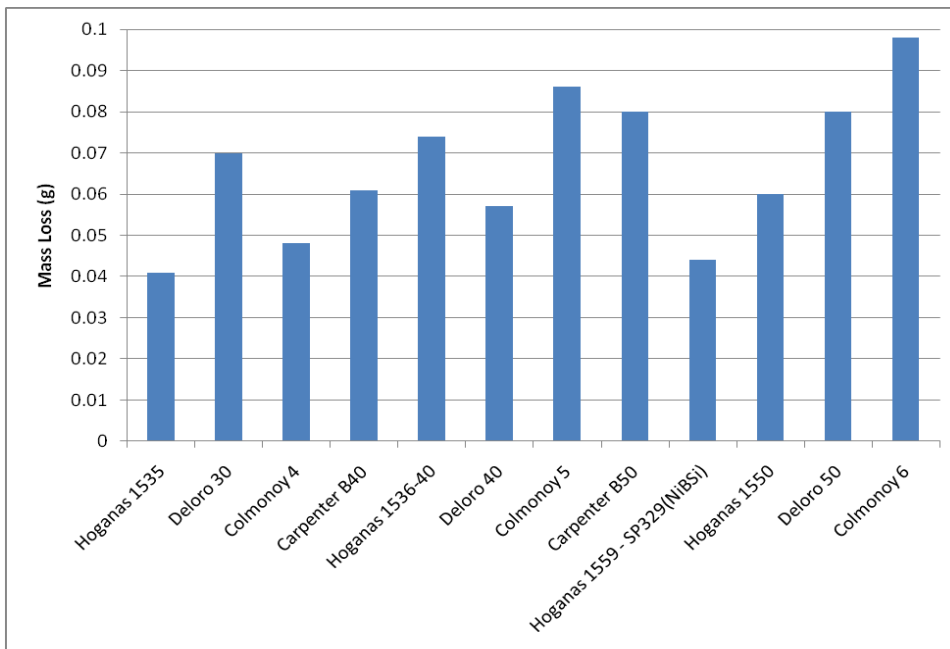
Figure 5.15. ASTM-G65 wear results for the Ni-WC overlays (wear results are for the 2nd wear scar).

The wear scars examined by SEM show that the WC particles are intact with the abrasive media, and protrude above the metal matrix. In the case of the Ni-WC utilizing Hoganas 1535 alloy (which exhibited the lowest wear rate), the surface of the WC particles are flat and smooth, with a short distance between adjacent WC particles (Figure 5.16a). In the case of the Ni-WC composite made using Colmonoy 6 alloy (which exhibited the highest wear rate), many of the WC particles appear to have a wider spacing (since the dissolution of the WC and their mean free path is higher), and seem to have fractured since they have a rough surface appearance (Figure 5.16b). This suggests that the WC may have likely chipped away, and the wider separation between WC particles would allow more of the matrix to be worn away. This accounts for the poor wear resistance observed in the Ni-WC based on the Colmonoy 6 alloy.
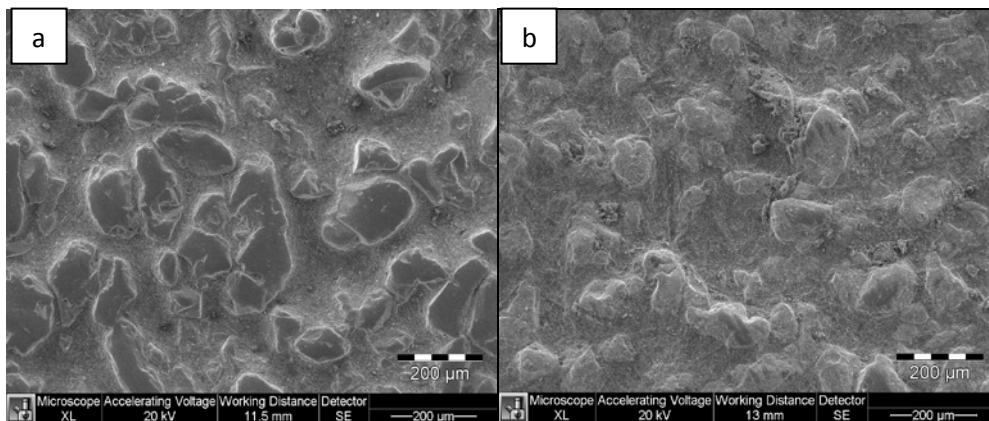
Figure 5.16. Wear scars for Ni-WC composites utilizing a)Hoganas 1535 and b)Colmonoy 6.

6. Discussion of Ni-WC Composite Results

6.1. Microstructure

Most MMC samples deposited by PTAW yielded a microstructure similar to that in Figure 5.1 which was devoid of pores, cracks, and denuded zones. Alloys with denuded zones or cracks were expected to perform poorly in wear testing (eg. Deloro 50 MMC had cracks and denuded zones and did in fact perform poorly in wear testing relative to the other MMCs).

As mentioned previously dissolution of the primary tungsten carbide particles was observed after PTAW welding and this resulted in the formation of secondary phases. The Cr-free alloy tested with EPMA contained very little secondary phases formed from dissolved WC and so its dissolution was very low (about 10% of initial WC dissolved). There did appear to be some phases that were slightly enriched in W that contained mainly Fe, and Si to a lesser extent. These phases containing Fe and Si were found in the Hoganas 1559-SP329 alloy deposit and so it appears they have a high affinity for dissolved tungsten in the composite alloys. The secondary phase contained Cr, W, and C in the case of a low-Cr alloy and formed at the periphery outlining the primary tungsten carbides and was quantified by AES to be about $Cr_7W_3C_6$. Based on the Cr-W-C ternary phase diagram, the intermetallic phases expected in this system are C_3Cr_6W, $C_4Cr_2W_3$, and possibly C_3Cr_5W.

In the case of a high-Cr alloy (Colmonoy 6) the secondary phases formed a large blocky phase and contained Cr, W, C, Ni, and Si. A W-Cr-Ni-Si phase was also detected in the case of Ni-WC overlay deposits made using gas metal arc welding, however, carbon may not have been detected in that study due to the use of EDX which is not sensitive enough to quantify C without significant error [69]. In addition, laser remelted NiCrBSi + WC alloy analyzed by EDS also revealed that some secondary phases had W, Ni, Cr, Si as well as possibly other elements that are not reliably detected by EDS [23]. Using AES however, this blocky secondary phase was quantified and it was found to have a stoichiometric formula of about $Ni_4Cr_5Si_2W_4C_{4.5}$. It should be noted that the phase, although appearing to grow out from the WC particles in certain micrographs, is more likely to have

grown from liquid phase in the melt between the WC particles. Based on the morphology and the gradients of chemistry across these particles, it appears these have grown as a single crystal. Evidence of this is visible in the EPMA map of W in Figure 5.11 where there appears to be segregation of elements outward from a central point which is away from the WC particle, and the gradient in W chemistry follows the angular geometry of the particle boundary. Similarly, fine dendrites in the matrix of a Ni-WC composite were attributed to the formation of numerous primary mixed carbides first in the molten melt which then provided heterogeneous sites for the nucleation of the γ-nickel phase [70].

6.2. Hardness

The average hardness of all alloys increased (by as much as a factor of two in the case of the low hardness Ni-alloys) due to the addition of WC reinforcing particles. However, when a 1kg load is used, the Vickers hardness reading may be influenced by whether the indent occurs on or near a WC particle. Several of the indents landed on WC particles and cracking of the particle was occasionally observed, leading to a lower hardness value than expected (~2000HV for a monocrystalline WC particle).

Cracking of the deposit was observed in both matrix and MMC overlays. The cracks in the matrix alloys (although rare) occurred in the interdendritic areas and revealed possible liquation (Figure 6.1) cracking and/or porosity in the deposit. For the MMCs examined, cracking was also found to propagate straight through WC particles in for example the composite made using Colmonoy 6 (Figure 6.2) and was prevalent most in the high hardness matrix alloy MMCs, which suggests it is due to thermal stresses that would be better accommodated in a softer matrix.
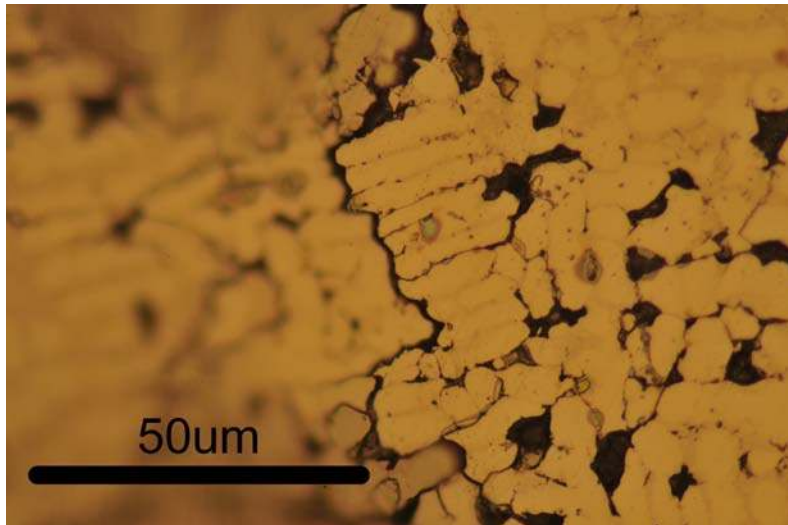
Figure 6.1. Liquation cracking in Deloro 40 matrix alloy.
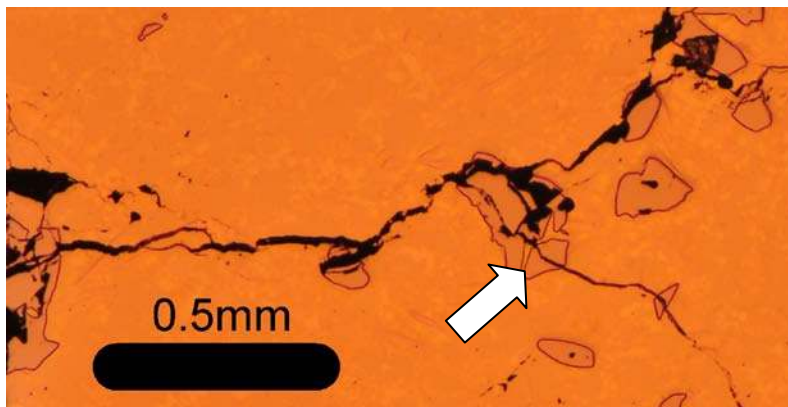
Figure 6.2. Cracks propagating through the WC particles (indicated by arrow) in Colmonoy 6.

6.3. Wear

The WC reinforcing particles increased the wear resistance of the matrix alloys by a factor of two to five times compared to the matrix Ni-alloy alone. As expected, the low hardness matrix alloys benefited the most from the addition of WC reinforcing particles. The low nominal hardness alloys in general had lower C wt% and Figure 6.3 shows the relation between the wear rate and C wt%. Disregarding the Cr-free alloys (they obtain their hardness from other phases such as Ni_3B), there is a good correlation between the wear rate and carbon content. A

higher carbon content will promote the formation of chromium carbides which in turn results in a harder matrix. In an abrasive wear situation, the load is applied mostly to the reinforcing particles since any of the softer matrix phase between particles would either be gouged out or plastically deform away from the abrading surface/particles [23]. If the hard phase structures in the composite coatings form a load support system, it limits the amount of load transmitted to individual particles and hence ensures the particles are not at their mechanical and adhesive limits [23, 71]. When a particularly hard matrix material is used, it may not be able to absorb energy during abrasive particle impacts [72] and lead to chipping and accelerated removal of the matrix which ultimately leads to the reinforcing particles decohering from the matrix and being removed as well.
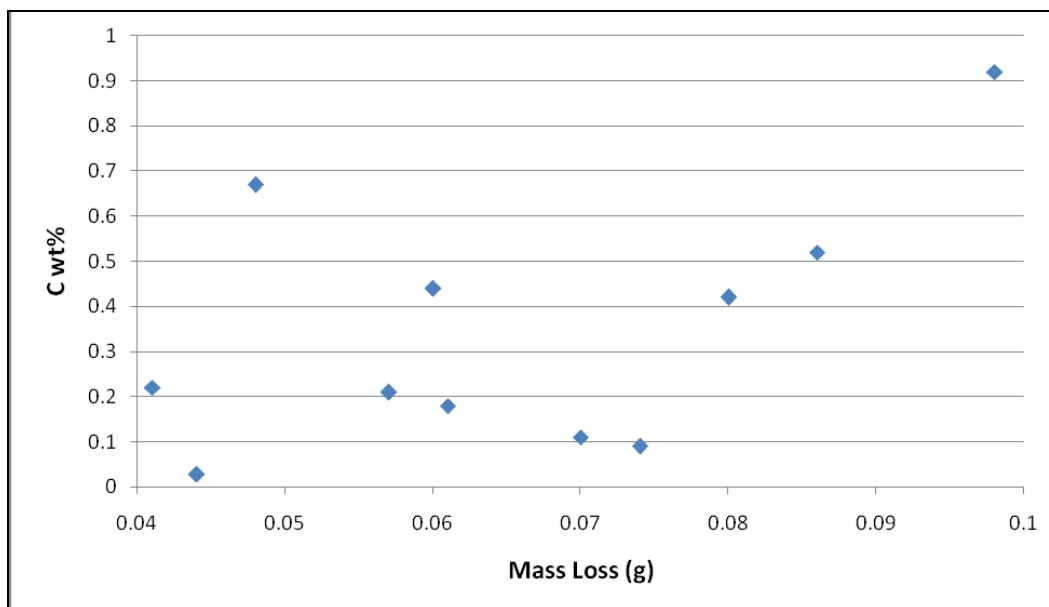
Figure 6.3. Wear rate vs. matrix C wt% for MMC overlays.

The relative size of abrasive particles to the reinforcing particles and their spacing in the metal matrix of an MMC also has an influence on wear resistance. Wear in the 3-body loading situation of the ASTM G65 test mainly results from the loss of matrix when the abrasive particles are small (low stress abrasion), while it could result more from microcracking and particle pull-out when the abrasive is large (high stress abrasion) [72]. However, a size ratio around 1:1 could facilitate the penetration of the abrasive particles into the matrix to damage

both the matrix and the reinforcement, thus enhancing the wear attack [72]. For the alloys examined, the WC particles were up to 180μm in size with an average size of 100μm and the sand particles were between 200-300μm and so the WC particle size versus abrasive size ratio ranges from approximately 1:1 to 1:2. As such, the mechanisms of matrix damage, microcracking, and particle pull-out are expected to be the major causes of wear in the MMC overlays examined. Examination of the wear scars showed matrix damage and microcracking of WC particles but little evidence of particle pull-out was found.

In the case of Ni-WC deposits which exhibited a high level of WC dissolution (eg. that which utilized Colmonoy 6 alloy), there is a higher mean free path (sometimes >200μm) between particles. Considering the sand used during wear testing has a size from 200 to 300 μm, it is possible for silica abrasive to fit between the WC particles and readily gouge out the metal matrix. Figure 6.4 shows a good correlation between the mean free path (between WC particles) and the wear rate, where a higher mean free path leads to a higher wear rate. Once a portion of the matrix is removed, the sand is also able to slide between and impact the sides of the WC particles, leading to shear loads being imposed on the WC particles (fracturing the edge of the WC particle as in Figure 6.5) rather than a compressive load it would experience if impacted from above. This loading situation is more detrimental to the WC particles, leading to more fracture since ceramics generally perform better under compressive loads. This can explain some of the differences in the wear resistance in which Ni-WC overlays exhibiting higher WC dissolution did not perform as well as those experiencing minimal WC dissolution. However, this chipping of the WC particle edges can still occur in some locations in the overlays with low WC dissolution. For example, Figure 6.6 shows the wear surface of the MMC produced using Hoganas 1559-SP329 alloy where it appears the edges of a WC particle have been fracture away (indicated by arrows). This was observed in the other alloys examined as well, but was most prevalent in high dissolution alloys (shown in Appendix E).
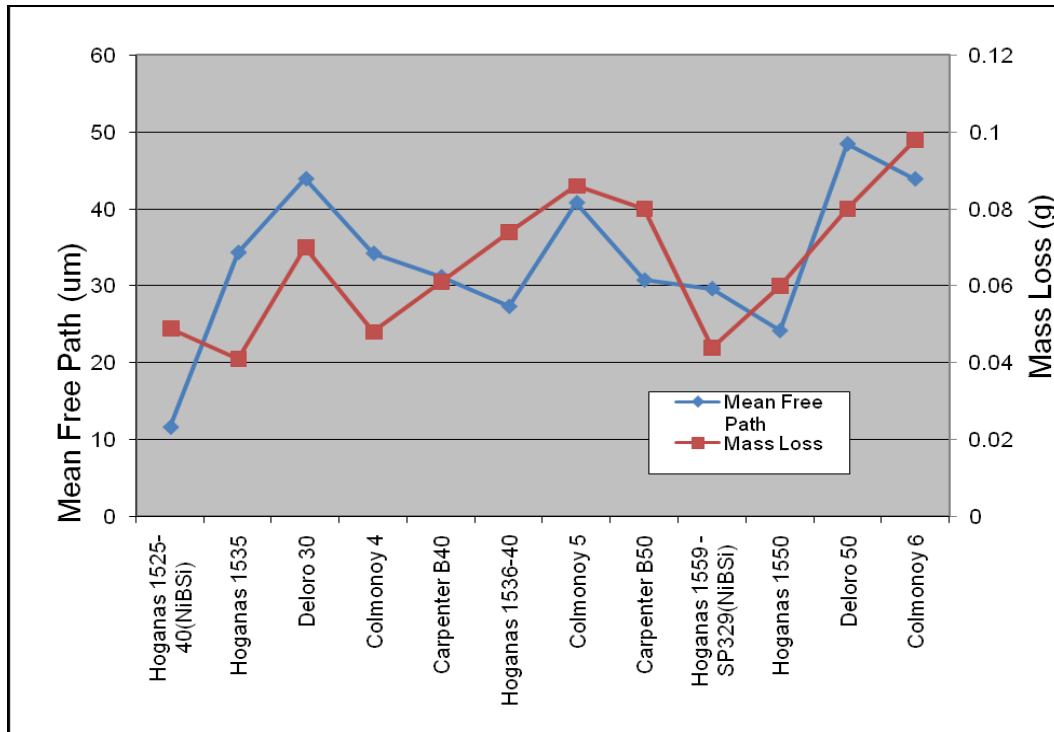
Figure 6.4. Mean free path vs. wear rate for Ni-WC overlays.
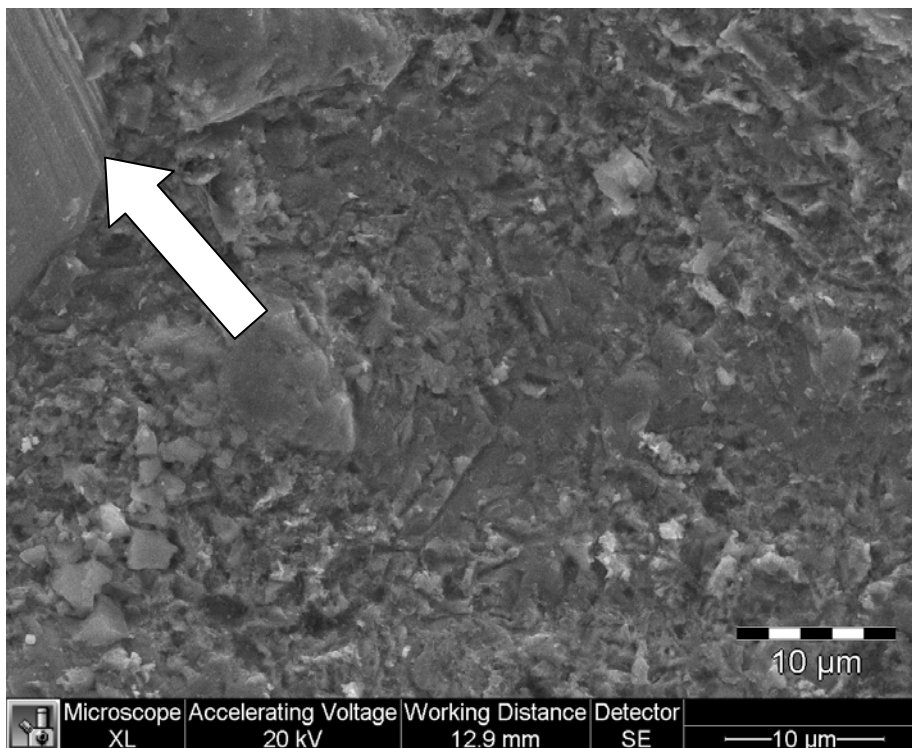
Figure 6.5. SEM wear scar image of the Ni-WC composite utilizing Colmonoy 4 alloy (arrow indicating fractured surface of WC particle).
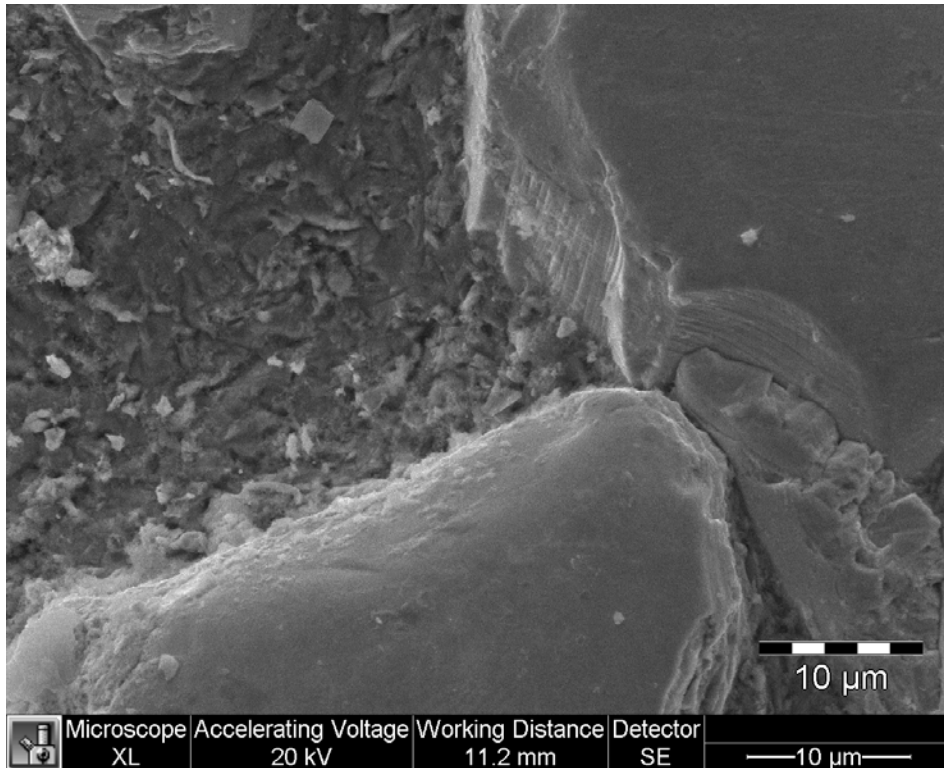
Figure 6.6. SEM wear scar image of the Ni-WC composite utilizing Hoganas 1559-SP329 (Cr-free) alloy (arrows indicating fractured surfaces of WC particle).

As discussed in section #3 , the high hardness matrix alloys have a lower dendrite fraction which reduces the potential for the material to plastically deform and absorb impact during abrassive wear, while the more abundant interdendritic areas (Figure 3.7) undergo brittle failure (shown in Figure 6.7) and are worn away to expose the edges of the WC particles to impacts by the abrasive media.

Ductile failure (dimpling) of nickel-phase dendrites

Cleavage of Interdendrite phases

(d) 20KV X2000 10U
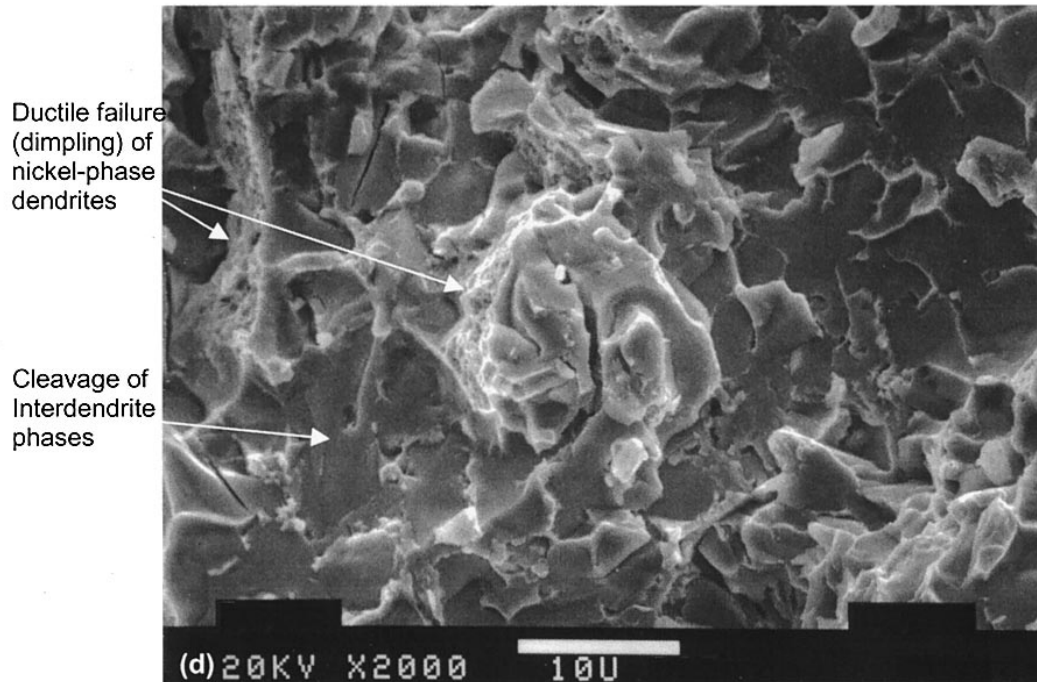
Figure 6.7. Microstructure at the fracture surface of Colmonoy 5 hardfacing K_{IC} specimens in the region of monotonic loading showing brittle cleavage [7].

It has been suggested that secondary carbides which form as a result of dissolution around the reinforcing WC phase aid in wear resistance as they bind the WC particles more strongly to the matrix and prevent particle pull out [17, 48]. However, analysis of wear scars by SEM did not show evidence of particle pull-out in the wear scars examined from 5 different MMC deposits exhibiting a wide range of WC dissolution values. As such, the reinforcement/matrix interface strength does not appear to have a major influence on the wear performance in the MMC deposits considered in the present study.

6.4. Summary of Ni-WC composite overlays

The Ni-WC MMC overlays examined showed similar microstructures and phases to that of the matrix alloys, however there were also other secondary phases that formed during deposition as a result of WC particle dissolution. A Cr-free alloy (Hoganas 1559-SP329) showed little dissolution, a medium-Cr alloy (Deloro 50) had small secondary carbides (approximately $Cr_7W_3C_6$) surrounding

WC particles, and a high-Cr alloy (Colmonoy 6) had large, blocky secondary carbides (approximately $Ni_4Cr_5Si_2W_4C_{4.5}$), which were found to be particularly brittle.

The average hardness of the MMC overlays increased by as much as two times with the addition of WC particles. In terms of wear loss, the MMC overlays were from two to five times more wear resistant than the matrix alloys without the WC particles. The MMCs with the softer matrix alloys generally performed better than those with hard matrix alloys. It is suggested that this is due to the presence of brittle secondary phases, less energy absorption by the matrix, and a larger mean free path between WC particles (due to dissolution) in the MMC overlays exhibiting more WC dissolution when high Cr-content matrix alloys are used. Particle pull-out, which has been observed in previous studies, was not widely observed in the wear samples examined.

7. Conclusions

7.1. Nickel Matrix Overlay Alloys

The microstructure of all NiCrBSi alloys examined were similar, consisting of γ-Ni dendrites, with varying fractions of interdendritic phases comprised of Ni-based eutectics (Ni/Ni$_3$B and Ni/Ni$_3$Si) along with Cr-based borides and carbides. The microstructure of a low-Cr alloy (Deloro 30) was found to consist of 61.6vol% γ-Ni dendrites and fewer interdendritic regions containing Cr-rich particles. A high-Cr alloy (Deloro 50) contained a significantly larger volume fraction of Cr-particles and interdendritic regions containing Cr-rich particles and Ni- borides and silicides.

The hardness of a typical NiCrBSi alloy deposit is controlled not only by the amount of Cr-rich particles present but also by the volume fraction of the hard interdendritic phases such as Ni$_3$B and Ni$_3$Si. As such B and Si, whose primary purpose was thought to be as melting point suppressants, actually make a significant contribution to the overall hardness of the deposit through the formation of Ni-borides and Ni-silicides. The interdendritic phase in the high-Cr (Deloro 50) alloy was found to exhibit high hardness of about 860HV relative to the primary dendritic phase which had a hardness of about 405 HV. Since the volume fraction of the interdendritic phases was higher for the harder Deloro 50 alloy (~55% versus ~35% for the softer Deloro 30 alloy), it significantly contributes to the overall properties of the deposit.

Although there was only a minor increase in Cr, C, and B content in Deloro 50, this lead to a large increase in the amount of Cr-particles from 1.4vol% to about 14vol% between the two alloys examined. Ternary phase diagrams suggest the addition of Fe or Si will decrease the solubility of Cr in Ni, however no significant change in Cr segregation was observed in the alloy compositions examined. It was also found that boron segregates to the interdendritic regions in both alloys and promotes formation of Ni$_3$B and CrB.

7.2. Ni-WC Composites

The MMC overlays produced similar microstructures and phases to that of the matrix alloys, however there were also other secondary phases that formed during deposition as a result of WC particle dissolution. The dissolution of WC particles appeared to be proportional to the alloying additions (Cr, C, etc.), where higher alloying additions resulted in higher WC particle dissolution. A Cr-free alloy (Hoganas 1559-SP329) showed very little dissolution, a medium-Cr alloy (Deloro 50) had small secondary carbides (approximately $Cr_7W_3C_6$) surrounding WC particles, and a high-Cr alloy (Colmonoy 6) had large, blocky secondary carbides (approximately $Ni_4Cr_5Si_2W_4C_{4.5}$).

The average hardness of the MMC overlays increased with the addition of WC particles and was higher for the MMCs with higher hardness matrix alloys. In terms of wear loss, the matrix alloys with higher hardness had higher wear resistance, but when used in MMCs, the Ni-alloys that produced MMCs with lower hardness had better wear resistance. It is suggested that this is due to more brittle secondary phases, less energy absorption by the matrix, and a larger mean free path between WC particles (due to dissolution) in the MMCs using high hardness matrix alloys. In terms of wear modes, only gouging of the matrix and microcracking of the carbides was detected (particle pull-out was not detected). Also, shrinkage cracks were most prevalent in the high hardness matrix alloy MMCs. Considering the previously mentioned factors, it is thus suggested to use a low-Cr matrix alloy with the WC particles to achieve optimum wear properties.

8. Future Work

The 5-component secondary phase found in the Colmonoy 6 MMC appeared to be brittle during microhardness testing. To examine the mechanical properties of the 5-component phase, nanoindentation followed by analysis with the Palmqvist method could be used to determine the toughness of the blocky phase and to see if it is in fact too brittle and detrimental to wear resistance.

The chemistry of the matrix alloy plays a large part in the resulting microstructure of the deposit. The matrix alloys with low alloying elements (Cr, C, B, Si, Fe) had fewer carbides and borides. From the ternary Fe-Cr-Ni and Si-Cr-Ni phase diagrams, it appears that Fe and Si both promote the segregation of Cr to the interdendritic regions. This will then lead to the formation of more carbides and borides which will make the deposit harder. It would thus be ideal to examine more carefully the effect of alloying additions such as Fe and Si (and consequently Cr, C, and B) on the deposit properties by carefully controlling alloy chemistry, which will lead to better alloy design. Thermodynamic modeling (using Thermo-Calc computer software) could also be used to supplement the experimental work and verify results.

In addition, the effect of the alloying additions on WC dissolution could be examined more closely as it was found that alloys such as Colmonoy 6 that had a higher percentage of alloying elements suffered from high WC dissolution (leading to possibly brittle phases) and so performed poorly in wear testing.

Along with wear resistance, corrosion resistance is also required in the oil sands industry as material removal in the presence of abrasive as well as corrosive environments leads to higher wear rates than the simple sum of the two processes. These higher wear rates mean the useful life of equipment is lowered and increases production and maintenance costs.

9. References

1.   Flores, J.F., et al., *An experimental study of the erosion-corrosion behavior of plasma transferred arc MMCs.* Wear, 2009. **267**(1-4): p. 213-222.

2.   Branagan, D.J., M.C. Marshall, and B.E. Meacham, *High toughness high hardness iron based PTAW weld materials.* Materials Science and Engineering: A, 2006. **428**(1-2): p. 116-123.

3.   Badisch, E. and M. Kirchgaßner, *Influence of welding parameters on microstructure and wear behaviour of a typical NiCrBSi hardfacing alloy reinforced with tungsten carbide.* Surface and Coatings Technology, 2008. **202**(24): p. 6016-6022.

4.   Bourithis, L. and G.D. Papadimitriou, *The effect of microstructure and wear conditions on the wear resistance of steel metal matrix composites fabricated with PTA alloying technique.* Wear, 2009. **266**(11-12): p. 1155-1164.

5.   Sudha, C., et al., *Microchemical and microstructural studies in a PTA weld overlay of Ni-Cr-Si-B alloy on AISI 304L stainless steel.* Surface and Coatings Technology, 2008. **202**(10): p. 2103-2112.

6.   Conde, A., F. Zubiri, and y.J. de Damborenea, *Cladding of Ni-Cr-B-Si coatings with a high power diode laser.* Materials Science and Engineering A, 2002. **334**(1-2): p. 233-238.

7.   Cockeram, B., *The fracture toughness and toughening mechanisms of nickel-base wear materials.* Metallurgical and Materials Transactions A, 2002. **33**(1): p. 33-56.

8.   Huang, S.W., M. Samandi, and M. Brandt, *Abrasive wear performance and microstructure of laser clad WC/Ni layers.* Wear, 2004. **256**(11-12): p. 1095-1105.

9.   D'Oliveira, A.S.C.M., R.S.C. Paredes, and R.L.C. Santos, *Pulsed current plasma transferred arc hardfacing.* Journal of Materials Processing Technology, 2006. **171**(2): p. 167-174.

10.   Hart, K.W.D., D.H. Harper, and M.J. Gill, *Case studies in wear resistance using HVOF, PTAW and Spray Fusion surfacing*, in *1st International Thermal Spray Conference*. 2000, Materials Park, OH; ASM International: Montreal, Canada. p. 1117-1125.

11.   Cockeram, B.V., *Fracture toughness testing and toughening mechanisms of some commercial cobalt-free hardfacing alloys.* Surface and Coatings Technology, 1998. **108-109**(1-3): p. 377-384.

12.   Yan, M. and W.Z. Zhu, *Surface remelting of Ni-Cr-B-Si cladding with a micro-beam plasma arc.* Surface and Coatings Technology, 1997. **92**(1-2): p. 157-163.

13.   Sari, N.Y. and M. Yilmaz, *Improvement of wear resistance of wire drawing rolls with Cr-Ni-B-Si + WC thermal spraying powders.* Surface and Coatings Technology, 2008. **202**(13): p. 3136-3141.
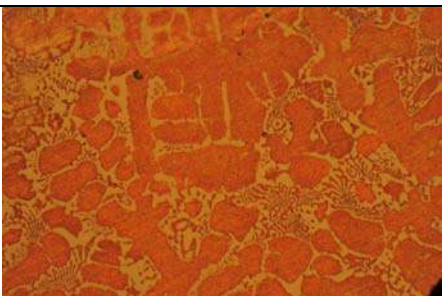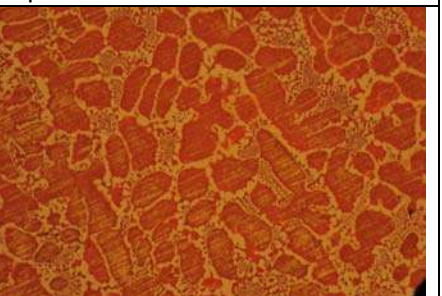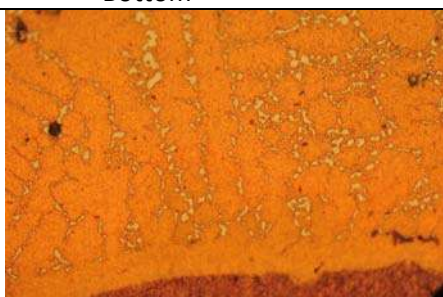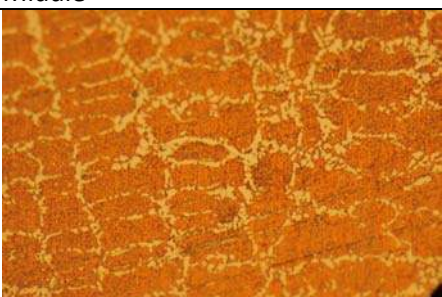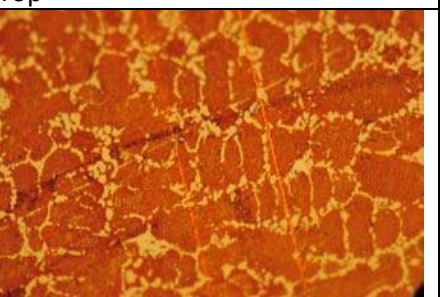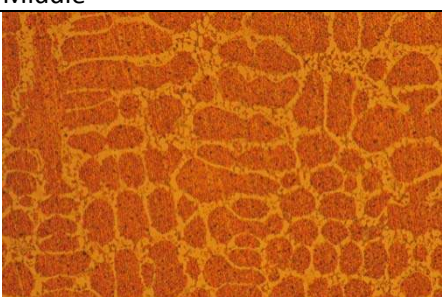
14. Shieh, Y.-H., et al., *Alloying and post-heat-treatment of thermal-sprayed coatings of self-fluxing alloys.* Surface and Coatings Technology, 1993. **58**(1): p. 73-77.

15. Lebaili, S., M. Durand-Charre, and S. Hamar-Thibault, *The metallurgical structure of as-solidified Ni-Cr-B-Si-C hardfacing alloys.* Journal of Materials Science, 1988. **23**(10): p. 3603-3611.

16. Grigorescu, I.C., et al., *Phase characterization in Ni alloy-hard carbide composites for fused coatings.* Surface and Coatings Technology, 1995. **76-77**(Part 2): p. 494-498.

17. Tobar, M.J., et al., *Morphology and characterization of laser clad composite NiCrBSi-WC coatings on stainless steel.* Surface and Coatings Technology, 2006. **200**(22-23): p. 6313-6317.

18. Kim, H.J. and Y.J. Kim, *Wear and corrosion resistance of PTA weld surfaced Ni and CO based alloy layers.* Surface Engineering, 1999. **15**: p. 495-501.

19. Lin, M.C., et al., *A study of high-speed slurry erosion of NiCrBSi thermal-sprayed coating.* Surface and Coatings Technology, 2006. **201**(6): p. 3193-3198.

20. Sidhu, T.S., S. Prakash, and R.D. Agrawal, *Characterisations of HVOF sprayed NiCrBSi coatings on Ni- and Fe-based superalloys and evaluation of cyclic oxidation behaviour of some Ni-based superalloys in molten salt environment.* Thin Solid Films, 2006. **515**(1): p. 95-105.

21. Gassmann, R.C., *Laser cladding with (WCW2C)/CoCrC and (WCW2C)/NiBSi composites for enhanced abrasive wear resistance.* Materials Science and Technology, 1996. **12**: p. 691-696.

22. Suh, N.P., *Tribophysics.* 1986, New Jersey: Prentice-Hall.

23. Wang, H., W. Xia, and Y. Jin, *A study on abrasive resistance of Ni-based coatings with a WC hard phase.* Wear, 1996. **195**(1-2): p. 47-52.

24. Vedani, M., et al., *Influence of interface properties on mechanical behaviour of particle reinforced metal matrix composite.* Materials Science and Technology, 1994. **10**: p. 132-140.

25. Navas, C., et al., *Abrasive wear behaviour of laser clad and flame sprayed-melted NiCrBSi coatings.* Surface and Coatings Technology, 2006. **200**(24): p. 6854-6862.

26. Zhang, L., D. Sun, and H. Yu, *Effect of niobium on the microstructure and wear resistance of iron-based alloy coating produced by plasma cladding.* Materials Science and Engineering: A, 2008. **490**(1-2): p. 57-61.

27. Kim, H.-J., et al., *Assessment of wear performance of flame sprayed and fused Ni-based coatings.* Surface and Coatings Technology, 2003. **172**(2-3): p. 262-269.

28. Bourithis, L. and G. Papadimitriou, *Three body abrasion wear of low carbon steel modified surfaces.* Wear, 2005. **258**(11-12): p. 1775-1786.

29. Martín, A., et al., *Sliding wear behaviour of plasma sprayed WC-NiCrBSi coatings at different temperatures.* Wear, 2001. **251**(1-12): p. 1017-1022.
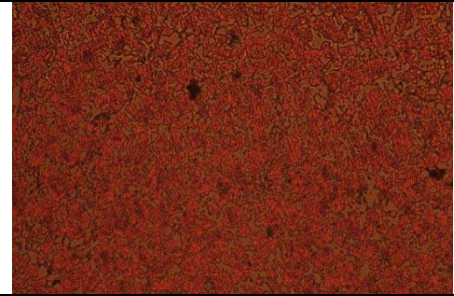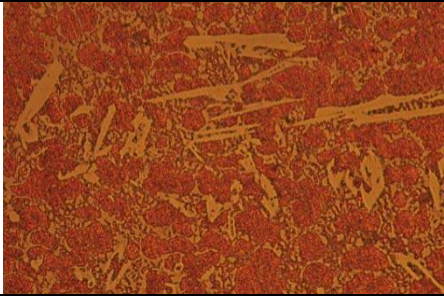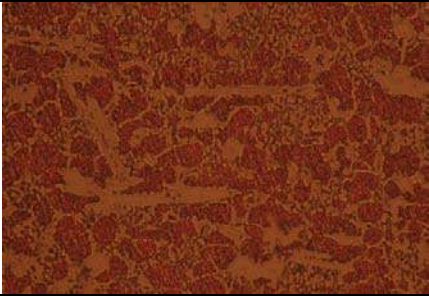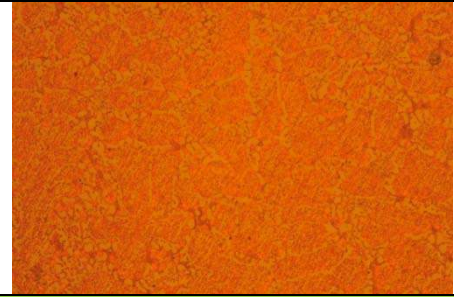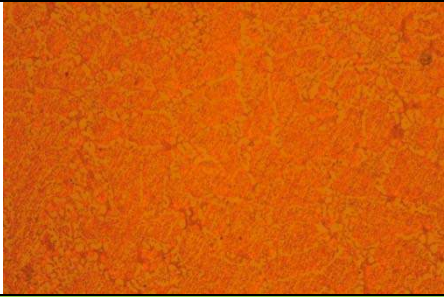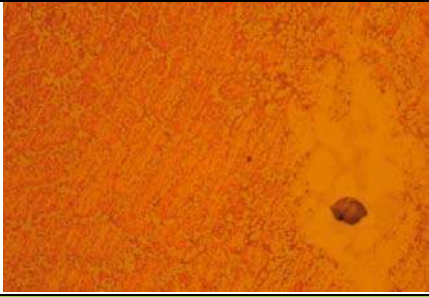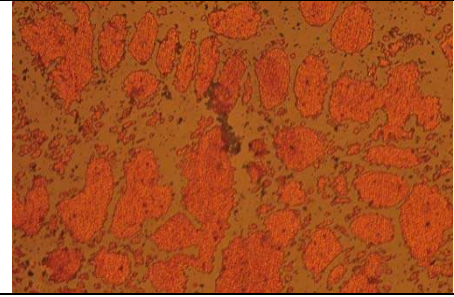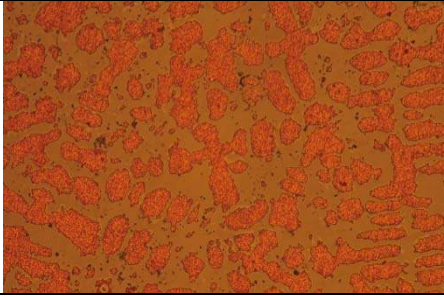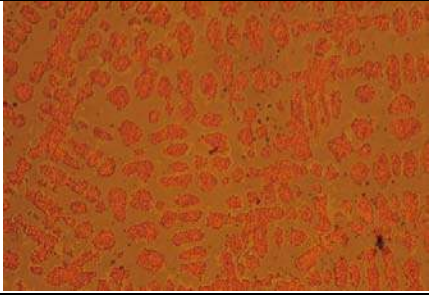
30. Van Acker, K., et al., *Influence of tungsten carbide particle size and distribution on the wear resistance of laser clad WC/Ni coatings.* Wear, 2005. **258**(1-4): p. 194-202.

31. Liao, H., B. Normand, and C. Coddet, *Influence of coating microstructure on the abrasive wear resistance of WC/Co cermet coatings.* Surface and Coatings Technology, 2000. **124**(2-3): p. 235-242.

32. Bolelli, G., L. Lusvarghi, and R. Giovanardi, *A comparison between the corrosion resistances of some HVOF-sprayed metal alloy coatings.* Surface and Coatings Technology, 2008. **202**(19): p. 4793-4809.

33. Gruzdys, E., et al., *Effects of Heating by Arc Discharge on Structure and Chemical Composition of Coatings Formed Using High Velocity Oxygen Fuel and Flame Spraying Processes.* Materials Science, 2008. **14**(3): p. 4.

34. Li, C., Y. Wang, and H. Li, *Effect of nano-crystallization of high velocity oxy-fuel-sprayed amorphous NiCrBSi alloy on properties of the coatings.* The Journal of Vacuum Science and Technology A, 2004. **22**(5): p. 5.

35. Verdon, C., A. Karimi, and J.L. Martin, *A study of high velocity oxy-fuel thermally sprayed tungsten carbide based coatings. Part 1: Microstructures.* Materials Science and Engineering A, 1998. **246**(1-2): p. 11-24.

36. Xu, G., et al., *Characteristics of Ni-based coating layer formed by laser and plasma cladding processes.* Materials Science and Engineering: A, 2006. **417**(1-2): p. 63-72.

37. Kaul, R., et al., *Laser Cladding of Austenitic Stainless Steel with Hardfacing Alloy Nickel Base.* Surface Engineering, 2003. **19**: p. 269-273.

38. González, R., et al., *Microstructural study of NiCrBSi coatings obtained by different processes.* Wear, 2007. **263**(1-6): p. 619-624.

39. Conde, A., F. Zubiri, and J. de Damborenea, *Cladding of Ni-Cr-B-Si coatings with a high power diode laser.* Materials Science and Engineering a-Structural Materials Properties Microstructure and Processing, 2002. **334**(1-2): p. 233-238.

40. Gómez-del Río, T., et al., *Influence of the deposition techniques on the mechanical properties and microstructure of NiCrBSi coatings.* Journal of Materials Processing Technology, 2008. **204**(1-3): p. 304-312.

41. Nurminen, J., J. Näkki, and P. Vuoristo, *Microstructure and properties of hard and wear resistant MMC coatings deposited by laser cladding.* International Journal of Refractory Metals and Hard Materials, 2009. **27**(2): p. 472-478.

42. Hirota, K., et al., *Simultaneous synthesis and consolidation of chromium carbides (Cr3C2, Cr7C3 and Cr23C6) by pulsed electric-current pressure sintering.* Materials Science and Engineering: A, 2005. **399**(1-2): p. 154-160.

43. ASM Handbook Committee., *ASM handbook comprehensive index.* 2nd ed. 2000, Materials Park, Ohio: ASM International. iv, 1189 p.

44. Finch, C.B., O.B. Cavin, and P.F. Becher, *Crystal growth and properties of trinickel boride, Ni3B.* Journal of Crystal Growth, 1984. **67**(3): p. 556-558.
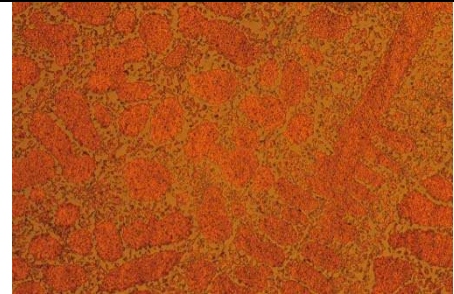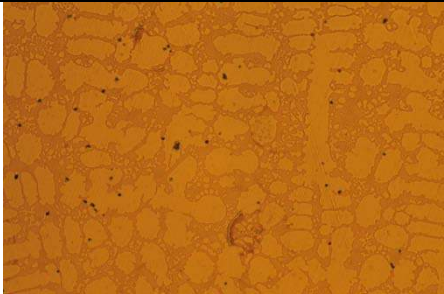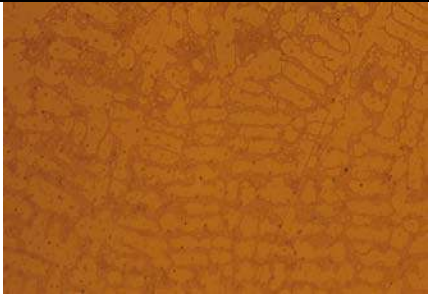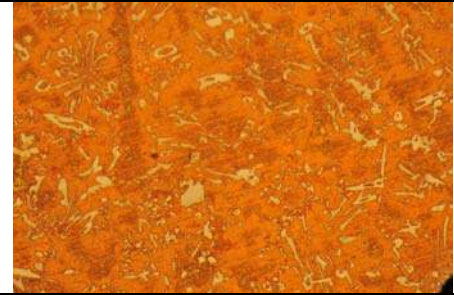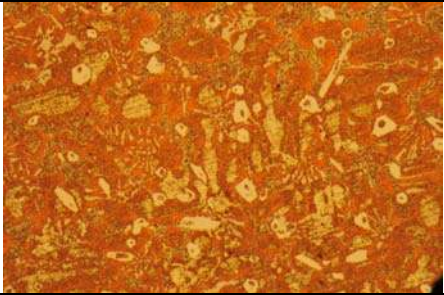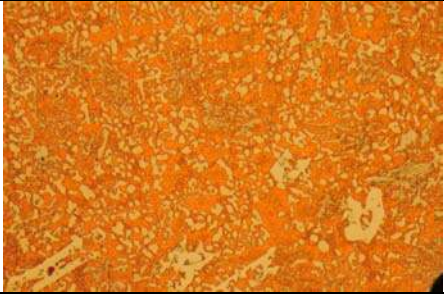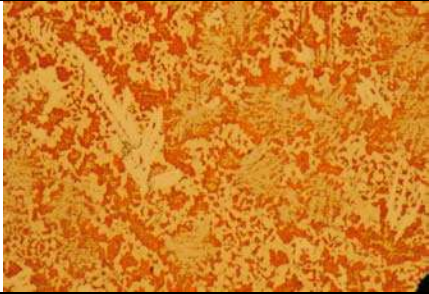
45.   González, R., et al., *Wear behaviour of flame sprayed NiCrBSi coating remelted by flame or by laser.* Wear, 2007. **262**(3-4): p. 301-307.

46.   Fernández, E., et al., *Wear behaviour of laser clad NiCrBSi coating.* Wear. **259**(7-12): p. 870-875.

47.   Itoh, M., K. Takaishi, and S. Kawano. *Development of Cobalt-free wear resistance coating.* in *7th International Conference on Nuclear Engineering.* 1999. Tokyo, Japan.

48.   Just, C., E. Badisch, and J. Wosik, *Influence of welding current on carbide/matrix interface properties in MMCs.* Journal of Materials Processing Technology, 2010. **210**(2): p. 408-414.

49.   Li, Q., T.C. Lei, and W.Z. Chen, *Microstructural characterization of WCp reinforced Ni-Cr-B-Si-C composite coatings.* Surface and Coatings Technology, 1999. **114**(2-3): p. 285-291.

50.   Nam, D., J. Do, and S. Lee, *Improvement of hardness and fracture toughness of surface composites fabricated by high-energy electron-beam irradiation with Fe-alloy powders and VC powders.* Scripta Materialia, 2009. **60**(8): p. 695-698.

51.   Neville, A., et al., *Assessing Metal Matrix Composites for Corrosion and Erosion-Corrosion Applications in the Oil Sands Industry* Corrosion, 2006. **62**(8): p. 19.

52.   Buytoz, S., M. Ulutan, and M.M. Yildirim, *Dry sliding wear behavior of TIG welding clad WC composite coatings.* Applied Surface Science, 2005. **252**(5): p. 1313-1323.

53.   Karimi, A. and C. Verdon, *Hydroabrasive wear behaviour of high velocity oxyfuel thermally sprayed WC-M coatings.* Surface and Coatings Technology, 1993. **62**(1-3): p. 493-498.

54.   Karimi, A., C. Verdon, and G. Barbezat, *Microstructure and hydroabrasive wear behaviour of high velocity oxy-fuel thermally sprayed WC---Co(Cr) coatings.* Surface and Coatings Technology, 1993. **57**(1): p. 81-89.

55.   Zuercher, M.H. and D.G. Morris, *Crystallization in Ni-Si-B glass: the influence of dispersoid additions.* Journal of Materials Science, 1990. **25**(11): p. 4717-4725.

56.   Wu, P., C.Z. Zhou, and X.N. Tang, *Microstructural characterization and wear behavior of laser cladded nickel-based and tungsten carbide composite coatings.* Surface and Coatings Technology, 2003. **166**(1): p. 84-88.

57.   Babu, S., et al., *Toward prediction of microstructural evolution during laser surface alloying.* Metallurgical and Materials Transactions A, 2002. **33**(4): p. 1189-1200.

58.   Stoica, V., R. Ahmed, and T. Itsukaichi, *Influence of heat-treatment on the sliding wear of thermal spray cermet coatings.* Surface and Coatings Technology, 2005. **199**(1): p. 7-21.

59.   Przybylowicz, J. and J. Kusinski, *Structure of laser cladded tungsten carbide composite coatings.* Journal of Materials Processing Technology, 2001. **109**(1-2): p. 154-160.
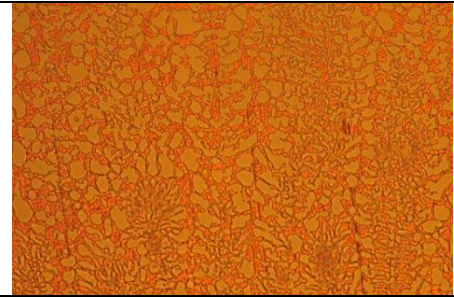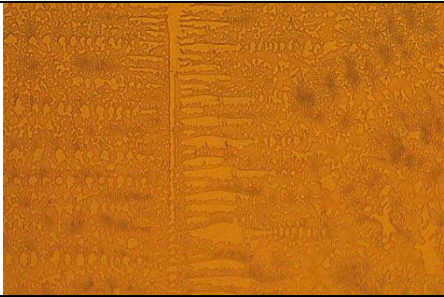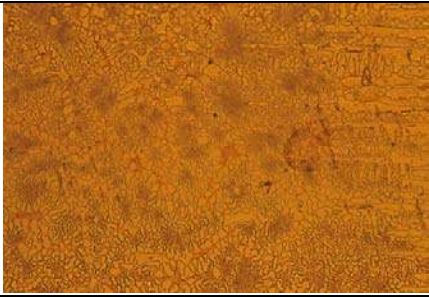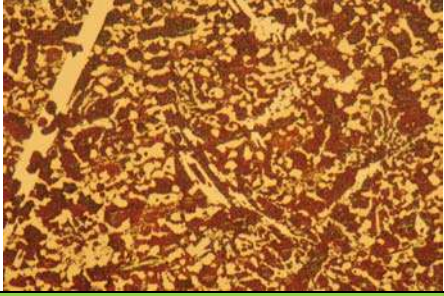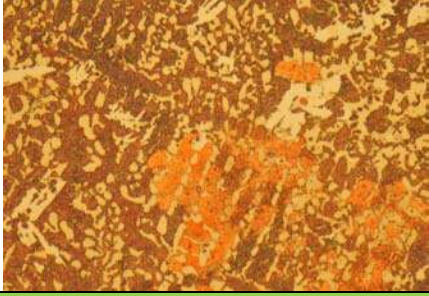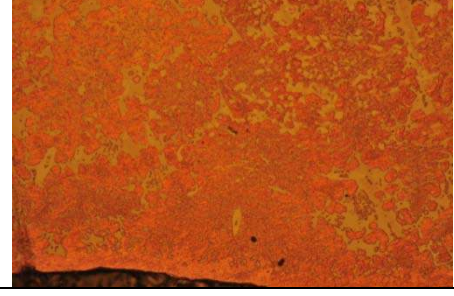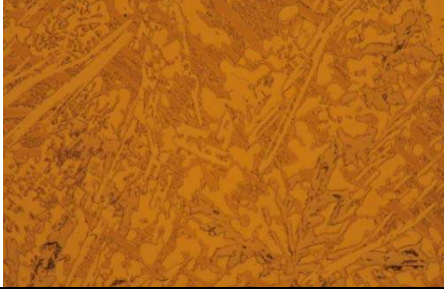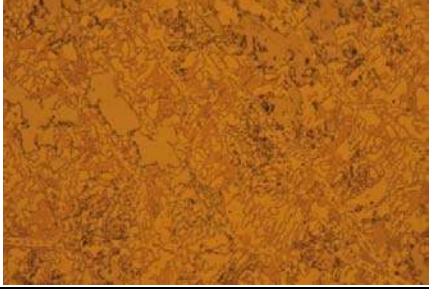
60. Cerri, W., et al., *Laser deposition of carbide-reinforced coatings.* Surface and Coatings Technology, 1991. **49**(1-3): p. 40-45.

61. Polak, R., S. Ilo, and E. Badisch, *Relation Between Inter-Particle Distance (LIPD) and Abrasion in Multiphase Matrix–Carbide Materials.* Tribology Letters, 2009. **33**(1): p. 29-35.

62. Neville, A., et al., *Erosion-corrosion behaviour of WC-based MMCs in liquid-solid slurries.* Wear, 2005. **259**(1-6): p. 181-195.

63. Yarmuch, M., *Effect of welding parameters on the plasma transferred arc welding (PTAW) process for autogenous beads and 410SS-WC overlays*, in *Chemical and Materials Engineering*. 2005, University of Alberta: Edmonton. p. 201.

64. Nam, D., K. Lee, and S. Lee, *Correlation of Microstructure with Hardness and Wear Resistance of Carbide-Reinforced Ferrous Surface Composites Fabricated by High-Energy Electron-Beam Irradiation.* Metallurgical and Materials Transactions A, 2008. **39**(11): p. 2626-2634.

65. Bauccio, M., *ASM engineered materials reference book*. 2nd ed. 1994, Materials Park, OH: ASM International. v, 580 p.

66. Scheil, E., Z. Metallkd. , 1942. **34**: p. 70-72.

67. Dupont, J.N., J.R. Michael, and B.D. Newbury, *Welding metallurgy of alloy HR-160.* Welding Journal, 1999. **78**(12): p. 408s-415s.

68. Milenkovic, S. and R. Caram, *Effect of the growth parameters on the Ni-Ni3Si eutectic microstructure.* Journal of Crystal Growth, 2002. **237-239**(Part 1): p. 95-100.

69. Wolfe, T., in *Chemical and Materials Engineering*. 2010, University of Alberta: Edmonton, Canada.

70. Lim, L.C., Q. Ming, and Z.D. Chen, *Microstructures of laser-clad nickel-based hardfacing alloys.* Surface and Coatings Technology, 1998. **106**(2-3): p. 183-192.

71. Bahadur, S. and C.-N. Yang, *Friction and wear behavior of tungsten and titanium carbide coatings.* Wear, 1996. **196**(1-2): p. 156-163.

72. Hu, J., D.Y. Li, and R. Llewellyn, *Synergistic effects of microstructure and abrasion condition on abrasive wear of composites--A modeling study.* Wear, 2007. **263**(1-6): p. 218-227.
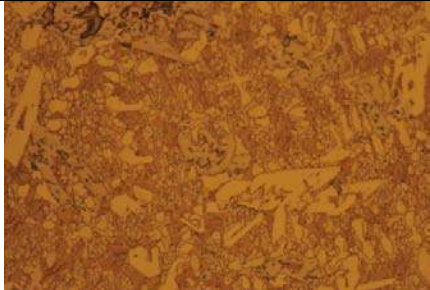
Appendix A-Optical Microscopy Images of Ni-alloy Overlays

Alloy type: • Hoganas 1525-40 (30HRC) • NiBSi	Scale for all images: **100um**	
Bottom	Middle	Top
Alloy type: • Hoganas 1535 (30HRC)		
Bottom	Middle	Top
Alloy type:Deloro 30 (30HRC)		
Bottom	Middle	Top

Alloy type: • Colmonoy 40 (40HRC)		
Bottom	Middle	Top
Alloy type: • Carpenter B40 (40HRC)		
Bottom	Middle	Top
Alloy type: • Hoganas 1536-40 (40HRC)		
Bottom	Middle	Top

Alloy type: • Deloro 40 (40HRC)		
Bottom	Middle	Top
Alloy type: • Colmonoy 50 (50HRC)		
Bottom	Middle	Top
Alloy type: • Carpenter B50 (50HRC)		
Bottom	Middle	Top

Alloy type: • Hoganas 1559-SP329 (50HRC) • NiBSi		
Bottom	Middle	Top
Alloy type: • Hoganas 1550 (50HRC)		
Bottom	Middle	Top
Alloy type: • Deloro 50 (50HRC)		
Bottom	Middle	Top
Alloy type: • Colmonoy 60 (60HRC)		
Bottom	Middle	Top

Alloy type: • Hoganas 1560-00 (60HRC)		
Bottom	Middle	Top

Appendix B-Microhardness Testing of Ni-alloys and Ni-WC Overlays

Microhardness Results for Ni-alloys
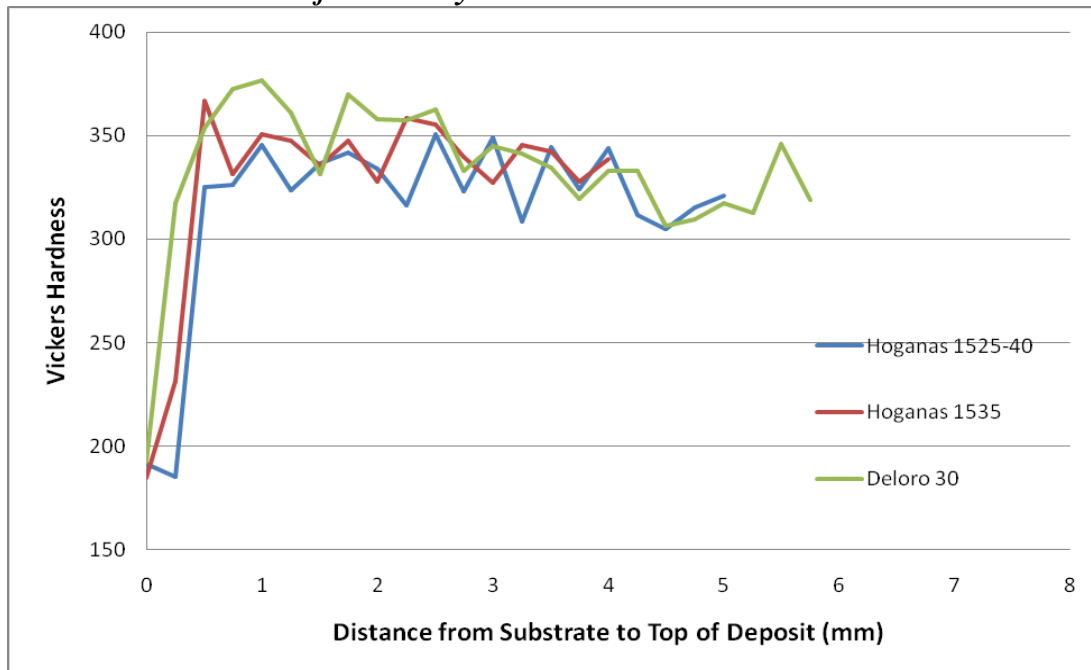
Figure B-1. Microhardness results from 30HRc Ni-alloys.
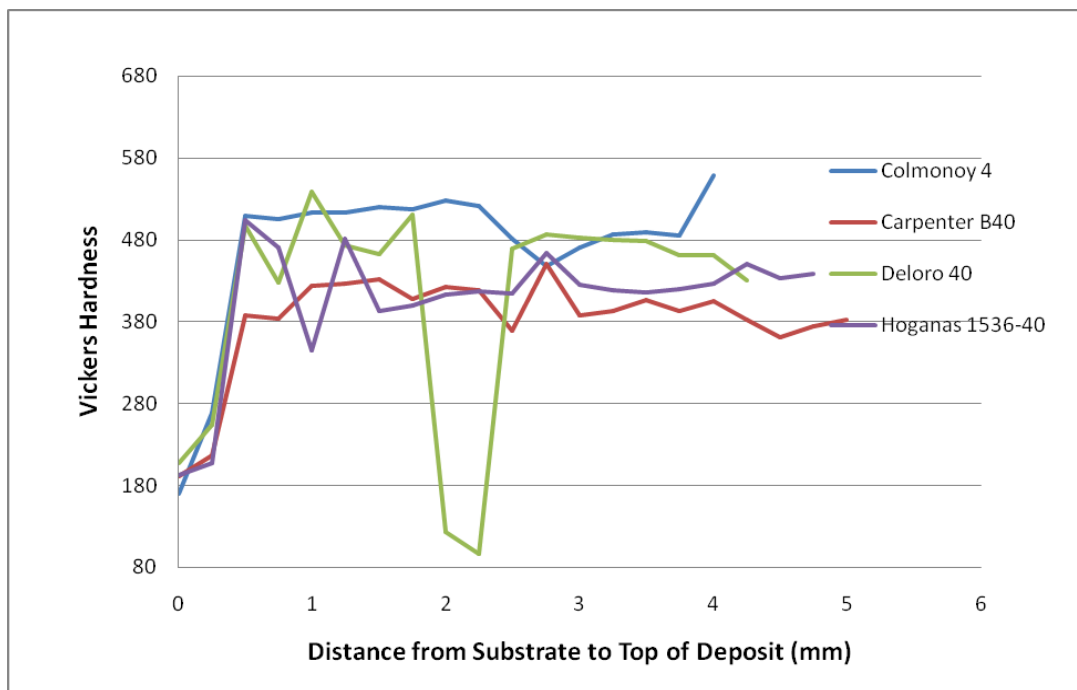
Figure B-2. Microhardness results from 40HRc Ni-alloys.
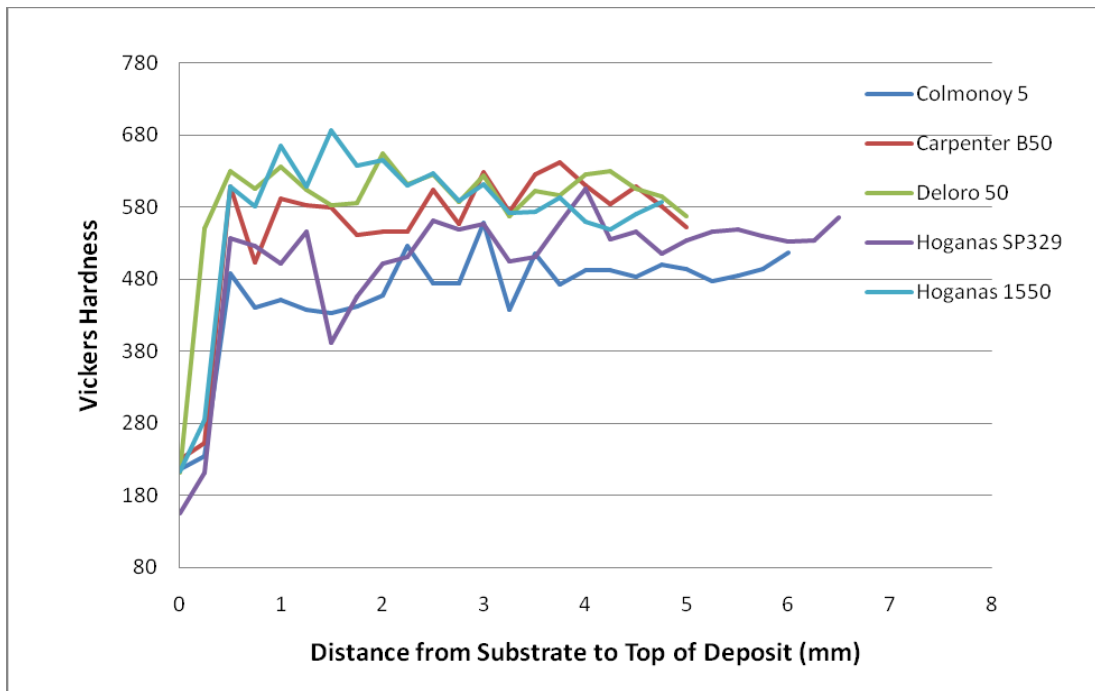
Figure B-3. Microhardness results from 50HRc Ni-alloys.
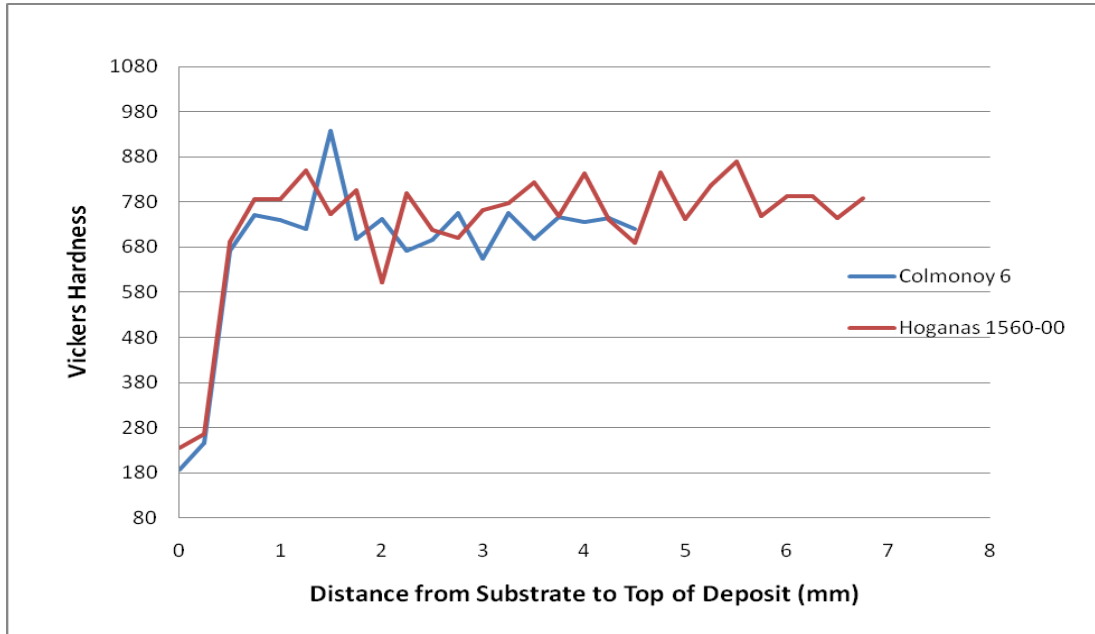
Figure B-4. Microhardness results from 60HRc Ni-alloys.

Microhardness Results for Ni-WC Alloys
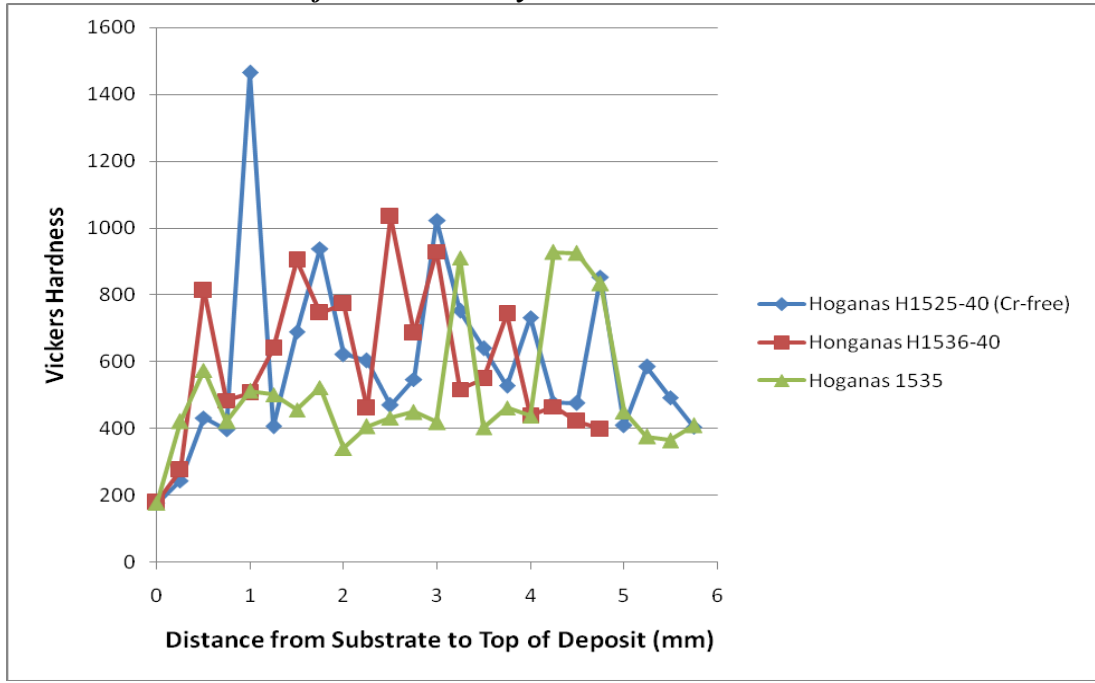
Figure B-5. Microhardness results from 30HRc Ni-WC overlays.
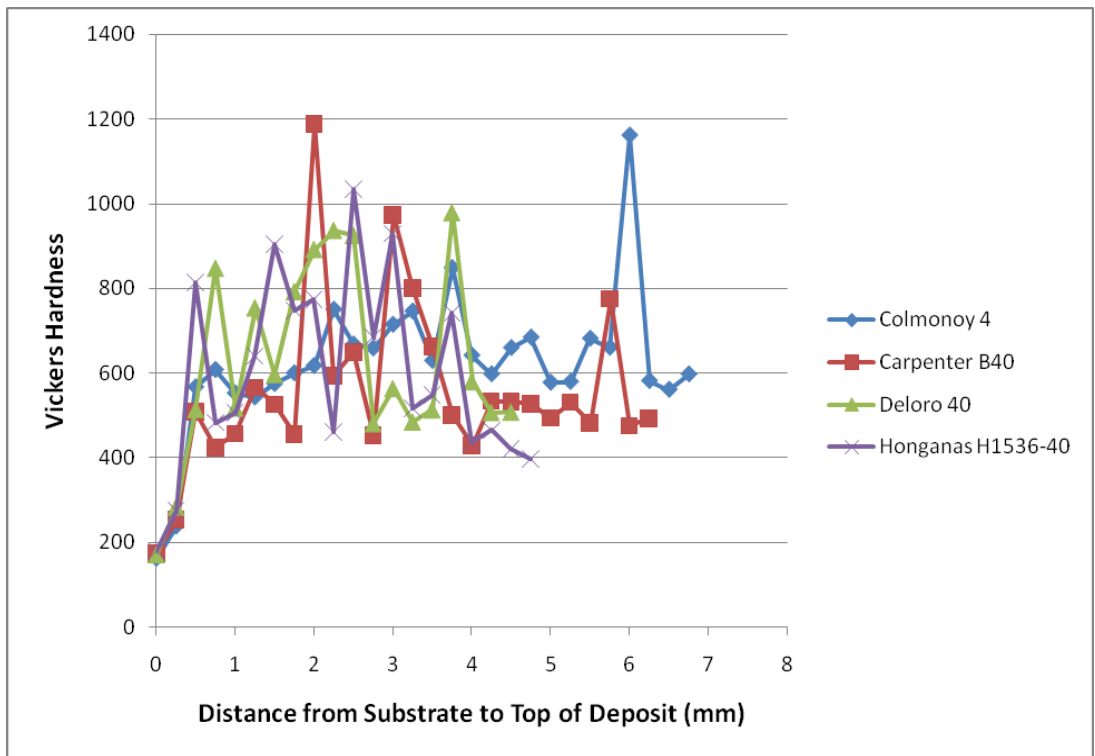
Figure B-6. Microhardness results from 40HRc Ni-WC overlays.
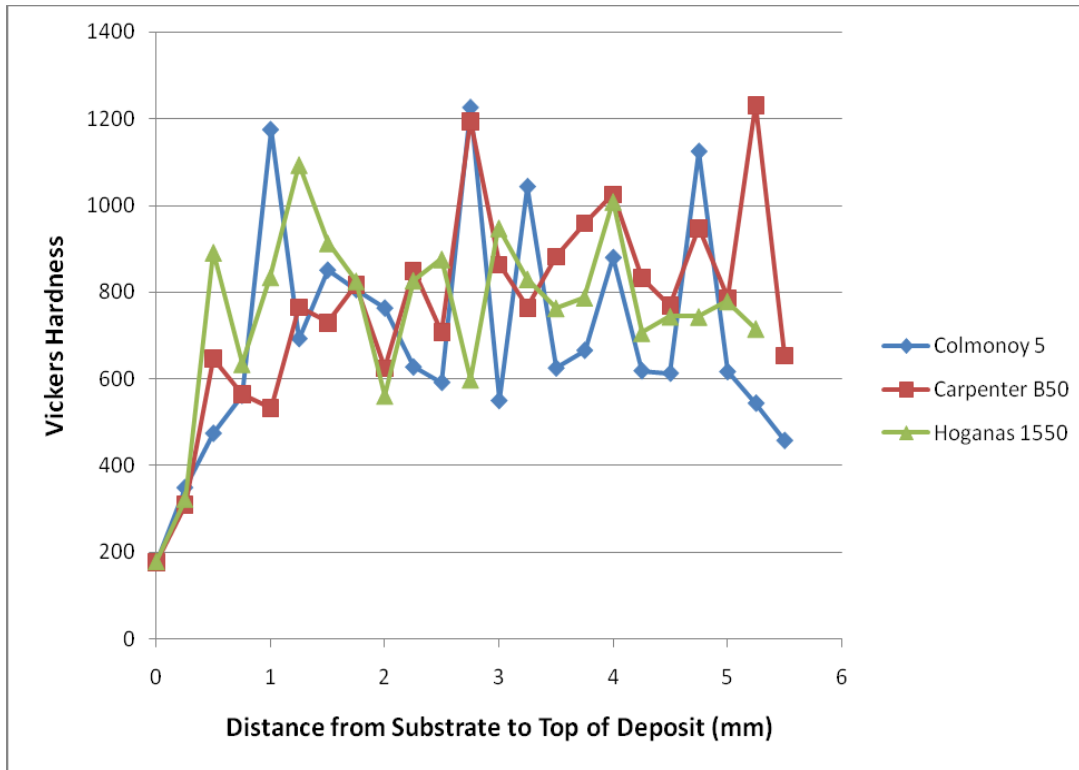
Figure B-7. Microhardness results from 50HRc Ni-WC overlays.
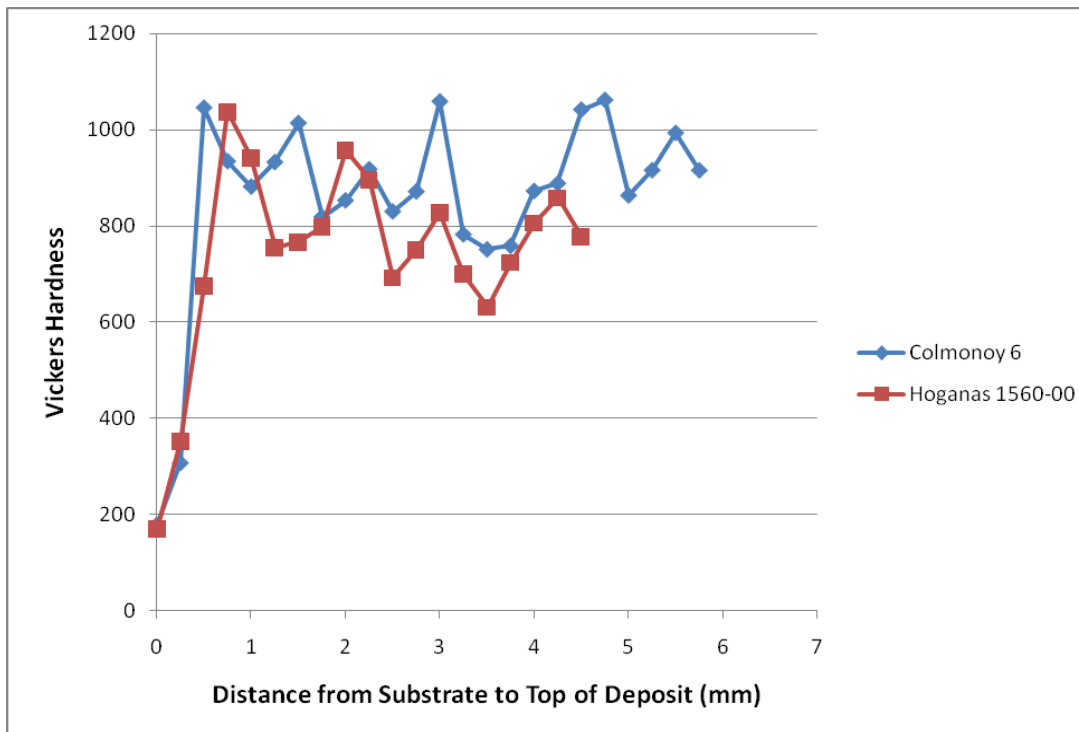
Figure B-8. Microhardness results from 60HRc Ni-WC overlays.

Appendix C-EPMA and AES Results

EPMA Results
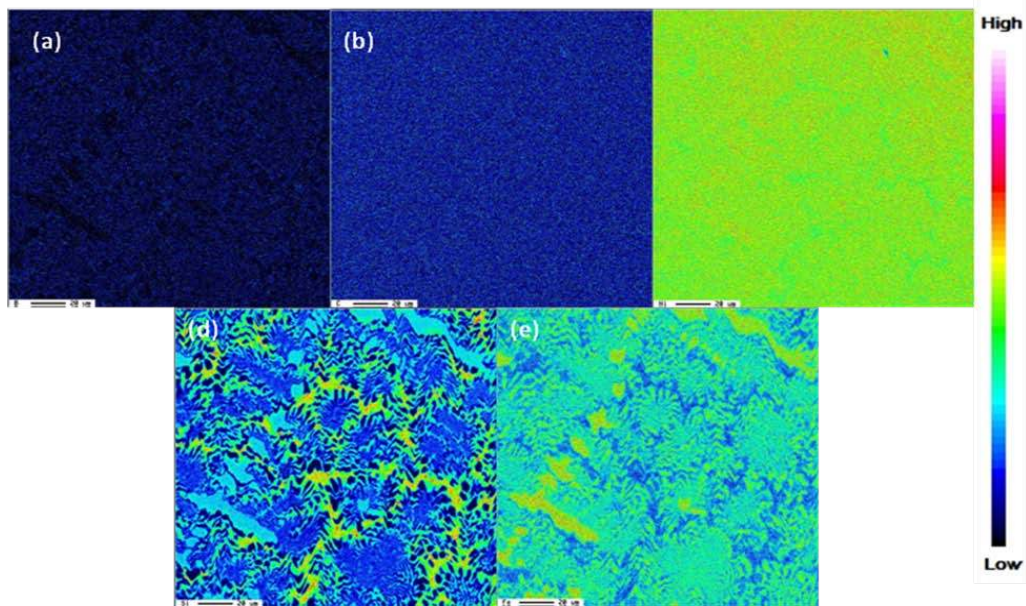
Figure C-1. EPMA area analysis of Hoganas SP329 (Cr-free) showing a)boron, b)carbon, c)nickel, d)silicon, and e)iron.
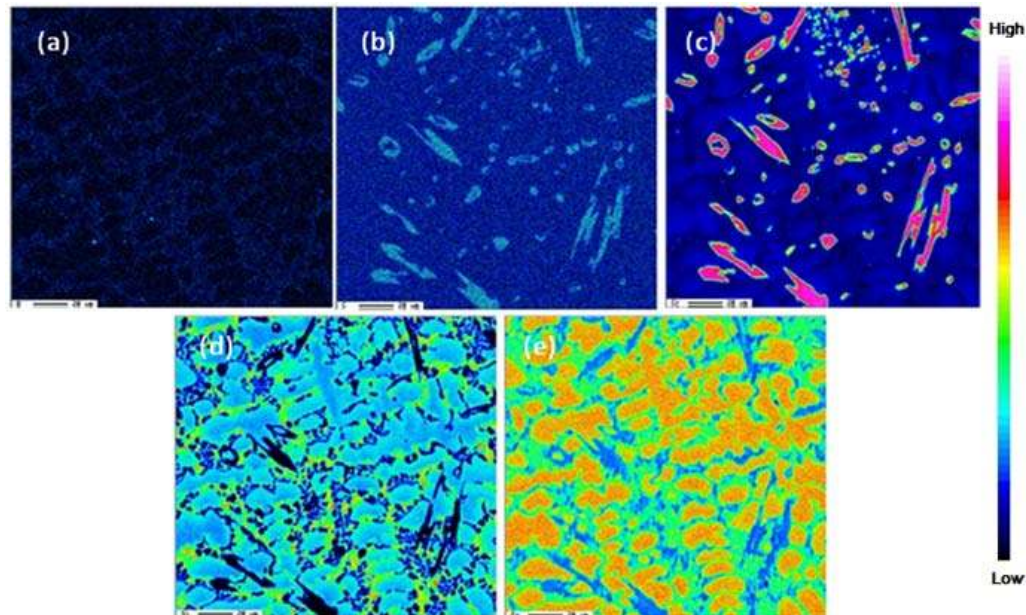
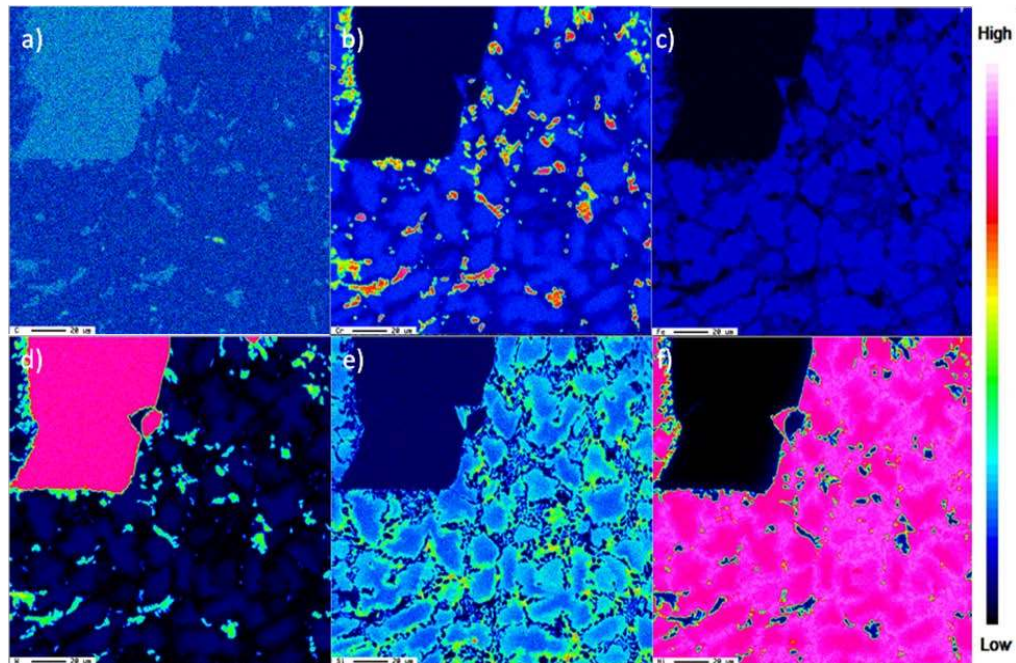**Figure C-2. EPMA area analysis of Colmonoy 4 showing a)Boron, b)Carbon, c)Chromium, d)Silicon, and e)Iron.**
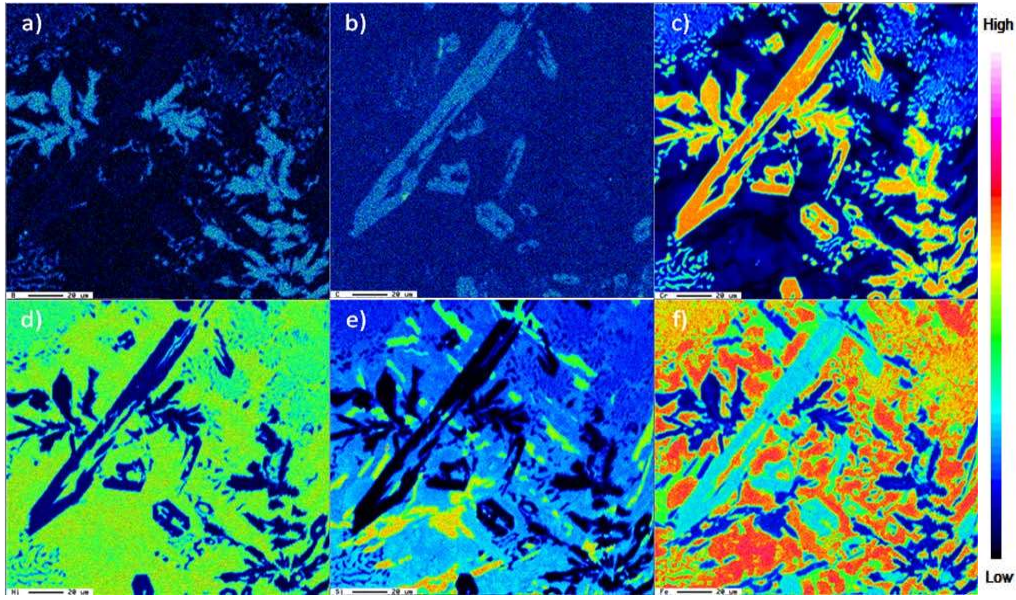
Figure C-3. EPMA area analysis of Colmonoy 6 showing a)boron, b)carbon, c)chromium, d)nickel, e)silicon, and f)iron.

Figure C-4. EPMA area analysis of Deloro 30 showing a)carbon, b)chromium, c)iron, d)tungsten, e)silicon, and f)nickel.
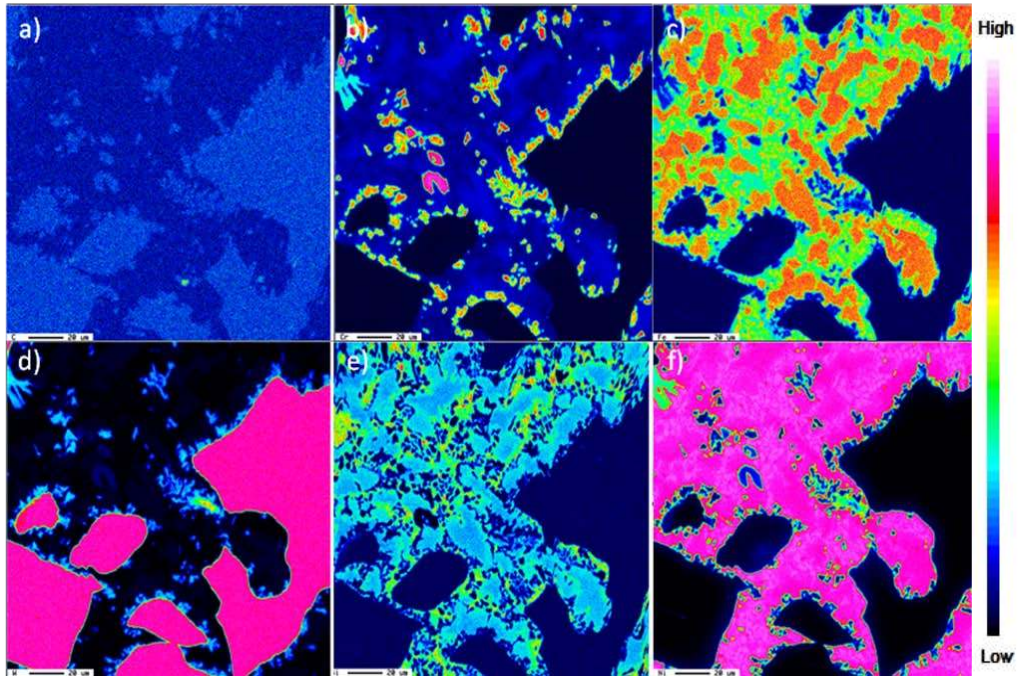
Figure C-5. EPMA area analysis of Colmonoy 4 MMC showing a)carbon, b)chromium, c)iron, d)tungsten, e)silicon, and f)nickel.
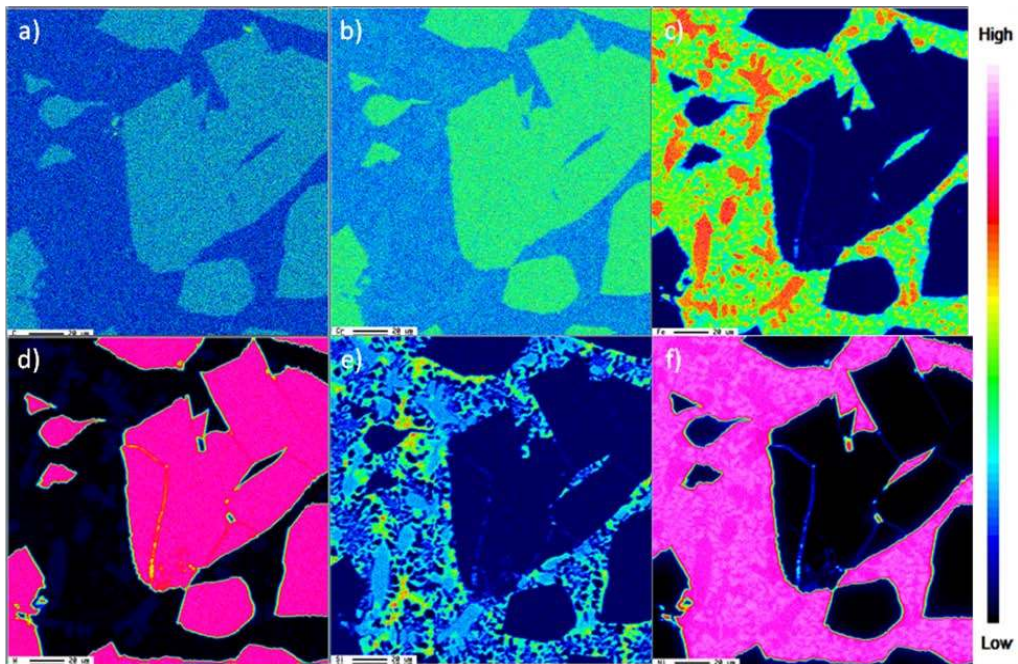

Figure C-6. EPMA area analysis of Hoganas 1559-SP329 MMC showing a)carbon, b)chromium, c)iron, d)tungsten, e)silicon, and f)nickel.
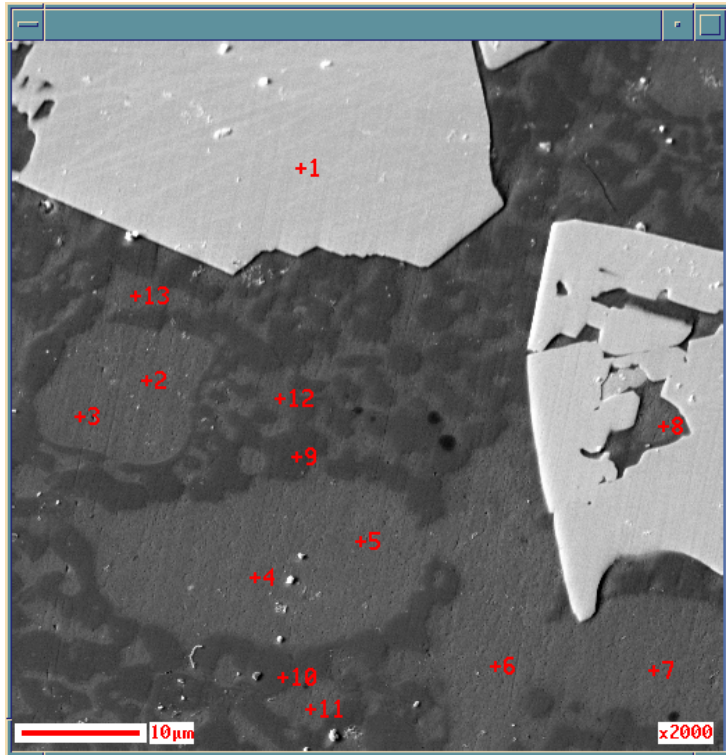
AES Results

Figure C-7. AES point analysis for Hoganas 1559-SP329 MMC.

Table C-1. AES point anlysis of Figure C-7.

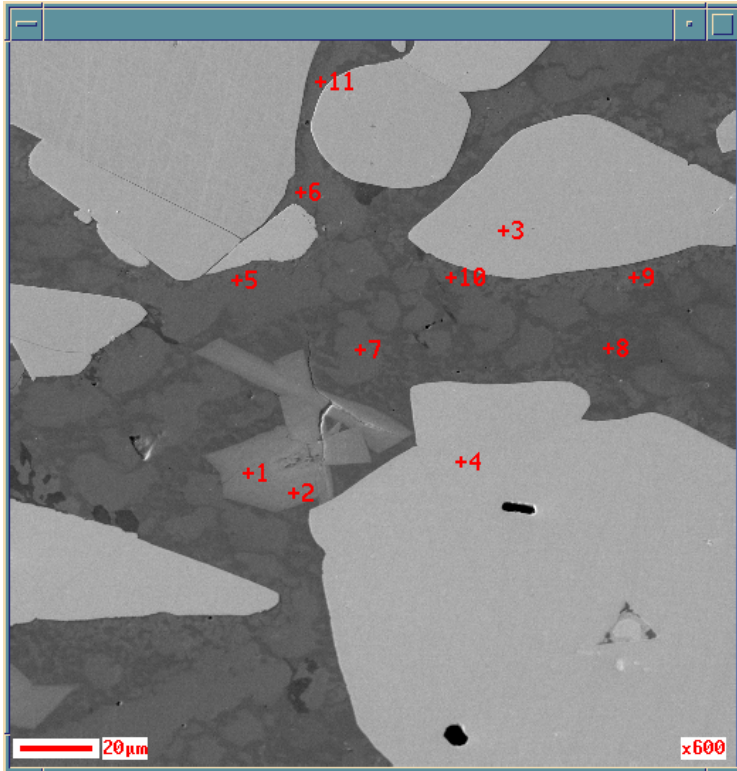| Point analyzed	C	W	Fe	Ni	B	Si
1	39.2	59.1	0	0	0	0
2	13.6	1	8.3	71.1	0	3.1
3	7.9	2	8.6	75.4	0	3.5
4	7.2	1	7.4	76.1	0	3.3
5	7.3	1.3	7.4	75.6	0	4.2
6	12.6	1.1	6.1	73.6	0	3
7	10.1	1.6	7.1	75.1	0	3.2
8	11.4	1.3	6.9	76	0	0.5
9	8.7	0	0	64	25.4	0
10	9.7	0	0	64	24.4	0
11	14.3	0.7	5.7	70.7	0	5.9
12	10.7	1.4	6	70.8	0	7.6
13	15	0	4.5	65.6	0	9.4

Figure C-8. AES point analysis for Colmonoy 4 MMC.

Table C-1. AES point anlysis of Figure C-8.

Point Analyzed	B	C	Cr	Fe	Ni	Si	W
1	0	19.4	19.3	1.6	23.3	9.9	26.5
2	0	19.6	20.1	0	20.6	9.5	30.2
3	0	39.9	1.8	0	0	0	58.3
4	0	38.8	2.6	0	0	0	58.6
5	0	37.2	43.9	0	1.6	0	17.3
6	0	36.6	46.9	0	0	0	16.5
7	0	6	6.4	2.4	77.4	6.3	1.5
8	20.1	4.4	5.3	1.8	59.9	7.4	1.1
9	0	34.5	40.3	0	7.5	3.1	14.6
10	0	37	44.6	0	0	0	18.4
11	0	4.8	6.6	1.7	77.3	7.6	2

Appendix D-Calculations

Volume fraction vs. weight fraction of WC particles in MMC alloys:

WC volume fraction = (60g WC/ 16g/cm^3)/((60g WC/ 16g/cm^3)+(40g Ni/ 9g/cm^3))
= 46 vol% WC

Appendix E-Wear Scar Images of Ni-WC Overlays
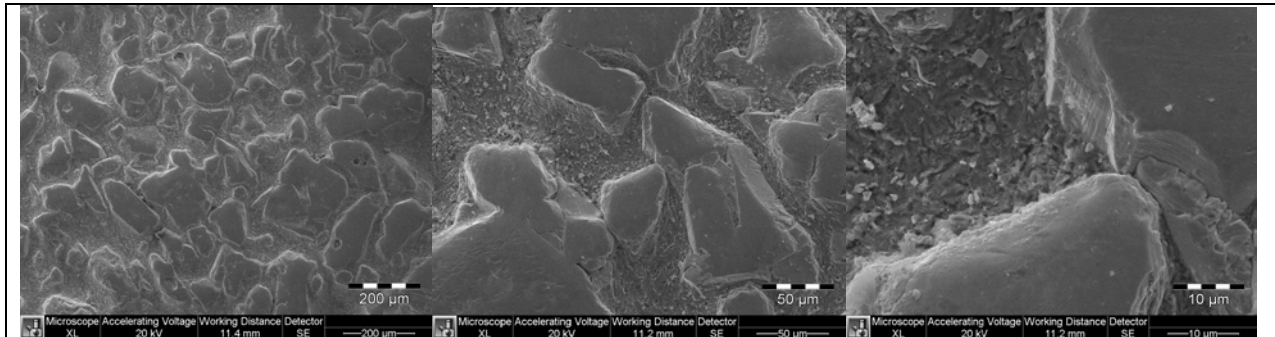
SEM Wear Scars

Figure E-1. Wear scar images for Hoganas 1559-SP329 Ni-WC overlay.

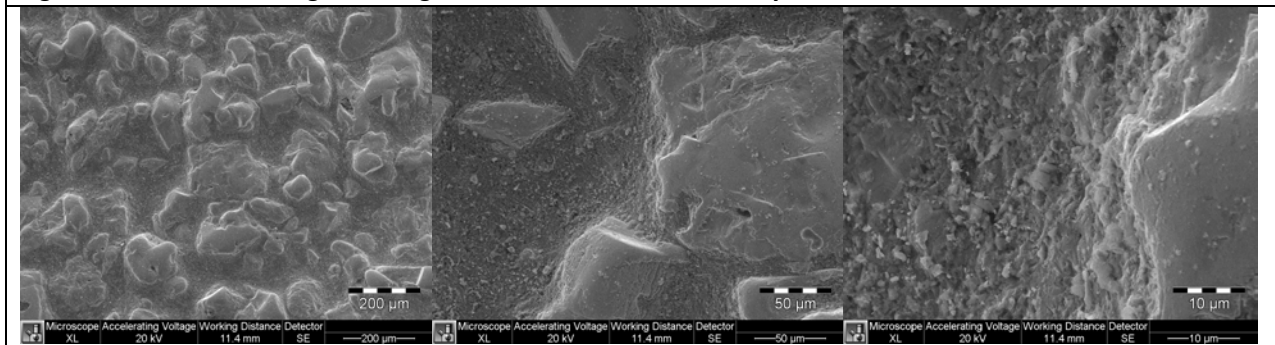
Figure E-2. Wear scar images for Deloro 30 Ni-WC overlay.
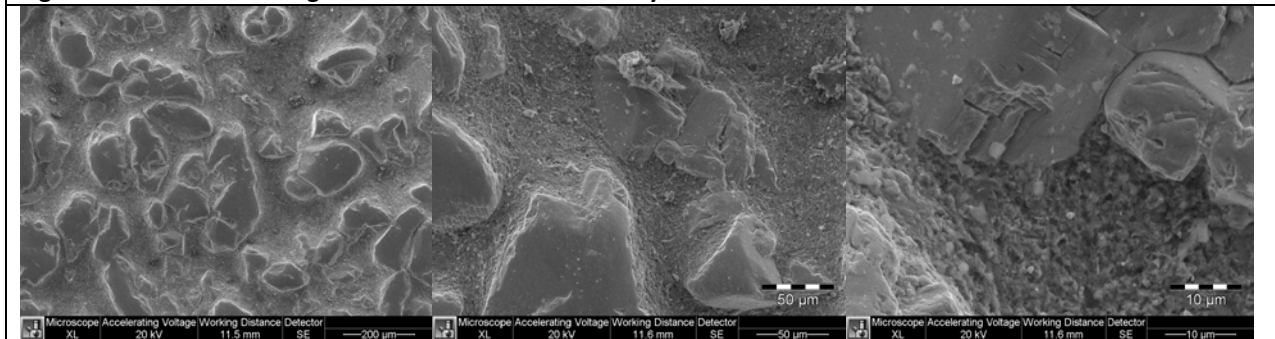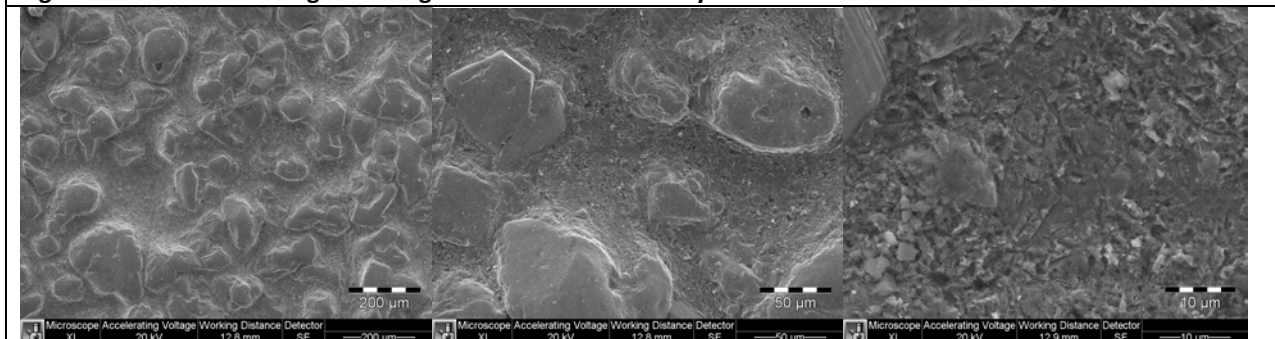

Figure E-3. Wear scar images for Hoganas 1535 Ni-WC overlay.

Figure E-4. Wear scar images for Colmonoy 4 Ni-WC overlay.